

UNIVERSITA' DEGLI STUDI DI VERONA

DEPARTMENT OF
BIOTECHNOLOGY

GRADUATE SCHOOL OF
NATURAL SCIENCES AND ENGINEERING

DOCTORAL PROGRAM IN
NANOSCIENCE AND ADVANCED TECHNOLOGIES

Cycle / year **XXIX/2014**

TITLE OF THE DOCTORAL THESIS

**LANTHANIDE DOPED ALKALINE-EARTH FLUORIDE
NANOPARTICLES AS BIOMEDICAL PROBES**

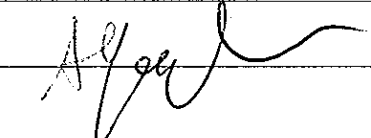
S.S.D. CHIM/03

(Please complete this space with the S.S.D. of your thesis – mandatory information)*

Coordinator: Prof. FRANCO TAGLIARO

Signature 

Tutor: Prof. ADOLFO SPEGHINI

Signature 




Doctoral Student: Dott. PAOLO CORTELLETTI

Signature 

* For the list of S.S.D. please refer to the Ministerial Decree of 4th October 2000, Attachment A "Elenco dei Settori Scientifico – Disciplinari" available at: http://www.miur.it/atti/2000/alladm001004_01.htm

This work is licensed under a Creative Commons Attribution-NonCommercial-NoDerivs 3.0 Unported License, Italy. To read a copy of the licence, visit the web page:

<http://creativecommons.org/licenses/by-nc-nd/3.0/>

-  **Attribution** — You must give appropriate credit, provide a link to the license, and indicate if changes were made. You may do so in any reasonable manner, but not in any way that suggests the licensor endorses you or your use.
-  **NonCommercial** — You may not use the material for commercial purposes.
-  **NoDerivatives** — If you remix, transform, or build upon the material, you may not distribute the modified material.

EXAMPLE:

Lanthanide Doped Alkaline-Earth Fluoride Nanoparticles as Biomedical Probes
Paolo Cortelletti
PhD thesis
Verona, 30/05/2017
ISBN xxxxx-xxxx-xxx

Abstract

In this thesis work, we present an investigation on lanthanide doped CaF_2 and SrF_2 nanoparticles doped with trivalent lanthanide ions. The first part of the thesis is focused on the site symmetry of lanthanide ions in CaF_2 and SrF_2 nanoparticles, using Eu^{3+} ions as symmetry probes, thanks to their peculiar luminescence features that are linked to their local symmetry. A reaction time dependent study was carried out, analyzing also the influence of Na^+ and K^+ ions, used as charge compensating ions to provide the neutrality of the nanoparticles, on the Eu^{3+} site symmetry. A site with D_2 symmetry was identified, with an extremely long luminescence decay time that suggests a possible use of the nanoparticles as probes for time-gated optical imaging. In the second part of the thesis we present Nd^{3+} doped CaF_2 nanoparticles that can be used as probes for optical imaging as well as nanothermometers in the near-infrared biological transparency windows to monitor the local temperature during a photothermal treatment. Since the Nd^{3+} emissions around 670 nm and 1050 nm show a temperature dependence, a ratiometric method was used to analyze the thermometry performance of the nanoparticles. The nanoparticles present a thermal sensitivity that is comparable to the sensitivity of other Nd^{3+} based nanothermometers and its minimum measurable temperature variation allows to monitor the threshold temperature during a photothermal therapy. The third part of the thesis shows the synthesis of core@shell@shell@shell SrF_2 nanoparticles, designed to be used as luminescent probes for visible and near-infrared optical imaging and as near-infrared nanothermometers. The structure of the nanoparticles were $\text{SrF}_2:\text{YbTm}@\text{Y}@\text{YbErNd}@\text{Nd}$, $\text{SrF}_2:\text{YbEr}@\text{Y}@\text{YbTmNd}@\text{Nd}$ and $\text{SrF}_2:\text{YbTm}@\text{Y}@\text{YbNd}@\text{Nd}$. The design of the nanoparticles allowed to obtain different upconversion emissions when the nanoparticles were excited at 800 nm (thanks to Nd^{3+} absorption) and 980 nm (thanks to Yb^{3+} absorption). By changing the Tm^{3+} and Er^{3+} ions in the core and in the second shell, it is possible to change the upconversion emission at two different exciting wavelengths. The energy transfer processes upon two different excitation wavelengths were studied. The nanothermometry properties were evaluated taking into account the temperature dependent relative variations of Yb^{3+} emission at 980 nm and Nd^{3+} emission at 1060 nm upon 800 nm excitation. We found that the thermal sensitivity can increase when a third dopant ion is introduced with Yb^{3+} and Nd^{3+} in the second shell of the nanoparticles and the nanoparticles doped with Er^{3+} present a higher sensitivity than the nanoparticles with Tm^{3+} as third dopant. The nanoparticles doped with Yb^{3+} , Nd^{3+} and Er^{3+} in the second shell present a sensitivity that is higher than most near-infrared nanothermometers, making them suitable as thermometric probes for temperature reading during a photothermal therapy.

Index

Introduction.....	p.07
Chapter 1	
Eu³⁺ doped CaF₂ and SrF₂ nanoparticles: structural and Spectroscopic investigation.....	p. 16
- 1.1 Introduction.....	p. 16
- 1.2 Experimental Section.....	p. 17
- 1.3 Results and Discussion.....	p. 18
- 1.4 Conclusions.....	p. 30
- REFERENCES.....	p. 31
Chapter 2	
Nd³⁺ activated CaF₂ NPs as colloidal nanothermometers in the biological window.....	p. 35
- 2.1 Introduction.....	p. 35
- 2.2 Experimental Details.....	p. 36
- 2.3 Results and Discussion.....	p. 37
- 2.4 Conclusions.....	p. 42
- REFERENCES.....	p. 43
Chapter 3	
Core@Multishell Architectures for Multicolor Upconversion and Near-Infrared Nanothermometry.....	p. 47
- 3.1 Introduction.....	p. 47
- 3.2 Experimental Section.....	p. 48
- 3.3 Results and Discussion.....	p. 50
- 3.4 Conclusions.....	p. 67
- REFERENCES.....	p. 69
Conclusions.....	p. 75
APPENDIX A.....	p. 77

Introduction

Nanotechnology has been unwittingly used for centuries or even millennia by artisans to produce ceramics, glasses, steel swords etc. Some examples can be reported about this ancient, naïve, use of nanotechnology. The Roman Lycurgus Cup, dated around the 4th century, is made of dichroic glass, thanks to gold and silver nanoparticles dispersed in the glass¹.

Damascus steel, famous for its peculiar pattern and extreme sharpness of the blades made of it, was probably invented in India around the 5th century B.C.² and carbon nanotubes and cementite (Fe_3C) nanowires were found in some ancient Damascus blades³⁻⁴. In addition, the luster of ancient Arabic potteries was found to be a colloidal dispersion of metallic nanoparticles in glass that provide the particular glaze and color changes that depend on the incident light interacting with the nanoparticles⁵⁻⁶.

Although nanotechnology has been widely used throughout human history, the first conscious scientific approach to nanotechnology can be dated to the middle of the 19th century, when Michael Faraday started studying colloidal gold, understanding that its color properties were due to the presence of gold particles with a tiny size in the solution⁷.

During the 20th century huge progresses were made in controlling and manipulating matter at an always smaller scale, that lead to the huge development of electronics, together with more powerful analytical techniques to investigate the properties of matter⁸. Therefore, after being almost ignored for the most of the 20th century, in the late 1970s – early 1980s the study of “tiny particles” received a huge boost, since the technology had advanced enough to allow the study the properties of nano-sized objects. In fact, the first time that the term “nanotechnology” (and as a consequence, nanoparticles, nano... etc.) was used was in 1986 in Drexler’s book, “Engines of Creation”⁹.

The interest on nanoparticles rapidly increased, because of the peculiar properties of matter at the nanoscale, since their small size can allow them to interact with light in different ways than bulk materials. At the nano-scale not only the interactions with light, but also the properties of the material change, since the surface/volume ratio strongly increases, providing interesting surface properties.

Several interesting studies have been carried out on metal or semiconductor nanoparticles, in particular on colloidal dispersions of the nanoparticles. In the case of metal nanoparticles they show enhanced plasmonic resonance thanks to their high surface to volume ratio, allowing them to reflect and adsorb light way differently than the bulk metals (e.g. the previously mentioned colloidal gold). The interactions of the “plasmonic” nanoparticles with light strongly depend on the size of the nanoparticles¹⁰⁻¹¹.

In the case of semiconductor nanostructures and nanoparticles (the so-called quantum dots), the involved mechanisms are different. Semiconductors present a “distortion” of the forbidden band when one or more of their dimensions decrease under the Bohr radius of the exciton in the semiconductor, allowing them to emit fluorescence under appropriate excitation. It is possible to tune the fluorescence emission wavelength of quantum dots by changing their size, virtually allowing quantum dots of a certain material to cover the entire visible spectrum¹²⁻¹⁵.

Several nanotechnological applications started to silently enter the life of common people since the end of the 1990s, but nowadays almost all of them exerting the intrinsic passive properties of the nanomaterials (e.g. titania nanoparticles in sunscreen lotions to adsorb UV light, silver nanoparticles used for their antibacterial properties, etc...).

Lanthanides doped inorganic nanoparticles are probably one of the latest “children” of nanotechnology, they made their appearance around year 2000¹⁶⁻¹⁹.

Lanthanides (from Ce to Yb on the periodic table) and lanthanides doped bulk materials have been deeply studied during the 20th century. The attention of the scientific community focused on lanthanides, and in particular on trivalent lanthanide ions, because of their peculiar luminescent properties. Trivalent lanthanide ions present a partially filled *f* electronic orbital, and their electronic transitions (named *ff* transitions) take place in this orbital. Since the *f* orbital is protected by the external *p* and *d* orbitals the emissions due to lanthanides’ *ff* transitions is protected and undergoes little changes when their local environmental conditions changes. Lanthanide ions emission spectra show narrow emission bands (on the contrary of quantum dots or organic molecules) thanks to the forbidden nature of *ff* transitions²⁰. A material conveniently doped with lanthanide ions can also show upconversion properties, in which high energy radiation is emitted when the material is excited with low energy radiation. Lanthanide doped bulk materials have been widely applied and can be found in lasers (e.g. Nd:YAG), permanent magnets, night visors, optical fibers, etc.

In this thesis, some potential applications of lanthanide doped nanoparticles are shown, since the interest in “active” nanoparticles has grown, in particular in the biomedical field. Lanthanide doped nanoparticles are good candidates as active materials, since their properties can be tuned by carefully choosing the lanthanide ions and varying their dopant concentration in the host material.

The materials studied for this work are CaF₂ and SrF₂ nanoparticles, doped with different lanthanide ions.

CaF₂ and SrF₂ are good hosts for luminescent trivalent lanthanide ions, in the first place because the radius of trivalent lanthanide ions is similar to the radius of Ca²⁺ and Sr²⁺ ions, therefore it can substitute them in the structure. Bulk CaF₂ and SrF₂ doped with Yb³⁺, Er³⁺, Tm³⁺, Nd³⁺ have been studied as laser materials. Lanthanide doped CaF₂ and SrF₂ have also shown interesting properties as near infrared (NIR) to visible upconverters (comparable to NaYF₄) thanks to their low phonon energy²¹⁻²³.

In 2011 our group presented a one-pot hydrothermal synthesis of citrate capped, water dispersible upconverting CaF₂ nanoparticles (that can be used also for SrF₂ nanoparticles), doped with Yb³⁺ and Tm³⁺ ions, allowing these materials to be used for biomedical applications^{22,24}.

The first chapter of the thesis will focus on the insertion site of lanthanide ions in CaF₂ and SrF₂, in particular Eu³⁺ ions, since, thanks to its half-filled *f* orbital, Eu³⁺ is a good probe to analyze the symmetry of the insertion site of lanthanides in a host. In particular the emission of Eu³⁺ ions strongly depends on the local symmetry surrounding Eu³⁺.

In Figure i.1 CaF₂ structure is shown (SrF₂ presents the same structure).

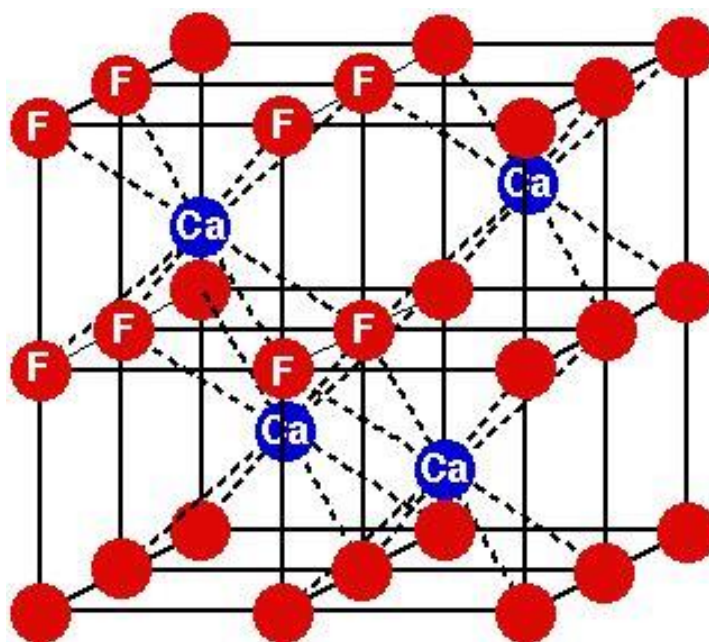


Figure i.1 CaF₂ crystal structure.

It is straightforward to assume that lanthanide ions insert in the fluoride structure substituting a Ca²⁺ (or Sr²⁺) that is located in a site with O_h symmetry. Since lanthanide ions are usually trivalent ions, the insertion of a lanthanide ion in a Ca²⁺ site provides an excess of positive charge that has to be compensated. There are several ways to provide a charge compensation, through interstitial F⁻ ions inserting the structure in different positions (in the nearest neighbors of the lanthanide ions or farther in the structure), through O²⁻ ions substituting an F⁻ ion or through a missing Ca²⁺ ion every two lanthanide ions doping the structure²⁵⁻²⁹. The symmetry changes from the O_h symmetry are well studied for these situations, but our hydrothermal synthesis involves sodium or potassium citrate. The citrate is not only used as capping agent, but also to provide charge compensation through Na⁺ or K⁺ ions entering the structure by substituting Ca²⁺ or Sr²⁺ ions (Na⁺ and K⁺ radius is similar to the radius of Ca²⁺ and Sr²⁺). Therefore, it was important to study the local site symmetry of Eu³⁺ ions in CaF₂ and SrF₂ nanoparticles, in order to understand how Eu³⁺ ions and Na⁺ or K⁺ ions can enter the CaF₂ and SrF₂ hosts.

The second chapter is dedicated to the study of Nd³⁺ and Gd³⁺ doped CaF₂ nanoparticles as NIR excited-NIR emitting nanothermometers and potential contrast agents for MRI. In the last decade a lot of efforts have been put in the synthesis of nanoparticles with diagnostic and therapeutic features for biomedical applications.

On the diagnostic side, several kind of quantum dots and lanthanide doped nanoparticles have been reported to be useful for optical imaging in the near-infrared biological windows, where skin, blood and muscles show the lowest absorption (exerting NIR excitation and emission)^{13, 22, 24, 30-33}. Gd³⁺ doped nanoparticles showed good paramagnetic properties, and might be novel contrast agents for MRI³⁴⁻³⁵.

On the therapeutic side of nanomedicine, nanoparticles are promising tools for cancer therapies. In particular gold nanoparticles and Nd³⁺ doped nanoparticles have shown interesting abilities to perform thermal treatment of tumors, when they are illuminated with NIR light^{31, 36-39}. During a thermal treatment the local temperature can easily exceed the safety thresholds for the therapy, since the temperature level must be high enough to kill cancer cells without harming the healthy cells⁴⁰. In this field nanothermometers can be a useful tool to monitor instantaneously the local temperature, to check when the thermal treatment should be stopped.

From a general point of view to perform a thermometric measurement, we need a measurable quantity that changes when the temperature changes, e.g. in the old mercury thermometers the level of mercury used to change with temperature, or in modern electronic thermometers a change in the conductivity is measured, etc.

In the case of nanothermometers the most useful parameter that can be measured are variations in the nanoparticles emission when temperature changes. Many strategies have been developed to achieve a high thermometric performance with nanoparticles, some of them rely on single nanoparticles^{31, 41-42}, while others use more complicated hybrid structures, combining lanthanide doped nanoparticles with quantum dots, or functionalizing the nanoparticles with fluorescent molecules⁴³⁻⁴⁴.

Some research groups have reported several nanothermometers based on Nd³⁺ emission in the last years^{39, 45-47}. All these nanothermometers rely on the variation of the electronic population of two Nd³⁺ energy levels (or Stark sublevels) that present a small energy gap between each other. The energy levels population changes according to temperature following Boltzmann distribution

$$\frac{L_2}{L_1} = e^{-\frac{\Delta E}{kT}} \quad (i.1)$$

where L_2 is the higher energy level, L_1 is the lower energy level, ΔE is the energy difference between L_2 and L_1 , k is the Boltzmann constant and T is the temperature in Kelvin.

Since the variation of the emission intensity depends also on the instrumental setup it is a common practice to choose another emission band as a reference, and divide the “thermometric” band to the reference band for each spectrum at different temperatures, in order to make the temperature measurement independent from the instrumental setup⁴².

The third chapter presents a study about more complicated SrF₂ nanoparticles, with a core@multishell structure, with the core and each shell doped with different combinations of lanthanide ions, similar to those synthesized by Lai et al.⁴⁸. These nanoparticles were designed to obtain the emission from different lanthanide ions when they are excited with 980 nm or 800 nm lasers. The aim was to obtain multimodal nanoparticles with the ability to emit UV light in order to activate potentially some photocatalytic mechanisms with also the possibility to make thermometric measurements in the NIR range.

In this way it has been possible to obtain Tm^{3+} emission by exciting the nanoparticles at 980 nm and Er^{3+} upconversion emission and Yb^{3+} and Nd^{3+} emissions when exciting at 800 nm.

In this case the nanothermometric properties develop from a combination of the Boltzmann thermalization processes described in chapter 2 and a non-resonant phonon assisted energy transfer from Nd^{3+} ions to Yb^{3+} ions. As it has been shown in the papers of Ximendes et al.³⁹, Marciniak et al.⁴⁹ and several other papers the latter mechanism is described by the Miyakawa-Dexter theory. According to the Miyakawa-Dexter model the probability of a phonon assisted energy transfer between two different energy levels is described by the equation

$$W_{ET}(T) = W_0 e^{-\beta\Delta E} \times A(T)^N \quad (\text{i.2})$$

where W_0 is the probability for a perfectly resonant energy transfer between two levels of the donor and the acceptor ions if the energy of the two levels is the same, β is a constant that depends on the host material, ΔE is the energy difference between the two involved levels, N is the number of phonons involved in the energy transfer and $A(T)$ is the temperature dependent parameter, defined as

$$A(T) = \begin{cases} n(T) + 1 & \text{for the absorption of a phonon} \\ n(T) - 1 & \text{for the emission of a phonon} \end{cases} \quad (\text{i.3})$$

where $n(T)$ is the effective temperature dependent parameter defined as

$$n(T) = \frac{1}{e^{\frac{\hbar\omega}{kT}} - 1} \quad (\text{i.4})$$

Where $\hbar\omega$ is the phonon energy, k is the Boltzmann constant and T is the temperature in Kelvin.

The strategy of exerting the $\text{Nd}^{3+} \rightarrow \text{Yb}^{3+}$ energy transfer is a hot topic in the nanothermometry field, since it shows a good potential for improving its thermometric performance.

Each chapter is structured like a scientific paper for convenience's sake. Chapter 2 has already been published.

REFERENCES

1. Freestone, I.; Meeks, N.; Sax, M.; Higgitt, C., The Lycurgus Cup — A Roman nanotechnology. *Gold Bulletin* **2007**, *40* (4), 270-277.
2. Srinivasan, S., Wootz Crucible Steel: A Newly Discovered Production Site in South India. *Papers from the Institute of Archaeology* **1994**, *5*, 49.
3. Reibold, M.; Paufler, P.; Levin, A. A.; Kochmann, W.; Pätzke, N.; Meyer, D. C., Discovery of Nanotubes in Ancient Damascus Steel. **2009**, *127*, 305-310.
4. Reibold, M.; Paufler, P.; Levin, A. A.; Kochmann, W.; Patzke, N.; Meyer, D. C., Materials: carbon nanotubes in an ancient Damascus sabre. *Nature* **2006**, *444* (7117), 286.
5. Colombari, P., The Use of Metal Nanoparticles to Produce Yellow, Red and Iridescent Colour, from Bronze Age to Present Times in Lustre Pottery and Glass: Solid State Chemistry, Spectroscopy and Nanostructure. *Journal of Nano Research* **2009**, *8*, 109-132.
6. Padeletti, G.; Fermo, P.; Gilardoni, S., Technological investigation of luster decorated ancient majolicas. *MRS Proceedings* **2011**, *712*.
7. Faraday, M., The Bakerian Lecture: Experimental Relations of Gold (and Other Metals) to Light. *Philosophical Transactions of the Royal Society of London* **1857**, *147* (0), 145-181.
8. Binnig, G.; Quate, C. F.; Gerber, C., Atomic force microscope. *Phys Rev Lett* **1986**, *56* (9), 930-933.
9. Drexler, E., Engines of Creation The Coming Era of Nanotechnology. **1986**.
10. Wurtz, G. A.; Im, J. S.; Gray, S. K.; Wiederrecht, G. P., Optical Scattering from Isolated Metal Nanoparticles and Arrays. *The Journal of Physical Chemistry B* **2003**, *107* (51), 14191-14198.
11. Andrews, D. L.; Steinbrück, A.; Nunzi, J.-M.; Csáki, A.; Festag, G.; Ostendorf, A.; Fritzsche, W., Designing plasmonic structures: bi-metallic core-shell nanoparticles. **2006**, *6195*, 619513.
12. Alivisatos, A. P., Semiconductor Clusters, Nanocrystals, and Quantum Dots. *Science* **1996**, *271* (5251), 933-937.
13. Bruchez Jr, M., Semiconductor Nanocrystals as Fluorescent Biological Labels. *Science* **1998**, *281* (5385), 2013-2016.
14. Michalet, X.; Pinaud, F. F.; Bentolila, L. A.; Tsay, J. M.; Doose, S.; Li, J. J.; Sundaresan, G.; Wu, A. M.; Gambhir, S. S.; Weiss, S., Quantum dots for live cells, in vivo imaging, and diagnostics. *Science* **2005**, *307* (5709), 538-44.
15. Medintz, I. L.; Uyeda, H. T.; Goldman, E. R.; Mattoussi, H., Quantum dot bioconjugates for imaging, labelling and sensing. *Nature materials* **2005**, *4* (6), 435-46.
16. Polizzi, S.; Fagherazzi, G.; Battagliarin, M.; Bettinelli, M.; Speghini, A., Fractal aggregates of lanthanide-doped Y2O3 nanoparticles obtained by propellant synthesis. *Journal of Materials Research* **2001**, *16* (01), 146-154.
17. Vetrone, F.; Boyer, J.-C.; Capobianco, J. A.; Speghini, A.; Bettinelli, M., Luminescence Spectroscopy and Near-Infrared to Visible Upconversion of Nanocrystalline Gd3Ga5O12:Er3+. *The Journal of Physical Chemistry B* **2003**, *107* (39), 10747-10752.
18. Hartridge, A.; Krishna, M. G.; Bhattacharya, A. K., Optical constants of nanocrystalline lanthanide-doped ceria thin films with the fluorite structure. *Journal of Physics and Chemistry of Solids* **1998**, *59* (6-7), 859-866.

19. Tissue, B. M., Synthesis and Luminescence of Lanthanide Ions in Nanoscale Insulating Hosts. *Chemistry of Materials* **1998**, *10* (10), 2837-2845.
20. Bünzli, J.-C. G.; Eliseeva, S. V., Basics of Lanthanide Photophysics. In *Lanthanide Luminescence: Photophysical, Analytical and Biological Aspects*, Hänninen, P.; Härmä, H., Eds. Springer Berlin Heidelberg: Berlin, Heidelberg, **2011**, pp 1-45.
21. Pedroni, M.; Piccinelli, F.; Passuello, T.; Giarola, M.; Mariotto, G.; Polizzi, S.; Bettinelli, M.; Speghini, A., Lanthanide doped upconverting colloidal CaF₂ nanoparticles prepared by a single-step hydrothermal method: toward efficient materials with near infrared-to-near infrared upconversion emission. *Nanoscale* **2011**, *3* (4), 1456-60.
22. Pedroni, M.; Piccinelli, F.; Passuello, T.; Polizzi, S.; Ueda, J.; Haro-González, P.; Martinez Maestro, L.; Jaque, D.; García-Solé, J.; Bettinelli, M.; Speghini, A., Water (H₂O and D₂O) Dispersible NIR-to-NIR Upconverting Yb³⁺/Tm³⁺+Doped MF₂(M = Ca, Sr) Colloids: Influence of the Host Crystal. *Crystal Growth & Design* **2013**, *13* (11), 4906-4913.
23. Quintanilla, M.; Cantarelli, I. X.; Pedroni, M.; Speghini, A.; Vetrone, F., Intense ultraviolet upconversion in water dispersible SrF₂:Tm³⁺,Yb³⁺+nanoparticles: the effect of the environment on light emissions. *J. Mater. Chem. C* **2015**, *3* (13), 3108-3113.
24. Dong, N. N.; Pedroni, M.; Piccinelli, F.; Conti, G.; Sbarbati, A.; Ramirez-Hernandez, J. E.; Maestro, L. M.; Iglesias-de la Cruz, M. C.; Sanz-Rodríguez, F.; Juarranz, A.; Chen, F.; Vetrone, F.; Capobianco, J. A.; Sole, J. G.; Bettinelli, M.; Jaque, D.; Speghini, A., NIR-to-NIR two-photon excited CaF₂:Tm³⁺,Yb³⁺ nanoparticles: multifunctional nanoprobe for highly penetrating fluorescence bio-imaging. *ACS nano* **2011**, *5* (11), 8665-71.
25. Barsis, E., Lattice Disorder in Some CaF₂-Type Crystals. *The Journal of Chemical Physics* **1966**, *45* (4), 1154.
26. Cascales, C.; Fernandez, J.; Balda, R., Investigation of site-selective symmetries of Eu³⁺ ions in KPb₂Cl₅ by using optical spectroscopy. *Optics express* **2005**, *13* (6), 2141.
27. Du, F.; Nakai, Y.; Tsuboi, T.; Huang, Y.; Seo, H. J., Luminescence properties and site occupations of Eu³⁺ ions doped in double phosphates Ca₉R(PO₄)₇ (R = Al, Lu). *Journal of Materials Chemistry* **2011**, *21* (12), 4669.
28. Hamers, R. J., Defect chemistry in CaF₂:Eu³⁺ *The Journal of Chemical Physics* **1982**, *77* (2), 683.
29. Ito, M.; Goutaudier, C.; Guyot, Y.; Lebbou, K.; Fukuda, T.; Boulon, G., Crystal growth, Yb³⁺ spectroscopy, concentration quenching analysis and potentiality of laser emission in Ca_{1-x}Yb_xF₂. *Journal of Physics: Condensed Matter* **2004**, *16* (8), 1501-1521.
30. Bunzli, J. C., Lanthanide luminescence for biomedical analyses and imaging. *Chemical reviews* **2010**, *110* (5), 2729-55.
31. Carrasco, E.; del Rosal, B.; Sanz-Rodríguez, F.; de la Fuente, Á. J.; Gonzalez, P. H.; Rocha, U.; Kumar, K. U.; Jacinto, C.; Solé, J. G.; Jaque, D., Intratumoral Thermal Reading During Photo-Thermal Therapy by Multifunctional Fluorescent Nanoparticles. *Advanced Functional Materials* **2015**, *25* (4), 615-626.
32. Hong, H.; Shi, J.; Yang, Y.; Zhang, Y.; Engle, J. W.; Nickles, R. J.; Wang, X.; Cai, W., Cancer-targeted optical imaging with fluorescent zinc oxide nanowires. *Nano letters* **2011**, *11* (9), 3744-50.

33. Seo, D.; Farlow, J.; Southard, K.; Jun, Y. W.; Gartner, Z. J., Production and targeting of monovalent quantum dots. *Journal of visualized experiments : JoVE* **2014**, (92), e52198.
34. Cantarelli, I. X.; Pedroni, M.; Piccinelli, F.; Marzola, P.; Boschi, F.; Conti, G.; Sbarbati, A.; Bernardi, P.; Mosconi, E.; Perbellini, L.; Marongiu, L.; Donini, M.; Dusi, S.; Sorace, L.; Innocenti, C.; Fantechi, E.; Sangregorio, C.; Speghini, A., Multifunctional nanoprobe based on upconverting lanthanide doped CaF₂: towards biocompatible materials for biomedical imaging. *Biomaterials Science* **2014**, 2 (9), 1158.
35. Passuello, T.; Pedroni, M.; Piccinelli, F.; Polizzi, S.; Marzola, P.; Tambalo, S.; Conti, G.; Benati, D.; Vetrone, F.; Bettinelli, M.; Speghini, A., PEG-capped, lanthanide doped GdF₃ nanoparticles: luminescent and T₂ contrast agents for optical and MRI multimodal imaging. *Nanoscale* **2012**, 4 (24), 7682-9.
36. Cheng, L.; Wang, C.; Liu, Z., Upconversion nanoparticles and their composite nanostructures for biomedical imaging and cancer therapy. *Nanoscale* **2013**, 5 (1), 23-37.
37. Lv, R.; Zhong, C.; Li, R.; Yang, P.; He, F.; Gai, S.; Hou, Z.; Yang, G.; Lin, J., Multifunctional Anticancer Platform for Multimodal Imaging and Visible Light Driven Photodynamic/Photothermal Therapy. *Chemistry of Materials* **2015**, 27 (5), 1751-1763.
38. Ximendes, E. C.; Rocha, U.; Jacinto, C.; Kumar, K. U.; Bravo, D.; Lopez, F. J.; Martin Rodriguez, E.; Garcia-Sole, J.; Jaque, D., Self-monitored photothermal nanoparticles based on core-shell engineering. *Nanoscale* **2016**, 8 (5), 3057-66.
39. Ximendes, E. C.; Rocha, U.; Kumar, K. U.; Jacinto, C.; Jaque, D., LaF₃ core/shell nanoparticles for subcutaneous heating and thermal sensing in the second biological-window. *Applied Physics Letters* **2016**, 108 (25), 253103.
40. Yarmolenko, P. S.; Moon, E. J.; Landon, C.; Manzoor, A.; Hochman, D. W.; Viglianti, B. L.; Dewhirst, M. W., Thresholds for thermal damage to normal tissues: an update. *International journal of hyperthermia : the official journal of European Society for Hyperthermic Oncology, North American Hyperthermia Group* **2011**, 27 (4), 320-43.
41. del Rosal, B.; Ximendes, E.; Rocha, U.; Jaque, D., In Vivo Luminescence Nanothermometry: from Materials to Applications. *Advanced Optical Materials* **2016**.
42. Jaque, D.; Vetrone, F., Luminescence nanothermometry. *Nanoscale* **2012**, 4 (15), 4301-26.
43. Ceron, E. N.; Ortgies, D. H.; Del Rosal, B.; Ren, F.; Benayas, A.; Vetrone, F.; Ma, D.; Sanz-Rodriguez, F.; Sole, J. G.; Jaque, D.; Rodriguez, E. M., Hybrid nanostructures for high-sensitivity luminescence nanothermometry in the second biological window. *Advanced materials* **2015**, 27 (32), 4781-7.
44. Donner, J. S.; Thompson, S. A.; Kreuzer, M. P.; Baffou, G.; Quidant, R., Mapping intracellular temperature using green fluorescent protein. *Nano letters* **2012**, 12 (4), 2107-11.
45. Balabhadra, S.; Debasu, M. L.; Brites, C. D.; Nunes, L. A.; Malta, O. L.; Rocha, J.; Bettinelli, M.; Carlos, L. D., Boosting the sensitivity of Nd(3+)-based luminescent nanothermometers. *Nanoscale* **2015**, 7 (41), 17261-7.
46. Rocha, U.; Upendra Kumar, K.; Jacinto, C.; Ramiro, J.; Caamaño, A. J.; García Solé, J.; Jaque, D., Nd³⁺ doped LaF₃ nanoparticles as self-monitored photo-thermal agents. *Applied Physics Letters* **2014**, 104 (5), 053703.

47. Benayas, A.; del Rosal, B.; Pérez-Delgado, A.; Santacruz-Gómez, K.; Jaque, D.; Hirata, G. A.; Vetrone, F., Nd:YAG Near-Infrared Luminescent Nanothermometers. *Advanced Optical Materials* **2015**, *3* (5), 687-694.
48. Lai, J.; Zhang, Y.; Pasquale, N.; Lee, K. B., An upconversion nanoparticle with orthogonal emissions using dual NIR excitations for controlled two-way photoswitching. *Angewandte Chemie* **2014**, *53* (52), 14419-23.
49. Marciniak, L.; Bednarkiewicz, A.; Stefanski, M.; Tomala, R.; Hreniak, D.; Strek, W., Near infrared absorbing near infrared emitting highly-sensitive luminescent nanothermometer based on Nd(3+) to Yb(3+) energy transfer. *Physical chemistry chemical physics : PCCP* **2015**, *17* (37), 24315-21.

Chapter 1

Eu³⁺ doped CaF₂ and SrF₂ nanoparticles: structural and spectroscopic investigation

1.1 Introduction

Luminescent lanthanide doped inorganic nanoparticles (NPs) have in recent years continuously increased their importance, as their features allow many potential technological applications in several fields. In nanosized form, they have been found useful as optical labels and probes for biomedical applications as well as in photovoltaic devices.¹⁻⁶ Upconverting NPs have been also investigated and in particular the interest in alkaline-earth fluorides such as CaF₂ and SrF₂ has been raised recently due to their interesting upconverting properties.^{7,8} While the local environment of single crystal lanthanide doped alkaline-earth fluorides has been deeply studied⁹⁻¹², scientific literature is lacking of the same analyses for alkaline-earth fluorides. Some investigation on Yb³⁺, Er³⁺ codoped CaF₂ and SrF₂ NPs have been carried out, demonstrating that these hosts can be valid substitutes as doping materials. The local environment of lanthanide ions as dopants in CaF₂ and SrF₂ hosts NPs is strictly correlated with their emission properties. In the present paper, an investigation on the spectroscopic and structural properties of Eu³⁺ doped CaF₂ and SrF₂ NPs is presented. The methodology involves the use of the citrate moiety as a hydrophilic capping agent, to ensure an excellent dispersion in water. Since Eu³⁺ is a trivalent ion and enters the CaF₂ or SrF₂ host substituting the Ca²⁺ or Sr²⁺ ion the excess of positive charge must be compensated to maintain the neutrality of the NPs and to avoid the clustering of the lanthanide ions.¹³ Usually, if nothing specific is used, in CaF₂ or SrF₂ the charge compensation is provided by interstitial F⁻ ions, that can exert a local charge compensation, if they are located in a crystalline cube near the lanthanide ion (Ln³⁺) position, or a non-local charge compensation, if they are located in a more distant position. These mechanisms are well studied, and lead to the formation of Ln³⁺ sites with C_{3v} or C_{4v} symmetry in the case of local charge compensation, and to sites with O_h symmetry in the case of non-local charge compensation. The presence of interstitial F⁻ ions also induces a distortion in the lattice structure because of the repulsion between the F⁻ ions.¹³⁻¹⁶

In this study Na⁺ or K⁺ present as counterions of the citrate were chosen to provide charge compensation, because they are positively charged and because their dimensions are similar to Ca²⁺ and Sr²⁺ dimensions, so they should easily enter the CaF₂ or SrF₂ host substituting Ca²⁺ and Sr²⁺ ions that are nearest neighbors of the Ln³⁺ ions¹⁷⁻¹⁹. Eu³⁺ is not only an excellent ion to investigate the site symmetry in which the lanthanide ions are accommodated^{9,20,21} but also its good emission in the red region of the visible spectrum is interesting for possible applications in biomedicine. Moreover, in order to evaluate the effects of the reaction time, several reactions were carried out changing the reaction times.

1.2 Experimental Section

Synthesis procedure

1% Europium doped MF_2 ($\text{M}=\text{Ca}^{2+}, \text{Sr}^{2+}$) NPs ($\text{CaF}_2\text{:Eu}$ NPs or $\text{SrF}_2\text{:Eu}$ NPs) were prepared by a hydrothermal synthesis (using a metal to RE ratio of 0.99:0.01). Stoichiometric quantities of $\text{CaCl}_2\cdot 2\text{H}_2\text{O}$ (Baker, >99%) or $\text{SrCl}_2\cdot 6\text{H}_2\text{O}$ (Carlo Erba, >99%), $\text{EuCl}_3\cdot 6\text{H}_2\text{O}$ (Aldrich, 99.99%), (total metal amount of $3.5\cdot 10^{-3}$ mol), were dissolved in 5 ml of deionized water in a Teflon vessel.

20 ml of a 1 M sodium citrate (Na-cit) or potassium citrate (K-cit) di-hydrated (Fluka, $\geq 99\%$) solution was added under vigorous stirring for few minutes. Potassium and sodium citrate were chosen not only to be the capping agent, but also as source of Na^+ or K^+ ions. A 3.5M aqueous solution of NH_4F (Baker, 99%) was added to the previous suspension, in order to have an excess of fluoride ions with respect to the stoichiometric amounts ($(\text{M}+\text{Eu})\text{:F}=1\text{:}2.5$, $\text{M}=\text{Ca}$ or Sr). The obtained clear solution was put in a Teflon lined pressure digester (DAB-2, Berghof) and heat treated in an oven at 190°C for different times, under autogenous pressure. The autoclave was then cooled to room temperature and after centrifugation (at 7000 rpm, for 10 min) the CaF_2 or SrF_2 NPs were collected. After a proper washing with a solution (ratio about 2:1) of deionized water and acetone or ethanol (to help the NPs precipitation), the NPs were stored under acetone or ethanol. The NPs can be easily dispersed in water as well as in saline solution to form transparent colloids. To obtain the NPs in powder form, they were dried at room temperature for 24 h and milled in an agate mortar. Hereafter the samples will be denoted as CN[reaction time in minutes] (for CaF_2 samples) or SN[reaction time in minutes] (for SrF_2 samples) if sodium citrate is the starting reagent, CK[reaction time in minutes] (for CaF_2 samples) if the starting reagent is potassium citrate.

X-Ray powder diffraction patterns

X-Ray powder diffraction (XRPD) patterns were measured with a Thermo ARL X'TRA powder diffractometer, operating in Bragg-Brentano geometry equipped with a Cu-anode X-ray source (K_α , $\lambda=1.5418$ Å) and using a Peltier Si(Li) cooled solid state detector. The spectra were collected with a scan rate of $2.5^\circ/\text{s}$, with a measurement time of 12 ms/step and 2θ range of 20° - 90° . The phase identification were performed with PDF-4+ 2009 database provided by the International Centre for Diffraction Data (ICDD). The instrumental X-Ray peak broadening was determined exploiting LaB_6 standard reference material (SRM 660a) provided by NIST, the cell parameters were precisely determined using $\alpha\text{-SiO}_2$ as an internal standard. The samples were carefully homogenized in a mortar, and deposited in a low-background sample stage.

Transmission Electron Microscopy

Transmission Electron Microscopy (TEM) and high resolution TEM (HRTEM) images were measured using a JEOL 3010 high resolution electron microscope (0.17 nm point-to-point), operating at 300 KV, equipped with a Gatan slow-scan CCD camera (model 794) and an Oxford Instrument EDS microanalysis detector (Model 6636). The powders were dispersed in water in order to be deposited. The NPs were suspended in deionized water and deposited on copper grids.

Spectroscopy measurements

Photoluminescence measurements were carried out using a tunable dye laser pumped by a Nd:YAG laser. The emission signal was analyzed by a half-meter monochromator (HR460, Jobin Yvon) equipped with a 1200 g/mm grating and detected with a CCD detector (Spectrum One, Jobin Yvon) or with a GaAs photomultiplier (Hamamatsu). The spectral resolution of the emission spectra is 0.1 nm. Lifetime measurements were acquired using a 500 MHz oscilloscope (Le Croy, Waverunner) connected with the photomultiplier. 77 K emission spectra were acquired with a home-made cold finger cryostat filled with liquid nitrogen. Excitation spectra were acquired using a Horiba-Jobin Yvon, Fluorolog-3 spectrophotometer, equipped with a Xenon lamp.

ICP-MS

ICP-MS analysis was carried out with using a Thermo Fisher Scientific model X Series II equipped with a technology collision/reaction cell (CCT). The NPs were de-capped from the citrate groups by washing them with a diluted nitric acid solution (0.5%) and recollecting them by centrifugation several times. The de-capped NPs were dissolved in a 5% nitric acid solution.

1.3 Results and Discussion

Structural and morphological characterization

The XRPD spectra are shown in figure 1.1. All the alkaline-earth fluoride NPs are cubic single phases (space group n. 225, $Fm\bar{3}m$). A Rietveld structural and microstructural refinement using MAUD software²² employing the crystal structural model determined by Laval et al.¹² in the case of $\text{CaF}_2:\text{Eu}$ and that one determined by Forsyth²³ in the case of $\text{SrF}_2:\text{Eu}$. The extreme purity of the samples is shown in the logarithmic graph in figure A1 of **APPENDIX A** (Supporting Information), evidencing that only the features of the expected cubic phase are present.

The shift of the XRPD peaks for $\text{CaF}_2:\text{Eu}$ NPs towards lower angles than for pure CaF_2 is due to the smaller ionic radius of Eu^{3+} (1.066 Å) compared with the Ca^{2+} one (1.12 Å), indicating the incorporation of the Eu^{3+} ions in the host structure. A similar behaviour is observed for the SrF_2 NPs. The diffraction peaks correspond to Miller's indexes values (hkl) of (111), (200), (220), (311), (400), (331) and (422)²⁴⁻²⁶ for CaF_2 and (111), (200), (220), (311), (222) (400), (331) and (422) for SrF_2 .²⁷⁻³⁰ In Table 1.1, the results from the Rietveld refinement are reported. It can be noticed that the NPs are larger as the reaction time increases.

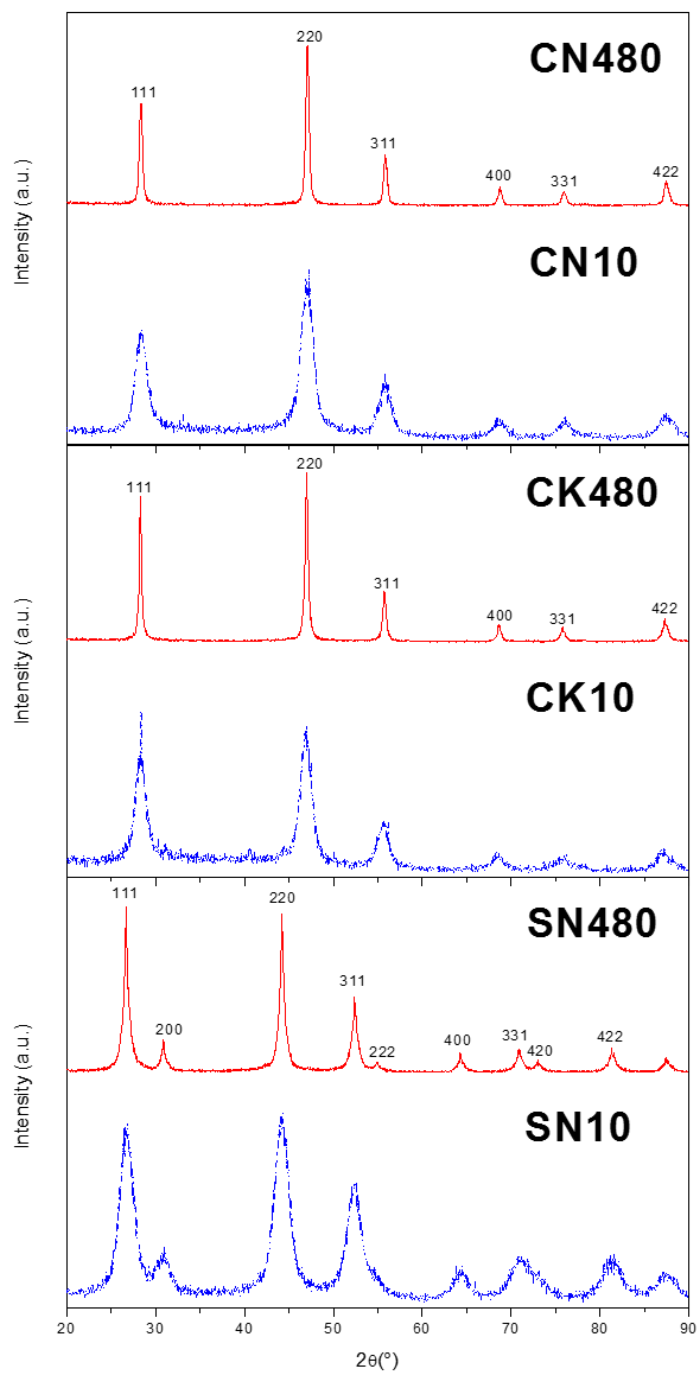


Figure 1.1 XRD spectra of the CN, CK and SN nanoparticles, in red the samples after 8 h of reaction time, in blue the samples after 10 min reaction time.

Table 1.1 NPs size evaluated from XRPD

Reaction Time	Nanoparticles size (nm)		
	CaF ₂ + Na-cit	CaF ₂ + K-Cit	SrF ₂ + Na-cit
10 min	8.9 ± 1.0	9.3 ± 1.6	6.8 ± 0.7
35 min	10.7 ± 1.3	11.8 ± 1.2	8.5 ± 0.7
6 hours	21.9 ± 2.4	15.7 ± 1.4	13.1 ± 0.7
8 hours	38.9 ± 4.5	35.1 ± 0.7	15.8 ± 1.0

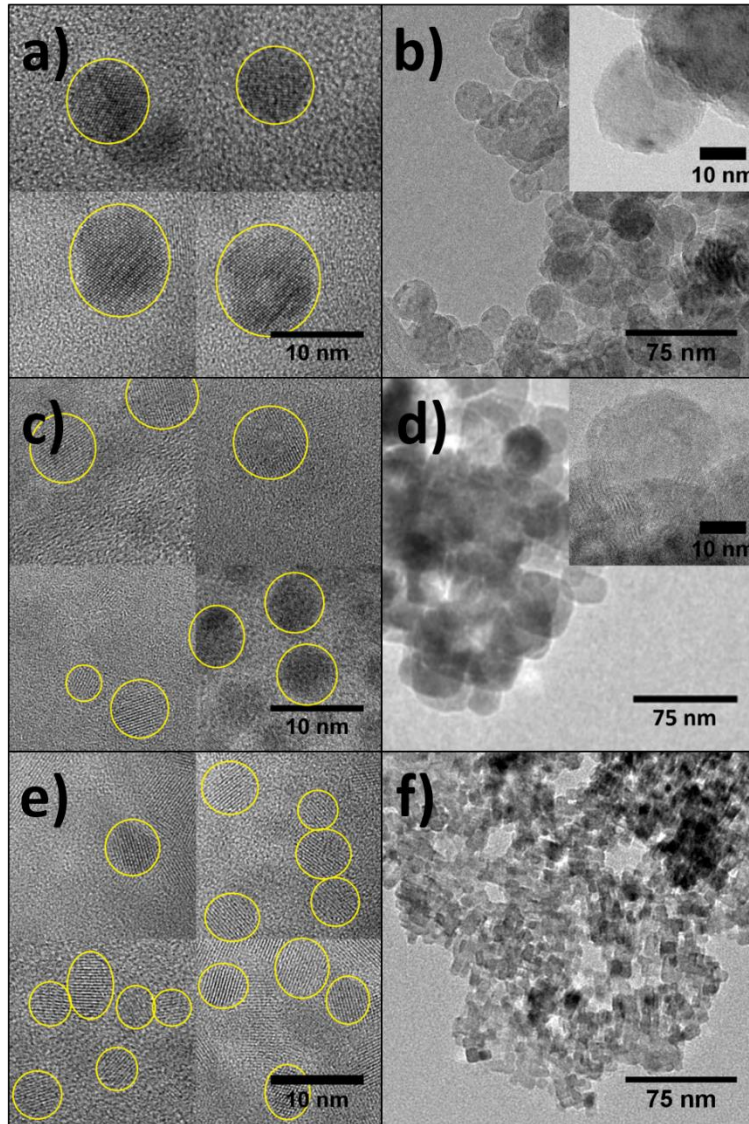


Figure 1.2 TEM pictures of a) CN10, b) CN480, c) CK10, d) CK480, e) SN10 and f) SN480.

The growth of the average dimension of the NPs is proved also by TEM measurement, as shown in figure 1.2. It is worth to note that the lattice constant does not change as the NPs size increases. The average value for the cubic lattice constant is $5.462 \pm 0.002 \text{ \AA}$ for CaF₂ NPs that is coherent with the values found in literature^{31,32}

and $5.802 \pm 0.002 \text{ \AA}$ for the SrF_2 NPs, that is consistent with the values found in literature.³³

Emission properties

As it is well known, when a trivalent lanthanide ion is inserted as dopant in CaF_2 or SrF_2 it substitutes Ca^{2+} or Sr^{2+} , therefore a charge compensation is needed in order to maintain the charge neutrality of the structure^{10,16}. In this work Na^+ and K^+ monovalent ions, provided by sodium or potassium citrate, can substitute Ca^{2+} or Sr^{2+} ions to providing charge compensation^{17,19}. Eu^{3+} ions could occupy the metal site (Ca^{2+} or Sr^{2+}) with different symmetry. Eu^{3+} ions could be accommodated in different sites subjected to different crystal fields, that influence the emission features. The emission of Eu^{3+} ions is particularly sensitive to their local symmetry^{16,20,34}, and this behavior makes Eu^{3+} ions a good sensor for investigating through spectroscopy how trivalent lanthanides accommodate in a host. In figure 1.3 the emission of the CN10 samples under 465 nm excitation and the energy levels scheme for Eu^{3+} ions are shown. The emission spectra for CK10 and SN10 samples are very similar to the one for the CN10 sample and they are shown in Figure A2 (APPENDIX A).

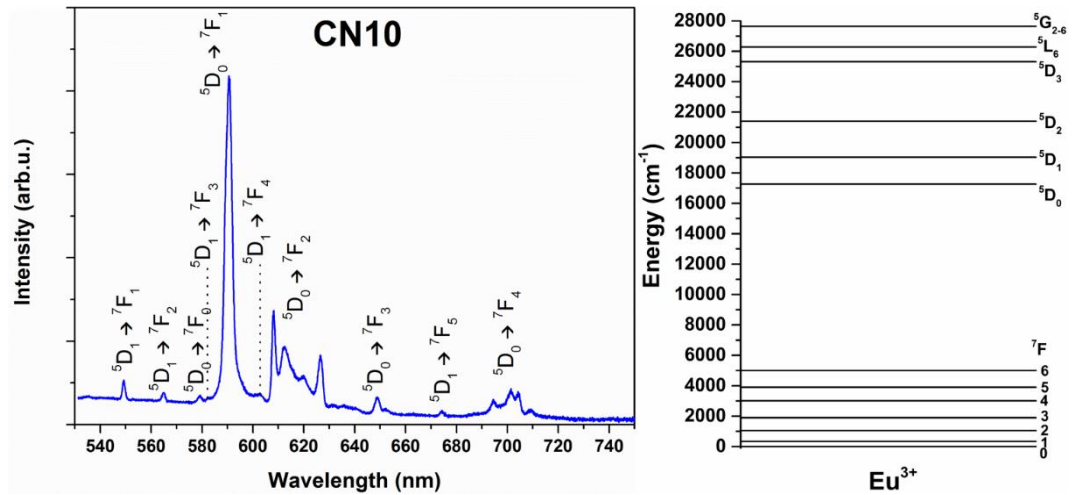


Figure 1.3 Emission spectrum of the CN10 sample upon 465 nm excitation (left) and energy levels scheme for Eu^{3+} ions (right).

As it is shown in Figure 1.3, the emission spectrum presents the typical Eu^{3+} emission bands due to the ${}^5D_1 \rightarrow {}^7F_J$ ($J = 1, 0; J = 1, 2, 3, \dots$) transitions. The strongest features are due to the ${}^5D_0 \rightarrow {}^7F_1$ transition around 590 nm and ${}^5D_0 \rightarrow {}^7F_2$ transition around 615 nm. The ${}^5D_0 \rightarrow {}^7F_1$ transition is a magnetic dipole transition and it is usually largely independent from the Eu^{3+} local environment, while the ${}^5D_0 \rightarrow {}^7F_2$ transition is an electric dipole (ED) transition that is defined as a so-called “*hypersensitive transition*” since its intensity strongly depends on the crystal field symmetry³⁴.

In Figure 1.4, the excitation spectra that have been measured considering the emissions at 589 and 611 nm, corresponding to the ${}^5D_0 \rightarrow {}^7F_1$ and ${}^5D_0 \rightarrow {}^7F_2$ transitions, respectively, are shown. As it can be seen in Figure 1.4, the excitation spectra are similar and present the typical excitation bands for the Eu^{3+} ions, corresponding to transitions starting from the 7F_0 level to higher excited states. The strongest band centered at 395 nm is due to the ${}^7F_0 \rightarrow {}^5L_6$ transition. The differences in the excitation spectra for the

two different emission wavelengths mean that the two transitions follow different excitation pathways. The first difference that can be noticed is that for the excitation spectrum measured at 589 nm emission, the ${}^7F_0 \rightarrow {}^5D_1$ transition is particularly intense, while for the 611 nm emission this transition is much weaker. Another important difference between the excitation spectra at the two different emission wavelengths concerns the ${}^7F_0 \rightarrow {}^5D_2$ transition, that is an electric dipole hypersensitive transition³⁴. The inset in Figure 1.4 clearly shows five Stark transitions, around 465 nm, for the ${}^7F_0 \rightarrow {}^5D_2$ transition in the case of 589 nm emission, while for the excitation spectrum at 611 nm emission only one dominant band peaked 465 nm is observed.

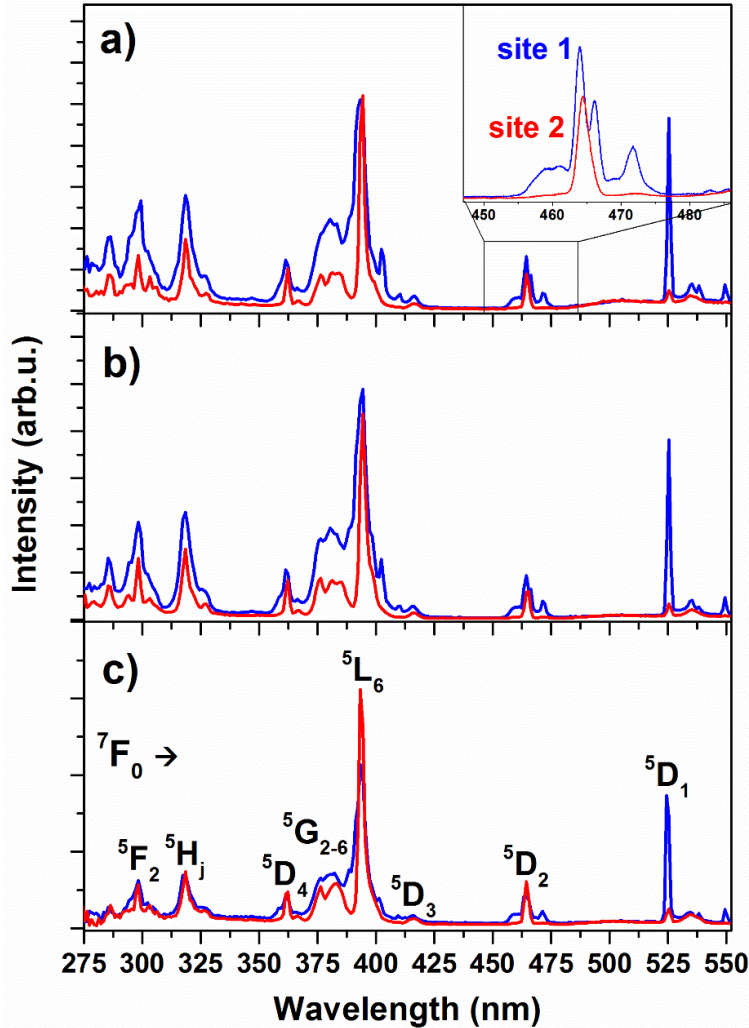


Figure 1.4 Room temperature excitation spectra for a) CN10, b) CK10, c) SN10 samples. Blue lines are the excitations for the 589 nm emission (site 1) and red lines for the 611 nm emission (site 2). In the inset the magnification of the ${}^7F_0 \rightarrow {}^5D_2$ transition for the CN10 sample. The spectra were acquired respecting the same experimental conditions, only the emission wavelength was changed.

These features suggest the presence of at least two different sites with different symmetry accommodating the Eu^{3+} ions in our samples, corresponding to different local crystal fields, generating different splitting of the 5D_2 Stark levels. The excitation site represented by the blue graph in figure 1.4 will be denoted hereafter as site 1, while the site represented by the red graph will be denoted as site 2. Site 1 can be identified

as the P site shown by Hamers et al.¹⁰ for an Eu³⁺ doped CaF₂ single crystal, since the two central Stark bands of its ⁷F₀ → ⁵D₂ transition perfectly match the two excitation bands reported by Hamers for the so-called P site at 464 nm and 466.5 nm. Hamers also reports two excitation bands for the ⁷F₀ → ⁵D₁ transition around 525.5 nm, separated by 0.2 nm, but in our measured excitation spectra, shown in Figure 7, they are not resolved due to the lower spectral resolution of the spectrofluorometer used for the measurements, or to a broadening of the bands due to the nanosize. Site 2 could be identified as the so-called Q or R sites shown by Hamers consisting of Eu³⁺ dimers that present multiple Stark bands around 525.5 nm and 465 nm. Because of the lack of resolution of our instrument, the excitation bands for the ⁷F₀ → ⁵D₂ and ⁷F₀ → ⁵D₁ transitions, shown in figure 1.4, cannot be assigned to a single Q or R site, most probably because the bands due to the latter sites are strongly overlapped.

Due to the observed features of the excitation spectrum, site selection spectroscopy has been carried out, using a tunable dye laser in the 455-475 nm range. The site selection spectroscopy emissions are shown in Figure 1.5. From the excitation spectrum, it can be noted that it is possible to select site 1 almost completely by exciting around 460 or 472 nm. On the other hand, site 2 can only partly be selected, because its excitation band peaked at 465 nm is partially overlapping the excitation band of site 1 (see Figure 7). By tuning the laser energy at 461.0, site 1 has been excited and the emission spectrum shows a dominant ⁵D₀ → ⁷F₁ band for all the samples under investigation (see Figure 8, blue lines), although features due to the other transitions are visible. On the other hand, after excitation at 464.5 nm, site 2 has been mainly excited, and the intensity of the ⁵D₀ → ⁷F₂ transition is comparable to the intensity of the ⁵D₀ → ⁷F₁ transition, although contributions from both sites are present.

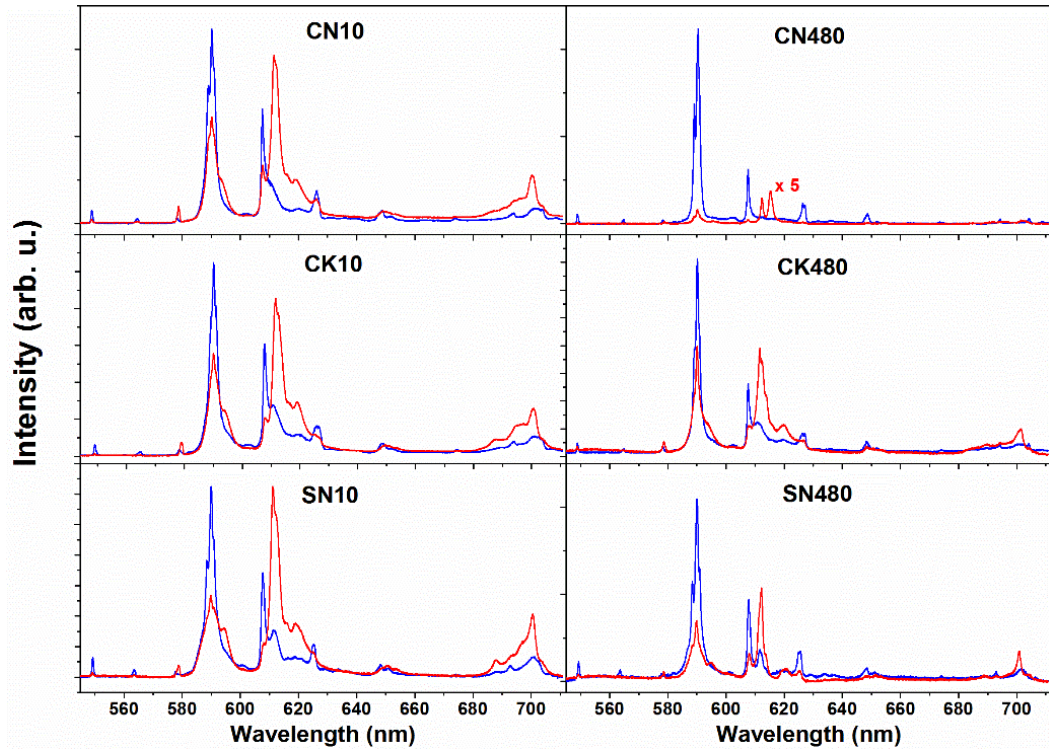


Figure 1.5 Site selection spectroscopy on the 10 min time reaction samples (left column) and 8 hour time reaction samples (right column). Blue spectra ($\lambda_{\text{exc}}=461.0$ nm) are emissions from site 1 and red spectra ($\lambda_{\text{exc}}=464.5$ nm) are emissions from site 2.

The site selection spectroscopy for the samples synthesized with other reaction times are shown in figure A3 (**APPENDIX A**).

It is important to notice that also for site 1 emission a contribution from site 2 is present in all the emission spectra except for the CN480 sample, since the ${}^7F_0 \rightarrow {}^5D_2$ excitation band for site 2 shown in the inset in figure 1.4 is extremely weak at 461.0 nm but not completely absent. Therefore, because of the laser power, also site 2 can be partially excited at 461.0 nm. The absence of site 2 contribution in the site selected emission of site 1 for the CN480 sample could be attributed to the fact that almost all Eu^{3+} ions are located in site 1 while only few of them are located in site 2. This hypothesis is also supported by the extremely low site 2 emission with respect to site 1 emission for the CN480 sample.

From the observed emission spectra it is possible to make some inferences about the site symmetry surrounding Eu^{3+} ions^{11,20,34-36}. First, it can be noticed that for site 1 the ${}^5D_0 \rightarrow {}^7F_0$ transition is weak or almost absent, while for site 2 it is clearly observable around 580 nm. This transition is ED forbidden, but thanks to j-mixing effect²⁵ the emission is measurable. The presence of the ${}^5D_0 \rightarrow {}^7F_0$ band indicates that the possible site 2 local symmetries for the lanthanide ions are C_s , C_1 , C_2 , C_3 , C_4 , C_6 , C_{2v} , C_{3v} , C_{4v} , and C_{6v} ^{20,34}.

Since for site 1 the ${}^5D_0 \rightarrow {}^7F_0$ transition is absent or very weak (probably because of contributions from site 2), it can be inferred that its symmetry is higher than for site 2.

Another clear feature of the emission spectra of all samples is that the relative intensity between the emission around 612 nm (${}^5D_0 \rightarrow {}^7F_2$ transition) and 590 nm (${}^5D_0 \rightarrow {}^7F_1$ transition) is different for excitation in the two different sites and it changes for samples prepared with increased reaction time. The ratio between the ${}^5D_0 \rightarrow {}^7F_2$ integrated intensity transition and the magnetic dipole ${}^5D_0 \rightarrow {}^7F_1$ one is called asymmetry ratio, an indicator of the local Eu^{3+} symmetry^{20,26,34}, defined as

$$R = \frac{A_{612}}{A_{590}} \quad (1.1)$$

where A_{612} is the integrated area of the 612 nm emission band and A_{590} is the integrated area of the 590 nm emission band. An increase of the asymmetry ratio points to a decrease of symmetry and vice-versa. The asymmetry ratio for site 1 was calculated for all the samples synthesized with different reaction times, and it is shown in figure 1.6. Since site selection for site 2 was not possible because of the overlapping of its excitation spectra with the one of site 1, its asymmetry ratio was not calculated.

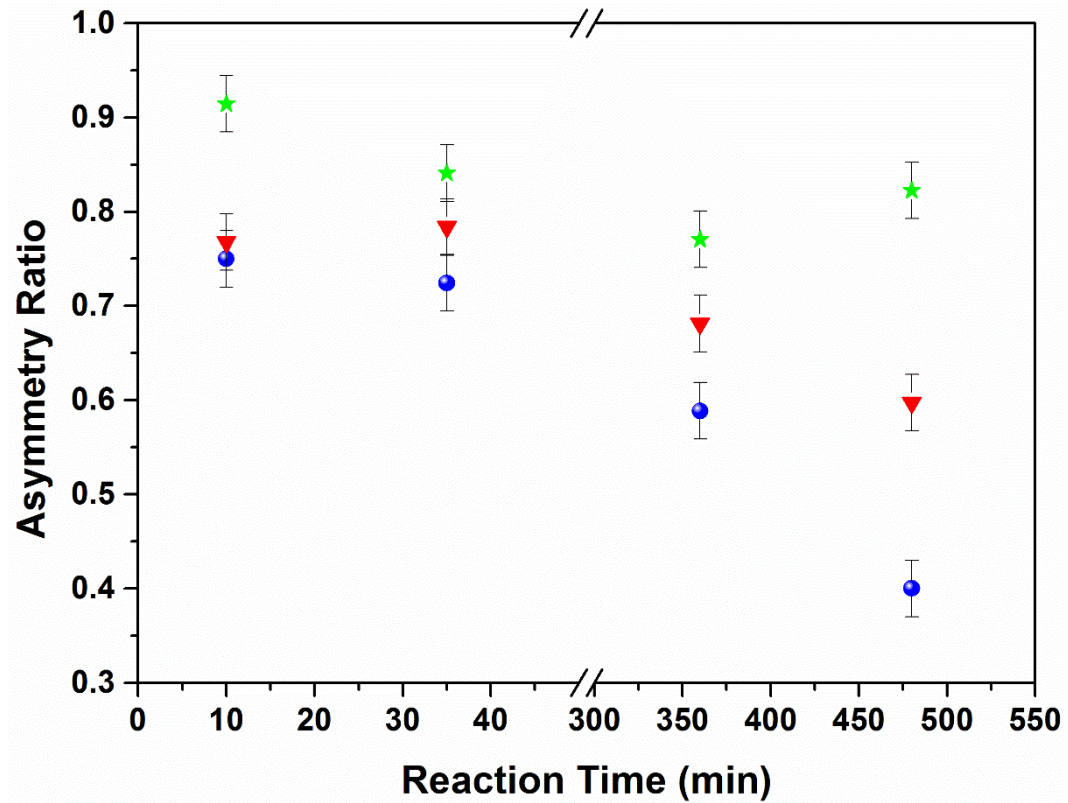


Figure 1.6 Asymmetry ratios for the CN samples (blue dots), CK samples (green stars), SN samples (the red triangles) synthesized at different reaction times ($\lambda_{exc}=461.0$ nm).

For the CN and SN samples R tends to decrease when the reaction time increases, but for the CK480 samples R increases with respect to the CK360 sample. This difference can be attributed to the narrowing of the ${}^5D_0 \rightarrow {}^7F_1$ emission band. The most important thing to notice is that however the R value for the CK480 sample is lower than the R value for the CK10 sample, meaning that the symmetry of site 1 for the CK480 sample is higher than for the CK10 sample. It is important to notice that the behavior of CaF_2 co-doped with Eu^{3+} and Na^+ is different from CaF_2 co-doped with Eu^{3+} and K^+ and from SrF_2 co-doped with Eu^{3+} and Na^+ . In fact, R for the CN samples is always lower than R for the other samples. For the samples synthesized with a 10 minutes reaction, CN10 and SN10 present almost the same R value, around 0.75, that means a similar average symmetry, while the R value for the CK10 sample is around 0.9. Also the behavior of R for the three kinds of sample are different when the reaction time increases. For the CN samples there is a decrease of 47% between the value of R for the 10 min reaction time sample and the 8 hours reaction time sample, while for the CK samples R presents a decrease of 10% and for the SN samples the decrease is 22%. Overall, it is possible to infer that by increasing the reaction time the symmetry of site 1 becomes higher.

The main difference in the R behavior is between the CN and the CK samples, while R for the CN samples undergoes a wide decrease when the reaction time increases, for the CK samples the decrease is much lower. This can be attributed to the different co-doping ions, Na^+ for the CN samples and K^+ for the CK samples, that have been used to compensate the Eu^{3+} ions extra charge when they substitute Ca^{2+} ions.

To evaluate the relative percentage of the different metal ions present in the NPs, elemental measurements using ICP-MS technique were carried out. The results obtained with the ICP-MS investigation are shown in Table 1.2. ICP-MS measurements for the SN samples are not shown because of instrumental problems.

Table 1.2. ICP-MS results for the CN and CK samples

Sample Name	%Eu ³⁺	%Na ⁺	%K ⁺
CN10	3.3	4.1	
CN35	3.7	3.6	
CN360	3.7	3.3	
CN480	3.5	2.7	
CK10	3.3		0.8
CK35	3.8		0.8
CK360	3.4		0.9
CK480	3.6		1.3

As it is shown in Table 1.2, although the nominal Eu³⁺ molar concentration is 1 mol% with respect to the total metal ions, ICP-MS measurements show that the percentage of Eu³⁺ ions in the NPs is higher than 3%. The amount of Eu³⁺ ions that substitute Ca²⁺ ions is almost the same for the CN and CK samples, meaning that the substitution of Ca²⁺ ions by Eu³⁺ ions has almost the same efficiency. It is important to notice that, although the concentration of Eu³⁺ ions is almost the same for the CN and the CK samples, the concentration of Na⁺ ions in the CN samples is almost the same of Eu³⁺ ions, while in the CK samples K⁺ concentration is much lower. This means that Na⁺ ions are more efficient in substituting Ca²⁺ ions in the CaF₂ structure than K⁺ ions. This behavior can be ascribed to the different ionic size of the Na⁺ and K⁺ ions. The ionic radius of Na⁺ in an 8-fold coordination is 1.32 Å, and of K⁺ it is 1.65 Å³⁷. Therefore, since Ca²⁺ ionic radius is 1.26 Å³⁷ it is possible to assume that Na⁺ ions can substitute Ca²⁺ ions more efficiently than K⁺ ions because of Na⁺ and Ca²⁺ similar ionic radius, while K⁺ ionic radius is 30% larger than Ca²⁺ one and therefore the substitution is much more difficult.

To investigate the contribution of the different Stark sub-levels to the emission spectrum, emission measurements at 77 K were also carried out. The local symmetry of the Eu³⁺ ions can be investigated considering the number of transitions due to Stark splitting observed for the bands^{16,20,34}, because the number of the bands depends on the crystal field splitting due to the local lanthanide symmetry.

In figure 1.7, the emission spectra for the CN480 sample under site selection are shown. The spectra for the other samples are shown in figure A4 of **APPENDIX A**.

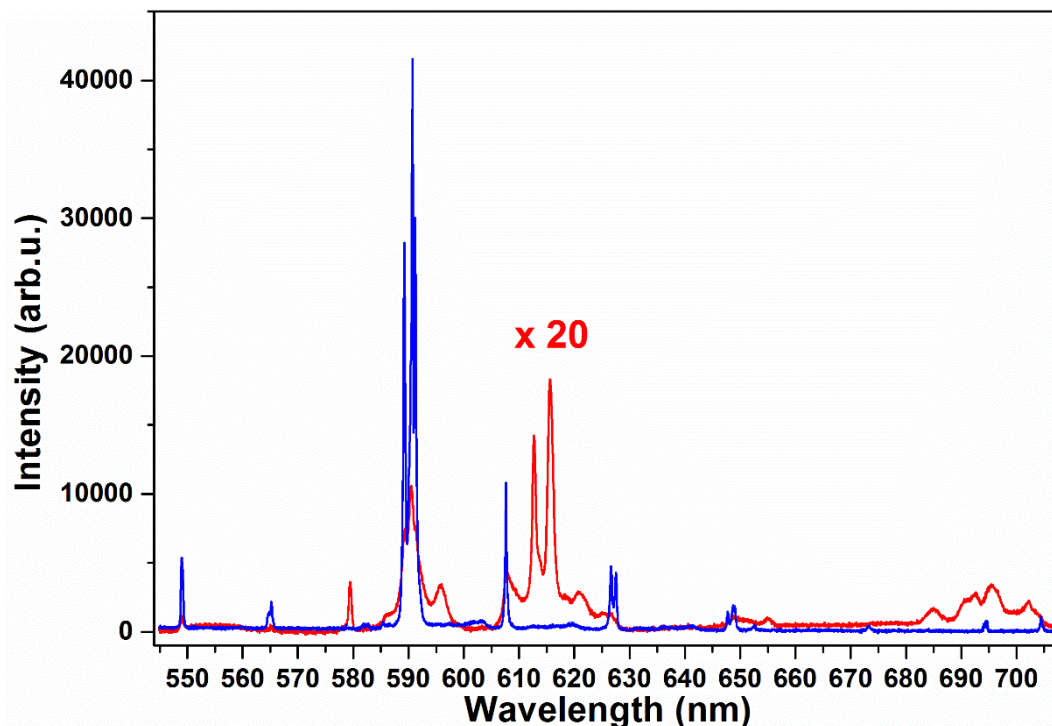


Figure 1.7 77 K emission spectra for the CN480 sample. Blue line: $\lambda_{\text{exc}} = 461.0$ nm; Red line: $\lambda_{\text{exc}} = 464.5$ nm.

The emission of the CN480 sample is shown since it is the only sample where site 1 can be perfectly selected by exciting at 461.0 nm. As can be noticed in figure 1.7, all the bands show a narrowing behavior with respect to the ones at room temperature (figure 1.5). As it was found also at room temperature, the $^5D_0 \rightarrow ^7F_0$ transition for site 1 is not present, and therefore the one observed for excitation at 464.5 nm can be attributed only to site 2. This confirms that the Eu^{3+} ions accommodated in site 1 have a higher symmetry than the ones in site 2. Other well defined narrow bands are visible for the $^5D_0 \rightarrow ^7F_1$ and $^5D_0 \rightarrow ^7F_2$ transitions in the 580 – 630 nm emission range. In figure 1.8, a detailed section of the emission spectra is shown, presenting the emission bands of the $^5D_0 \rightarrow ^7F_0$, $^5D_0 \rightarrow ^7F_1$ and $^5D_0 \rightarrow ^7F_2$ transitions. All the 77K emission spectra, shown in **APPENDIX A** figure A4, present the same behavior of the spectra of CN480 sample, although some multiple site emission is present. For the low reaction time samples the emission bands are broader.

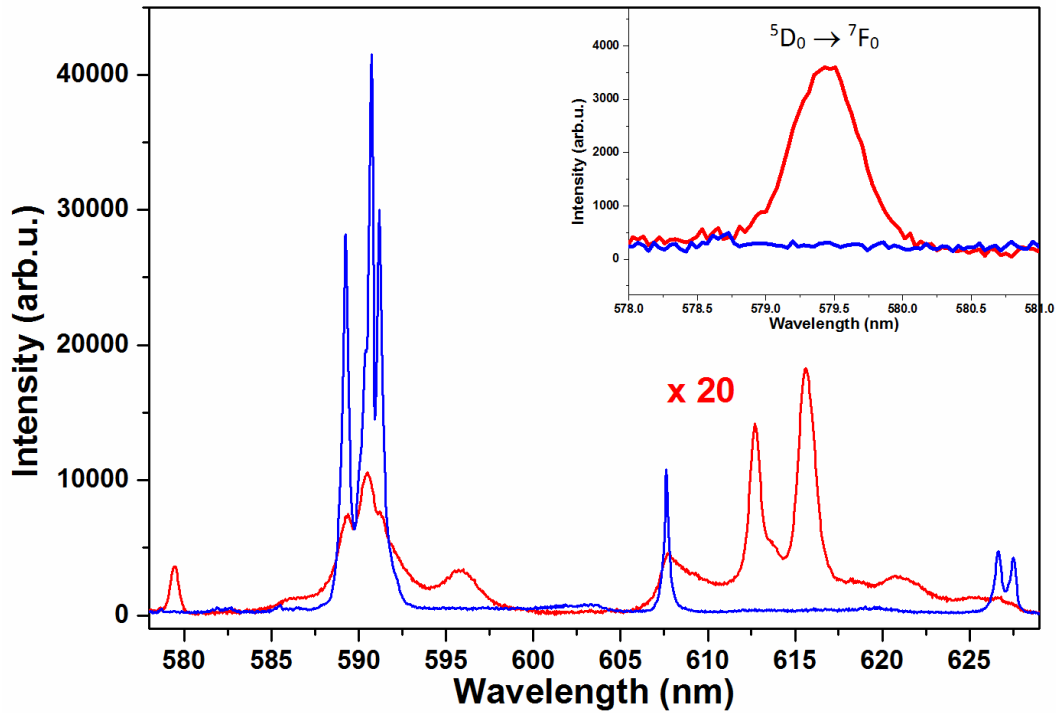


Figure 1.8 Emissions bands due to the ${}^5D_0 \rightarrow {}^7F_0$, ${}^5D_0 \rightarrow {}^7F_1$ and ${}^5D_0 \rightarrow {}^7F_2$ transitions for the CN480 sample at 77 K. Blue line: $\lambda_{exc} = 461.0$ nm; Red line: $\lambda_{exc} = 464.5$ nm. In the inset a zoom on the emission band of the ${}^5D_0 \rightarrow {}^7F_0$ transition, with site 1 emission magnified 20 times.

As it can be seen in Figure 1.8, the emission of both the sites presents three bands for the ${}^5D_0 \rightarrow {}^7F_1$ transition around 590 nm. For site 2 the ${}^5D_0 \rightarrow {}^7F_0$ transition is present, therefore its possible site symmetry is restricted to C_{2v} , C_2 , C_s or C_1 ^{20,34}. It is not possible to perfectly assign the symmetry of site 2 since it presents multiple site emission when excited at 464.5 nm, and the emission bands are not well resolved even at 77 K. Like for the room temperature emission spectra, site 1 presents no ${}^5D_0 \rightarrow {}^7F_0$ transition and three bands for the ${}^5D_0 \rightarrow {}^7F_2$ transition, the first at 607.5 nm, and the other 2 at 627 nm and 627.5 nm. The emission bands of the ${}^5D_0 \rightarrow {}^7F_2$ transition perfectly match those for the P site found by Hamers et al. in Eu^{3+} doped CaF_2 single crystals¹⁰ with the same Stark splitting. It is worth noting that Hamers do not assign a symmetry for the P site. Since the ${}^5D_0 \rightarrow {}^7F_0$ transition is absent, and both the ${}^5D_0 \rightarrow {}^7F_1$ and ${}^5D_0 \rightarrow {}^7F_2$ transitions show three band due to Stark splittings, it is possible to assign the D_2 symmetry to site 1^{20,34}. As far as we know, this is the first time that a site with D_2 symmetry has been found and assigned for Eu^{3+} ions in CaF_2 or SrF_2 .

To confirm the already presented results the lifetimes of the 5D_0 level for site 1 for all the samples were acquired and are shown in figure 1.9.

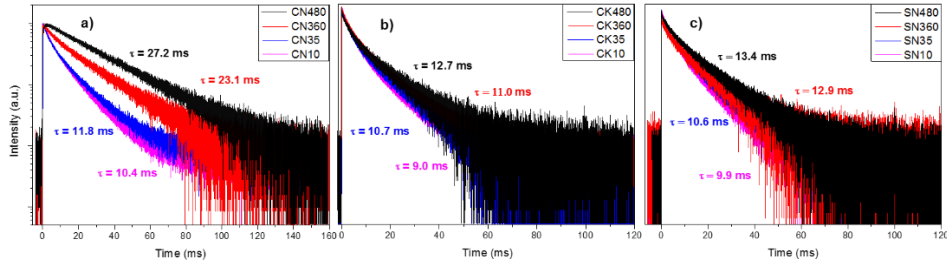


Figure 1.9 Decay times in logarithmic scale of the 5D_0 state, in **a)** the CN samples, in **b)** the CK samples, in **c)** the SN samples ($\lambda_{exc}=461.0$ nm)

The 5D_0 state presents long lifetimes, as also reported by Hamers et al. for the P site (16 ms)¹⁰. Since the decay curves present a non-exponential behavior (apart from the CN480 sample) the effective lifetime has been calculated using the formula³⁸:

$$\tau = \frac{\int_0^{t_f} t \times f(t) dt}{\int_0^{t_f} f(t) dt} \quad (1.2)$$

where $f(t)$ is the measured decay curve and $t_f \gg \tau$. For site 1, the 5D_0 state lifetime increases by increasing the reaction time, but for CK and SN (figures 1.9b and 1.9c) there is only a slight difference in the lifetime of the different samples (it varies from 9.0 ms for CK10 to 12.7 ms for CK480 and from 9.9 ms for SN10 to 13.4 ms for SN480). For the CK and SN samples the decay curves do not present a single exponential behavior, meaning that the emission is not from Eu^{3+} ions accommodated in a single site but probably from both site 1 and 2. Differently, CN samples (figure 1.9a) show a large difference between samples with different reaction times. Every CN sample at a defined reaction time presents a higher lifetime than the CK or SN sample with similar reaction time.

Furthermore, the difference between CN10, CN35, CN360 and CN480 is sharp. The lower lifetime for a CN sample is 10.4 ms (CN10), while it is 27.2 ms for the CN480 sample. To the best of our knowledge, a decay time of 27.2 ms is the longest decay time ever measured for the 5D_0 level of Eu^{3+} . Also the shape of the lifetime curve changes for CN depending on the reaction time: the behavior of CN10 and CN35 resembles the behavior of CK and SN samples, while CN360 and CN480 exhibit an almost single exponential behavior. This confirms the behavior of the emission obtained with site selection spectroscopy that show that for the CN480 sample the emission from site 2 has almost disappeared. In fact, such a long lifetime means that Eu^{3+} is located in the site with higher symmetry (site 1, D_2 symmetry). The rise-decay behavior that can be seen in the decay-time curves of the CN samples (especially for CN360 and CN480) can be ascribed to a slow $^5D_1 \rightarrow ^5D_0$ feeding²⁰.

From the lifetime measurements it is possible to infer that the contribution of site 1 to the overall emission increases when the synthesis reaction time increases. It is more evident for the CN samples, where the lifetime of the 5D_0 state shows an almost perfect exponential behavior for the CN480 sample (confirmed also by the high emission intensity of site 1 with respect to site 2 as it can be seen in figures 1.5, 1.7 and 1.8).

The comparison between the lifetimes of the CN and CK samples also confirms the ICP-MS results, since Na^+ ions can substitute Ca^{2+} ions at least two times more

than K^+ ions, and the amount of Na^+ ions in the CN samples is similar to the amount of Eu^{3+} ions. Therefore, for the CN samples by increasing the reaction time, more Na^+ ions can be arranged in a D_2 symmetry around Eu^{3+} ions. This behavior can be seen also for the CK and SN samples, but with less efficiency. Moreover, Na^+ is known to favor the presence of symmetric sites when co-doped with lanthanide ions³⁹.

1.4 Conclusion

Lanthanide doped CaF_2 and SrF_2 NPs have been prepared by a one-step, simple and

environmental friendly hydrothermal technique. The NPs are easily dispersible in water solutions, without the need of any post-synthesis reaction. XRD confirmed the purity of the CaF_2 and SrF_2 crystalline phases. Site selective laser spectroscopy allowed to find the symmetry sites of Eu^{3+} ions in the three different kinds of NPs and to investigate the relative populations of the different sites by varying the reaction time. The 5D_0 level lifetime measured for the CN480 sample (27.2 ms) is the longest ever measured for Eu^{3+} ions. This leads to some possible applications in biomedicine, for time resolved imaging spectroscopy, to eliminate the autofluorescence of the biological tissues, for instance using Fluorescence Lifetime Imaging Microscopy⁴⁰.

In the next future further studies will be carried out using multiphoton excitation, in order to evaluate the possibility to use these nanoparticles to work using NIR exciting source for potential *in vivo* applications.

REFERENCES

- 1 Hillhouse, H. W. & Beard, M. C. Solar cells from colloidal nanocrystals: Fundamentals, materials, devices, and economics. *Current Opinion in Colloid & Interface Science* **14**, 245-259, doi:10.1016/j.cocis.2009.05.002 (2009).
- 2 Di, W. *et al.* Photoluminescence, cytotoxicity and in vitro imaging of hexagonal terbium phosphate nanoparticles doped with europium. *Nanoscale* **3**, 1263-1269, doi:10.1039/c0nr00673d (2011).
- 3 Bunzli, J. C. Benefiting from the unique properties of lanthanide ions. *Accounts of chemical research* **39**, 53-61, doi:10.1021/ar0400894 (2006).
- 4 Ma, Z. Y. *et al.* Synthesis and bio-functionalization of multifunctional magnetic Fe₃O₄@Y₂O₃:Eu nanocomposites. *Journal of materials chemistry* **19**, 4695-4700, doi:10.1039/b901427f (2009).
- 5 Dong, N. N. *et al.* NIR-to-NIR two-photon excited CaF₂:Tm³⁺, Yb³⁺ nanoparticles: multifunctional nanoprobes for highly penetrating fluorescence bio-imaging. *ACS nano* **5**, 8665-8671, doi:10.1021/nn202490m (2011).
- 6 Reisfeld, R. New developments in luminescence for solar energy utilization. *Optical Materials* **32**, 850-856, doi:10.1016/j.optmat.2010.04.034 (2010).
- 7 van der Ende, B. M., Aarts, L. & Meijerink, A. Lanthanide ions as spectral converters for solar cells. *Physical chemistry chemical physics : PCCP* **11**, 11081-11095, doi:10.1039/b913877c (2009).
- 8 Chatterjee, D. K., Rufaihah, A. J. & Zhang, Y. Upconversion fluorescence imaging of cells and small animals using lanthanide doped nanocrystals. *Biomaterials* **29**, 937-943, doi:10.1016/j.biomaterials.2007.10.051 (2008).
- 9 Jouart, J. P., Bissieux, C., Mary, G. & Egee, M. A spectroscopic study of Eu³⁺ centres in SrF₂ using a site-selective excitation technique. *Journal of Physics C: Solid State Physics* **18**, 1539-1551, doi:10.1088/0022-3719/18/7/019 (1985).
- 10 Hamers, R. J., Wietfeldt, J. R. & Wright, J. C. Defect Chemistry in CaF₂-Eu³⁺. *J Chem Phys* **77**, 683-692, doi:10.1063/1.443882 (1982).
- 11 Cirillo-Penn, K. M. & Wright, J. C. Laser spectroscopic measurement of point-defect dynamics in Eu³⁺:CaF₂. *Physical Review B* **41**, 10799-10807, doi:10.1103/PhysRevB.41.10799 (1990).
- 12 Laval, J. P., Mikou, A., Frit, B. & Roullet, G. Short-range order in heavily doped CaF₂:Ln³⁺ fluorites: A powder neutron diffraction study. *Solid State Ionics* **28-30**, 1300-1304, doi:10.1016/0167-2738(88)90375-x (1988).
- 13 Pedroni, M. *et al.* Water (H₂O and D₂O) Dispersible NIR-to-NIR Upconverting Yb³⁺/Tm³⁺ Doped MF₂ (M = Ca, Sr) Colloids: Influence of the Host Crystal. *Crystal Growth & Design* **13**, 4906-4913, doi:10.1021/cg401077v (2013).
- 14 Wells, J.-P. R. & Reeves, R. J. Polarized laser selective excitation and Zeeman infrared absorption of C_{4v} and C_{3v} symmetry centers in Eu³⁺-doped CaF₂, SrF₂, and BaF₂ crystals. *Physical Review B* **64**, doi:10.1103/PhysRevB.64.035102 (2001).
- 15 Wells, J.-P. R. & Reeves, R. J. Polarized laser-selective excitation and Zeeman infrared absorption of Sm³⁺ centers in CaF₂ and SrF₂ crystals. *Physical Review B* **61**, 13593-13608, doi:10.1103/PhysRevB.61.13593 (2000).
- 16 Gastev, S. V., Choi, J. K. & Reeves, R. J. Laser spectroscopy of Eu³⁺ cubic centers in the CaF₂ bulk single crystal. *Physics of the Solid State* **51**, 44-49, doi:10.1134/s1063783409010041 (2009).

- 17 Jones, G. D. & Reeves, R. J. Na⁺, Li⁺ and cubic centres in rare-earth-doped CaF₂ and SrF₂. *Journal of Luminescence* **87-89**, 1108-1111, doi:10.1016/s0022-2313(99)00559-1 (2000).
- 18 Martin, P., Hamaidia, A. & Margerie, J. Paramagnetic colour centres in SrF₂:Na⁺. *Journal of Physics C: Solid State Physics* **18**, 5947-5961, doi:10.1088/0022-3719/18/32/007 (1985).
- 19 Su, L. *et al.* Sites structure and spectroscopic properties of Yb-doped and Yb, Na-codoped CaF₂ laser crystals. *Chemical Physics Letters* **406**, 254-258, doi:10.1016/j.cplett.2005.02.122 (2005).
- 20 Ju, Q. *et al.* Optical Spectroscopy of Eu³⁺-Doped BaFCl Nanocrystals. *The Journal of Physical Chemistry C* **113**, 2309-2315, doi:10.1021/jp809233p (2009).
- 21 Werts, M. H. V., Jukes, R. T. F. & Verhoeven, J. W. The emission spectrum and the radiative lifetime of Eu³⁺ in luminescent lanthanide complexes. *Physical Chemistry Chemical Physics* **4**, 1542-1548, doi:10.1039/b107770h (2002).
- 22 Pedroni, M. *et al.* Lanthanide doped upconverting colloidal CaF₂ nanoparticles prepared by a single-step hydrothermal method: toward efficient materials with near infrared-to-near infrared upconversion emission. *Nanoscale* **3**, 1456-1460, doi:10.1039/c0nr00860e (2011).
- 23 Forsyth, J. M. Single-Frequency Operation of the Argon-Ion Laser at 5145 Å. *Applied Physics Letters* **11**, 391, doi:10.1063/1.1728226 (1967).
- 24 Pandurangappa, C., Lakshminarasappa, B. N. & Nagabhushana, B. M. Synthesis and characterization of CaF₂ nanocrystals. *Journal of Alloys and Compounds* **489**, 592-595, doi:10.1016/j.jallcom.2009.09.118 (2010).
- 25 Zahedifar, M., Sadeghi, E., Mozdianfard, M. R. & Habibi, E. Synthesis, characteristics and thermoluminescent dosimetry features of gamma-irradiated Ce doped CaF₂ nanophosphor. *Applied radiation and isotopes : including data, instrumentation and methods for use in agriculture, industry and medicine* **78**, 125-131, doi:10.1016/j.apradiso.2013.04.029 (2013).
- 26 Song, L., Gao, J. & Song, R. Synthesis and luminescent properties of oleic acid (OA)-modified CaF₂: Eu nanocrystals. *Journal of Luminescence* **130**, 1179-1182, doi:10.1016/j.jlumin.2010.02.017 (2010).
- 27 Grass, R. N. & Stark, W. J. Flame synthesis of calcium-, strontium-, barium fluoride nanoparticles and sodium chloride. *Chemical communications*, 1767-1769, doi:10.1039/b419099h (2005).
- 28 Jin, Y., Qin, W. & Zhang, J. Preparation and optical properties of SrF₂:Eu³⁺ nanospheres. *Journal of Fluorine Chemistry* **129**, 515-518, doi:10.1016/j.jfluchem.2008.03.010 (2008).
- 29 Sun, J., Xian, J., Zhang, X. & Du, H. Hydrothermal synthesis of SrF₂:Yb³⁺/Er³⁺ micro-/nanocrystals with multiform morphologies and upconversion properties. *Journal of Rare Earths* **29**, 32-38, doi:10.1016/s1002-0721(10)60396-1 (2011).
- 30 Wang, J. *et al.* High-Pressure Behaviors of SrF₂Nanocrystals with Two Morphologies. *The Journal of Physical Chemistry C* **117**, 615-619, doi:10.1021/jp306742p (2013).
- 31 Gerward, L. *et al.* X-ray diffraction investigations of CaF₂ at high pressure. *Journal of Applied Crystallography* **25**, 578-581, doi:doi:10.1107/S0021889892004096 (1992).
- 32 Bensalah, A., Mortier, M., Patriarche, G., Gredin, P. & Vivien, D. Synthesis and optical characterizations of undoped and rare-earth-doped CaF₂ nanoparticles. *Journal of Solid State Chemistry* **179**, 2636-2644, doi:10.1016/j.jssc.2006.05.011 (2006).

- 33 Bingham, D., Cormack, A. N. & Catlow, C. R. A. Rigid-ion potentials for SrF₂, CaF₂ and GdF₃. *Journal of Physics: Condensed Matter* **1**, 1205 (1989).
- 34 Binnemans, K. Interpretation of europium(III) spectra. *Coordination Chemistry Reviews* **295**, 1-45, doi:10.1016/j.ccr.2015.02.015 (2015).
- 35 Sarkar, S., Hazra, C. & Mahalingam, V. Bright luminescence from colloidal Ln(3+)-doped Ca(0.72)Y(0.28)F(2.28) (Ln=Eu, Tm/Yb) nanocrystals via both high and low energy radiations. *Chemistry* **18**, 7050-7054, doi:10.1002/chem.201103157 (2012).
- 36 Das, S., Amarnath Reddy, A., Ahmad, S., Nagarajan, R. & Vijaya Prakash, G. Synthesis and optical characterization of strong red light emitting KLaF₄:Eu³⁺ nanophosphors. *Chemical Physics Letters* **508**, 117-120, doi:10.1016/j.cplett.2011.04.029 (2011).
- 37 Shannon, R. D. Revised effective ionic radii and systematic studies of interatomic distances in halides and chalcogenides. *Acta Crystallographica Section A* **32**, 751-767, doi:10.1107/s0567739476001551 (1976).
- 38 Passuello, T. *et al.* Structural and optical properties of Vernier phase lutetium oxyfluorides doped with lanthanide ions: interesting candidates as scintillators and X-ray phosphors. *Journal of materials chemistry* **22**, 10639, doi:10.1039/c2jm31317k (2012).
- 39 Hraiech, S. *et al.* Role of monovalent alkali ions in the Yb³⁺ centers of CaF₂ laser crystals. *Radiation Measurements* **45**, 323-327, doi:10.1016/j.radmeas.2009.11.017 (2010).
- 40 Siegel, J. *et al.* Studying Biological Tissue with Fluorescence Lifetime Imaging: Microscopy, Endoscopy, and Complex Decay Profiles. *Applied Optics* **42**, 2995, doi:10.1364/ao.42.002995 (2003).

Chapter 2

Nd³⁺ activated CaF₂ NPs as colloidal nanothermometers in the biological window*

Introduction

Nanostructured materials have become a hot topic in the biomedical field, especially in nanomedicine, where they have been evaluated as efficient tools for diagnostic and therapy for in-vitro and in-vivo applications. In particular, trivalent lanthanide (Ln³⁺) doped nanoparticles (NPs), thanks to the peculiar electronic configuration of Ln³⁺ ions, have shown interesting properties as markers for optical imaging¹⁻², as contrast agents for MRI³⁻⁴ and as nanoheaters for photothermal therapy, in which near infrared (NIR) light is converted into heat⁵⁻⁸. For an optimal anti-cancer treatment based on hyperthermia, one important concern is that the local temperature in the treated area must be confined below 47 °C,⁹ in order to kill efficiently the cancer cells without harming the healthy tissues. Therefore, it is of paramount importance to measure the local temperature in the tissue region where the heat is delivered¹⁰. The underlying idea behind optical nanothermometry is to develop luminescent nanosized materials with high photostability and good emission that can measure the temperature within the spatial resolution of the optical setup for luminescence measurements. Recently, Ln³⁺ doped nanomaterials have been investigated as nanothermometers, since their luminescence is dependent on the temperature¹⁰⁻¹¹. Particularly, the emission intensities of certain energy levels can be used to determine the temperature of the system, exploiting the population of two energy levels that are not too far in energy (typically around 2000 cm⁻¹). The relative population of these two thermally populated energy levels depends on the temperature through the Boltzmann law¹²⁻¹⁵. A ratiometric method considering the relative intensity changes between two emission bands deriving from transitions of thermally populated levels is useful to evaluate the thermometric performance. In fact, the ratiometric method avoids the drawbacks of evaluating a single transition intensity and therefore possible emission variations due to the nanothermometer concentration or excitation source intensity fluctuations. A typical Ln³⁺ ion used in nanothermometry is the Er³⁺ ion, for which the variation of the relative intensities of the emission bands centered at 520 and 540 nm are due to the thermal coupling between the ²H_{11/2} and ²S_{3/2} excited energy levels¹⁶⁻¹⁷. The Tm³⁺ ion has been also considered for nanothermometry¹⁸⁻¹⁹ although in this case, the involved emission bands are centered at 790 and 800 nm, as observed in Tm³⁺, Yb³⁺ codoped CaF₂ NPs. In this particular case, their variations with temperature are due to the thermal coupling of the Stark sublevels of the ³H₄ excited state of Tm³⁺ ion. Another attractive Ln³⁺ ion for thermometry is Nd³⁺, due to its emissions in the NIR region, particularly important for use in nanomedicine as they lie within the transparency windows of biological tissues. Recently, Nd³⁺ has

* Paper published: P. Cortelletti, et al., Nd³⁺ activated CaF₂ NPs as colloidal nanothermometers in the biological window, *Optical Materials* (2016), <http://dx.doi.org/10.1016/j.optmat.2016.11.019>

been studied in some nanomaterials in the first and second biological windows (I-BW, 800-950 nm and II-BW, 1000-1300 nm respectively), where the radiation absorption by the biological tissue is minimal²⁰⁻²¹.

After excitation both in the visible or NIR region around 800 nm, the Nd³⁺ ion can emit in the NIR region, involving Stark transitions between the ⁴F_{3/2} (R₁ and R₂) and ⁴I_J (J = 9/2, 11/2) energy levels^{13, 22}. Recently alkaline earths fluorides, such as CaF₂ and SrF₂, have been studied as hosts for Ln³⁺ ions, due primarily to their low phonon energies that favor Ln³⁺ ion luminescence. In particular, Ln³⁺ doped CaF₂ presents a strong luminescence both in the UV-visible region and the NIR region²³⁻²⁶. Recent in-vitro and in-vivo investigations, showed that CaF₂ NPs doped with lanthanide ions have a low toxicity. In particular, Ln³⁺ doped CaF₂ NPs have low toxicity on HeLa and immune cells^{1, 27-28}, as well as they do not activate human dendritic cells and monocyte response. Moreover, after intravenous injection of the NPs on mice, no modification of their daily life status for one month has been observed. Furthermore, the present CaF₂ NPs are synthesized with a facile, green chemistry procedure at relatively low temperature (<200 °C) and using water as the solvent. Combined these attractive features make Ln³⁺ doped CaF₂ NPs promising materials for biomedical applications.

The aim of this work is to prepare and investigate the spectroscopic properties in the NIR of water colloids of CaF₂ NPs activated with Nd³⁺ ions, in particular for thermometric properties. We used a ratiometric method, using the ratio between the emission intensity of the ⁴F_{3/2} → ⁴I_{9/2} and ⁴F_{3/2} → ⁴I_{11/2} NIR transitions. Gd³⁺ ions have been also added to slow the growth of the NPs during the reaction and permit a finer tuning of the NPs size²⁹⁻³⁰. Since the Gd³⁺ ions provide paramagnetic properties to the host, the obtained NPs can be considered as both optical and MRI contrast agent with thermometric properties²⁷.

Experimental details

Synthesis

The Nd³⁺, Gd³⁺ codoped CaF₂ NPs, with Ca²⁺/Nd³⁺/Gd³⁺ = 0.78/0.03/0.19 nominal metal ratio, were prepared using the hydro thermal method described by Pedroni et al.²⁶. Briefly, in a 50ml Teflon vessel, stoichiometric quantities of reagent grade metal chlorides were dissolved in 7.0ml of deionized water and 20.0 ml of a 1.00 M sodium citrate aqueous solution was added. Then, an ammonium fluoride aqueous solution was added dropwise to the previous solution, to furnish a slight excess of fluoride ions with respect to the stoichiometric amount. The clear solution was treated in an autoclave (DAB-2, Berghof) at 190°C for 3 h. The autoclave was then quenched to room temperature and after washing with acetone, the NPs were collected by centrifugation. The water colloids of the NPs are stable for at least two months.

X-ray powder diffraction

X-ray power diffraction (XRPD) measurements were carried out with a Thermo ARL X'TRA powder diffractometer equipped with a Cu-anode X-ray source ($\lambda = 1.5418 \text{ \AA}$) with a Peltier Si(Li) cooled solid state detector. The patterns were collected with a scan rate of 0.04°/s, with a measurement time of 1.0 s/step. The phase was identified with the PDF-4+ 2014 database (International Centre for Diffraction Data, ICDD). Before the measurements, the samples were homogenized in a mortar with few drops of ethanol. After evaporation of the ethanol, the sample was deposited on a low background sample stage.

TEM

Images of doped CaF₂ NPs were evaluated using a high-resolution (0.17 nm point-to-point) Transmission Electron Microscopy (JEOL 3010) operating at 300 kV, equipped with a Gatan slow-scan CCD camera. The Pebbles software was used to evaluate the NP size distribution³¹.

Spectroscopic setup

The emission spectra of the NPs were measured with a Fluorolog 3 (Horiba-Jobin Yvon) spectrofluorometer, using a Xe lamp as the source, a double excitation monochromator, a single emission monochromator (mod. HR320) and a NIR InGaAs array for the emission detection. A water bath was used to set the sample temperature. All the spectroscopic measurements were performed on water colloidal dispersion of NPs.

Results and discussion

Structural and morphological characterization

The CaF₂ NPs exhibit a cubic single phase (Space group n. 225, $Fm\bar{3}m$), as shown by the XRPD data (see figure 2.1).

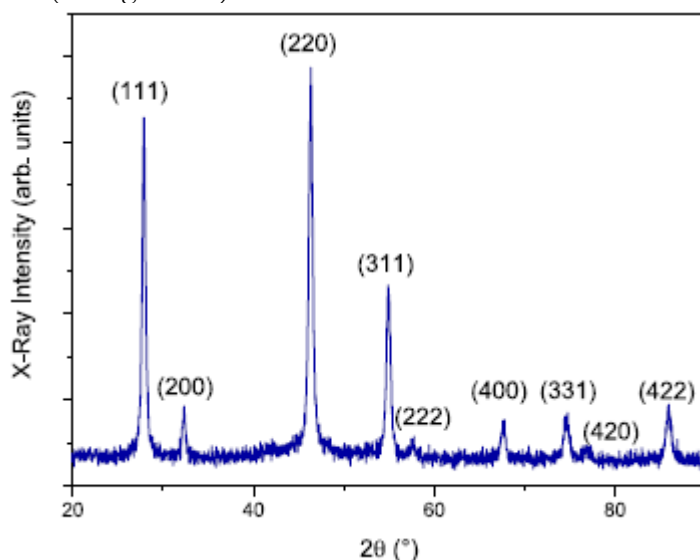


Figure 2.1 X-ray powder diffraction pattern for the CaF₂:Nd³⁺,Gd³⁺ NPs. Miller indexes are shown as (hkl) values.

From the XRPD reflections, considering the cubic structure, a cell parameter of 5.541(1) Å was determined and is larger than the one found for an undoped CaF₂ host ($a = 5.463(1)$ Å³²). It is worth noting that Nd³⁺ or Gd³⁺ ions are prone to substitute the Ca²⁺ ions in the crystal lattice due to their ionic radius similarity ($r_{Nd(III)} = 1.249$ Å, $r_{Gd(III)} = 1.193$ Å, $r_{Ca(II)} = 1.26$ Å, 8-fold coordination³³). For the same reason, Na⁺ ions ($r_{Na(I)} = 1.30$ Å) that are present in the starting reagent (sodium citrate) can be incorporated in the crystal lattice, as already observed for a CaF₂:Yb³⁺, Tm³⁺ nanocrystalline sample that was prepared with the same synthetic procedure²⁶. Due to charge compensation, interstitial fluoride or hydroxide ions can also be present in the crystal host, and therefore electronic repulsions among these anions can explain the increase of the cell parameter found for the NPs under investigation. TEM images and the evaluated particle

size distribution, shown in figure 2.2, demonstrate that the NPs have a round shape with an average size of 9.5 ± 1.9 nm. High Resolution TEM images confirmed the crystallinity of the NPs and the corresponding Fast Fourier Transform (FFT) (figure 2.2, inset) provides information about the orientation of the NPs and its fcc structure.

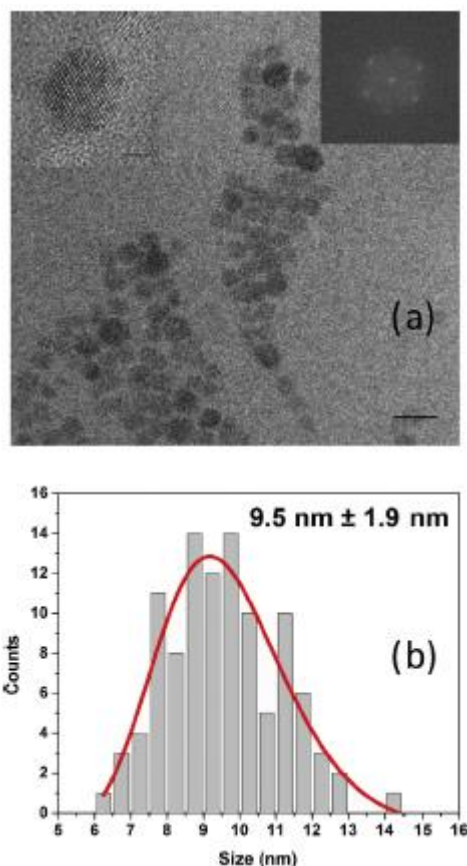


Figure 2.2 (a) TEM image (scale bar = 20 nm) for the $\text{CaF}_2:\text{Nd}^{3+},\text{Gd}^{3+}$ NPs. Right inset: and HRTEM (scale bar = 2 nm); left inset: HREM image and FFT show a NP oriented along the $\langle 101 \rangle$ zone axis showing the $[111]$ and $[020]$ lattice planes. (b) Particle size distribution as calculated by Pebbles software and log-normal fit of the distribution (solid line).

Spectroscopic investigation

The luminescence spectra of a colloidal solution of the Nd^{3+} , Gd^{3+} codoped CaF_2 NPs were measured in the 21-65°C temperature range with an interval of 5°C. The sample was excited by a Xenon lamp radiation with an excitation wavelength of 573 nm. The

Nd^{3+} ions in the CaF_2 host have a rather broad absorption band around 570 nm, as observed by Ma et al.³⁴ and thus, after excitation at 573 nm, the $^4\text{G}_{5/2}$, $^2\text{G}_{7/2}$ excited energy levels of the Nd^{3+} ions are populated. After a rapid non-radiative relaxation, a radiative decay from the $^4\text{F}_{3/2}$ level to lower lying energy levels is observed. Emission spectra for water colloids of the doped NPs, measured at 21°C and at 65°C, are shown in figure 2.3 as representative examples along with the corresponding Nd^{3+} ion energy levels as well as some Stark sublevels. The emission spectrum features two bands located in the 850-915 nm and 1030-1100 nm ranges, corresponding to electronic transitions from the $^4\text{F}_{3/2}$ level to the $^4\text{I}_{9/2}$ and $^4\text{I}_{11/2}$ levels, respectively. Due to the strong overlap among Stark level transitions of the emitting $^4\text{F}_{3/2}$ and the lower lying $^4\text{I}_J$ ($J = 11/2, 9/2$) levels, as well as the fact that several sites are present for Ln^{3+} ions in the

CaF₂ crystal host³⁵⁻³⁸, it was not possible to precisely assign all the transitions for the emission bands.

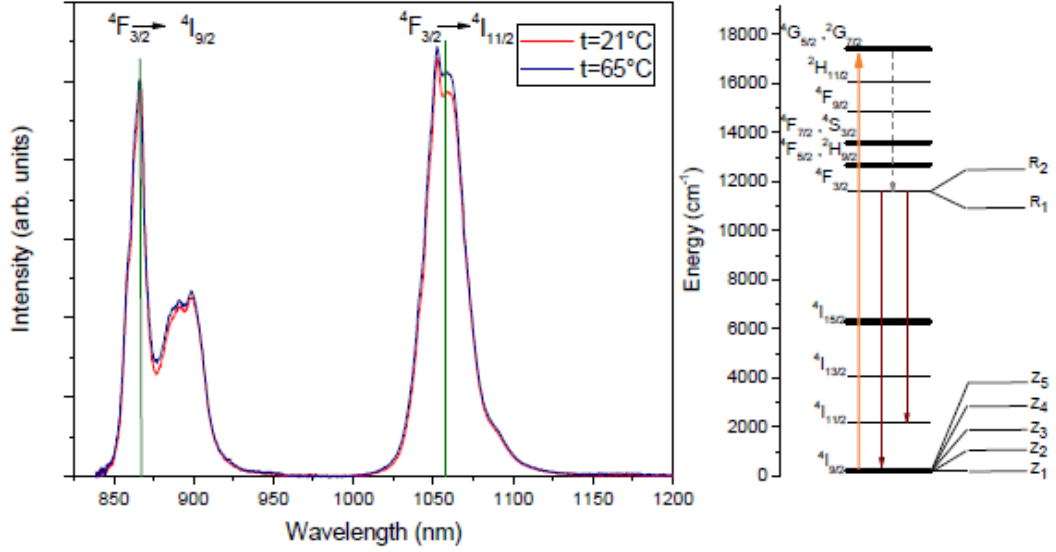


Figure 2.3 Emission spectra at 21 °C and 65 °C for a water colloidal dispersion of the CaF₂:Nd³⁺, Gd³⁺ NPs. The vertical lines indicate the wavelength at which the intensity of the emission bands were considered for the evaluation of the thermometric performance.

Nonetheless, the structured band in the 850-915 nm range is strongly similar to the one found by Rocha et al. for a Nd³⁺ doped LaF₃ host³⁹, where the main emission line was around 864 nm. It is therefore reasonable that the strongest emission at 867 nm is mainly attributed to the R₁→Z₁ Stark level transition of the Nd³⁺ ions (see energy levels in figure 2.3). We have therefore normalized the emission spectra measured at different temperatures to this line and the obtained spectra are shown in figure 2.3. Clear changes of the relative intensity of some emissions are observed on varying the temperature, both in the ⁴F_{3/2} → ⁴I_{9/2} and ⁴F_{3/2} → ⁴I_{11/2} emission range. The emission variations around 900 nm are similar to those found by Rocha et al. for a Nd³⁺ doped LaF₃ host³⁹. These intensity changes can be attributed to variations of the electronic populations of the R₁ and R₂ Stark levels as a function of the temperature. In fact, as the temperature increases, the R₂ level population increases with respect to the R₁ one, following Boltzmann distribution. From the spectra, it can be noted that the most relevant emission intensity changes are observed for the ⁴F_{3/2} → ⁴I_{11/2} band (see figure 2.3). Therefore, we have evaluated the thermometric performances taking into account the intensity ratio between the emission at 1058 nm and at 867 nm (indicated as vertical lines in figure 2.3), according to the ratiometric method. We have therefore calculated the “Fluorescence Intensity Ratio” (FIR) of the intensity of emission bands of Nd³⁺, defined as:

$$FIR = \frac{I_{1058}}{I_{867}} \quad (2.1)$$

where I is the intensity of the emission band at the chosen wavelength. In figure 2.4, the variations of the FIR on changing the temperature are shown. The FIR values calculated from the emission spectra at various temperatures increase on increasing the temperature in the 22 - 65 °C range, following a linear behavior. The increase of the FIR vs temperature can be therefore explained by the increase of the population of the

higher energy R_2 Stark level with respect to the R_1 one (see figure 2.3). The absolute thermal sensitivity (S) can be defined as^{5,40}:

$$S = \left| \frac{\partial FIR}{\partial T} \right| \quad (2.2)$$

where T is the temperature. From a linear fit of the FIR values vs temperature, a thermal sensitivity of $(1.19 \pm 0.04) \cdot 10^{-3} \text{ K}^{-1}$ has been evaluated from the slope of the straight line (see figure 2.4).

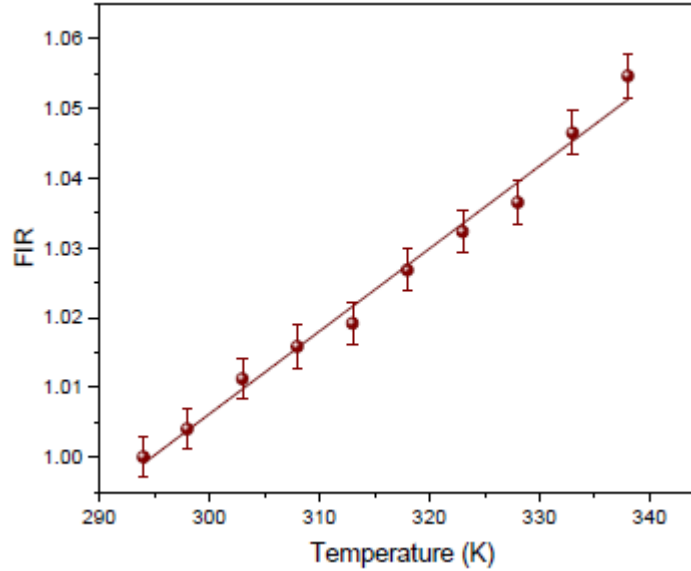


Figure 2.4 FIR (defined in Eq. (1)) behavior as a function of the temperature for a water colloidal dispersion of $\text{CaF}_2:\text{Nd}^{3+}, \text{Gd}^{3+}$ NPs.

Nonetheless, in order to compare the thermal performances between different nanothermometers, it is very useful to evaluate the relative thermal sensitivity (S^{rel})^{22, 41}, defined as:

$$S^{\text{rel}} = \frac{S}{FIR} \quad (2.3)$$

where the FIR and S values have been previously defined in equations (2.1) and (2.2). The relative sensitivity, in the investigated temperature range, is estimated to be around $(0.120 \pm 0.05) \cdot 10^{-2} \text{ K}^{-1}$, and it shows small variations as a function of the temperature (see figure 2.5). The obtained relative sensitivities are very similar to those found for other nanothermometers based only on the Nd^{3+} emission, in colloidal dispersion form. Nonetheless, it is important to remark that the present nanothermometer can work using two well separated emission bands, that are located in the I-BW (the ${}^4F_{3/2} \rightarrow {}^4I_{9/2}$ transition) and in the II-BW (the ${}^4F_{3/2} \rightarrow {}^4I_{11/2}$ transition). To the best of our knowledge, this is the first time that these two NIR emission bands due to Nd^{3+} ions are exploited for nanothermometry in the biological windows. In fact, in the literature

only the investigation focusing on emissions within the same ${}^4F_{3/2} \rightarrow {}^4I_{9/2}$ or ${}^4F_{3/2} \rightarrow {}^4I_{11/2}$ band are found.

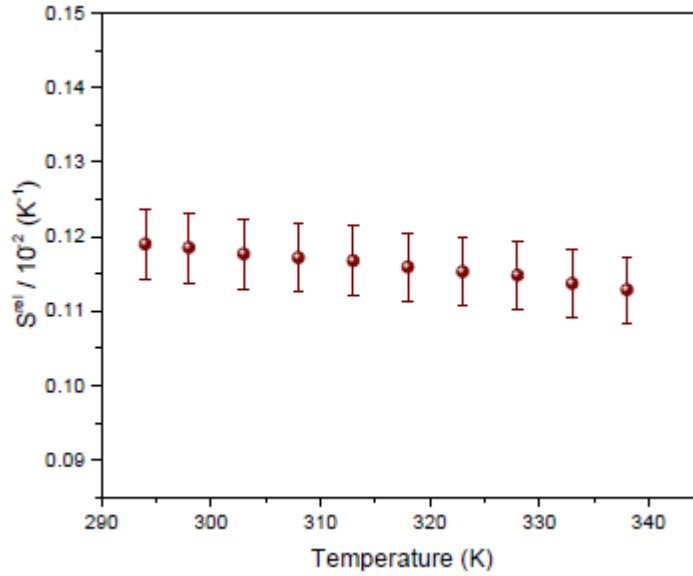


Figure 2.5 Thermal relative sensitivities for a water colloidal dispersion of $\text{CaF}_2:\text{Nd}^{3+}, \text{Gd}^{3+}$ NPs.

In table 2.1, the values for relative sensitivities of nanothermometers based only on the Nd^{3+} emission are reported for water dispersions. The ratiometric method in the I-BW and II-BW with the nanothermometers under investigation could be particularly advantageous for real applications in optical imaging. In fact, the two thermometric emission bands are well separated in energy and therefore the experimental setup could be based on inexpensive filters with relatively narrow optical spectral bandwidth instead of using expensive monochromatic systems.

Table 2.1

Comparison between Nd^{3+} activated NPs in water colloidal dispersions as nanothermometers.

Host	FIR ^a	Temperature range	$S^{rel} (\cdot 10^{-2} K^{-1})^b$	Reference
$\text{CaF}_2:\text{Nd}$	I_{1058}/I_{867}	21 – 65 °C	0.12	This work
$\text{LaF}_3:\text{Nd}$	I_{885}/I_{863}	30 – 60 °C	0.12	[39]
$\text{YVO}_4:\text{Nd}$	I_{879}/I_{887}	25 – 60 °C	0.19	[42]
$\text{YVO}_4:\text{Nd}$	I_{1063}/I_{1072}	25 – 60 °C	0.15	[42]
$\text{YAG}:\text{Nd}$	I_{938}/I_{945}	10 – 70 °C	0.15	[12]

^a I: intensity of the emission band.

^b Highest value in the considered temperature interval.

Another very important parameter used to describe the thermometric performance is the minimum temperature uncertainty ΔT^{min} , which defines the accuracy that can be achieved in the temperature evaluation under conditions in which the nanothermometers are working. This parameter is defined as⁴³:

$$\Delta T^{min} = \frac{\Delta FIR}{FIR \cdot S^{rel}} \quad (2.4)$$

It is important to remark that the $\Delta FIR/FIR$ ratio (relative uncertainty of the thermometric parameter) depends on the instrumental setup and in particular on the signal

to noise ratio of the obtained signal. The obtained ΔT^{\min} values are around 1.85 ± 0.10 °C (figure 2.6) in the investigated temperature range. It is worth mentioning that Yarmolenko et al. reviewed the thermal thresholds for thermal damage to normal tissues⁴⁴ and pointed out that temperature and time treatment have a crucial role in hyperthermia, both considered in the accepted metric for thermal dose assessment (Cumulative Equivalent Minutes at 43 °C, CEM43). Although the ΔT^{\min} value for the present NPs is not extremely low, it could be enough to monitor if the temperature reaches a threshold value in a hyperthermia treatment.

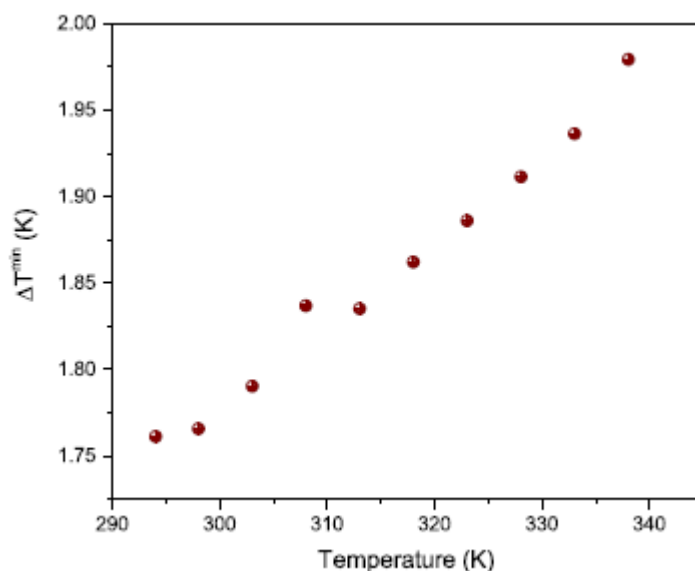


Figure 2.6 ΔT^{\min} as a function of the temperature for water colloidal dispersion of $\text{CaF}_2:\text{Nd}^{3+},\text{Gd}^{3+}$ NPs. The uncertainties in the ΔT^{\min} values are within the dot size.

Conclusions

In this investigation, Nd^{3+} , Gd^{3+} codoped CaF_2 NPs have been prepared with a simple hydrothermal method, using citrate ions as capping agents. The NPs can be easily and efficiently dispersed in water, forming a colloidal dispersion stable for months. From a spectroscopic investigation in the NIR region, it was observed that the CaF_2 NPs exhibit a good emission of the Nd^{3+} ions in the first and second BW, upon excitation at 573 nm. A thermometric investigation using a ratiometric technique involving two well separated NIR emission bands, evidenced that Nd^{3+} doped CaF_2 NPs as water colloids show a thermal relative sensitivity of $(0.12 \pm 0.05) \cdot 10^{-2} \text{ K}^{-1}$ almost invariant in the 21 - 65 °C temperature range, indicating their possible use as nanothermometers in biomedicine. The CaF_2 NPs present also a best temperature variation ΔT^{\min} around 1.8 °C, which could be enough to permit a significant temperature monitoring during a photothermal treatment.

REFERENCES

1. Dong, N. N.; Pedroni, M.; Piccinelli, F.; Conti, G.; Sbarbati, A.; Ramirez-Hernandez, J. E.; Maestro, L. M.; Iglesias-de la Cruz, M. C.; Sanz-Rodriguez, F.; Juarranz, A.; Chen, F.; Vetrone, F.; Capobianco, J. A.; Sole, J. G.; Bettinelli, M.; Jaque, D.; Speghini, A., NIR-to-NIR two-photon excited CaF₂:Tm³⁺,Yb³⁺ nanoparticles: multifunctional nanoprobes for highly penetrating fluorescence bio-imaging. *ACS nano* **2011**, *5* (11), 8665-71.
2. Jalani, G.; Naccache, R.; Rosenzweig, D. H.; Haglund, L.; Vetrone, F.; Cerruti, M., Photocleavable Hydrogel-Coated Upconverting Nanoparticles: A Multifunctional Theranostic Platform for NIR Imaging and On-Demand Macromolecular Delivery. *Journal of the American Chemical Society* **2016**, *138* (3), 1078-83.
3. Park, Y. I.; Kim, H. M.; Kim, J. H.; Moon, K. C.; Yoo, B.; Lee, K. T.; Lee, N.; Choi, Y.; Park, W.; Ling, D.; Na, K.; Moon, W. K.; Choi, S. H.; Park, H. S.; Yoon, S. Y.; Suh, Y. D.; Lee, S. H.; Hyeon, T., Theranostic probe based on lanthanide-doped nanoparticles for simultaneous in vivo dual-modal imaging and photodynamic therapy. *Advanced materials* **2012**, *24* (42), 5755-61.
4. Passuello, T.; Pedroni, M.; Piccinelli, F.; Polizzi, S.; Marzola, P.; Tambalo, S.; Conti, G.; Benati, D.; Vetrone, F.; Bettinelli, M.; Speghini, A., PEG-capped, lanthanide doped GdF₃ nanoparticles: luminescent and T₂ contrast agents for optical and MRI multimodal imaging. *Nanoscale* **2012**, *4* (24), 7682-9.
5. Carrasco, E.; del Rosal, B.; Sanz-Rodriguez, F.; de la Fuente, A. J.; Gonzalez, P. H.; Rocha, U.; Kumar, K. U.; Jacinto, C.; Sole, J. G.; Jaque, D., Intratumoral Thermal Reading During Photo-Thermal Therapy by Multifunctional Fluorescent Nanoparticles. *Advanced Functional Materials* **2015**, *25* (4), 615-626.
6. Rocha, U.; Kumar, K. U.; Jacinto, C.; Ramiro, J.; Caamano, A. J.; Sole, J. G.; Jaque, D., Nd³⁺ doped LaF₃ nanoparticles as self-monitored photo-thermal agents. *Appl Phys Lett* **2014**, *104* (5).
7. Ximendes, E. C.; Rocha, U.; Jacinto, C.; Kumar, K. U.; Bravo, D.; Lopez, F. J.; Martin Rodriguez, E.; Garcia-Sole, J.; Jaque, D., Self-monitored photothermal nanoparticles based on core-shell engineering. *Nanoscale* **2016**, *8* (5), 3057-66.
8. Ximendes, E. C.; Rocha, U.; Kumar, K. U.; Jacinto, C.; Jaque, D., LaF₃ core/shell nanoparticles for subcutaneous heating and thermal sensing in the second biological-window. *Appl Phys Lett* **2016**, *108* (25), 253103.
9. Dewhirst, M. W.; Viglianti, B. L.; Lora-Michiels, M.; Hoopes, P. J.; Hanson, M., Thermal Dose Requirement for Tissue Effect: Experimental and Clinical Findings. *Proceedings of SPIE--the International Society for Optical Engineering* **2003**, *4954*, 37.
10. Jaque, D.; Vetrone, F., Luminescence nanothermometry. *Nanoscale* **2012**, *4* (15), 4301-26.
11. Jaque, D.; Rosal, B. D.; Rodriguez, E. M.; Maestro, L. M.; Haro-Gonzalez, P.; Sole, J. G., Fluorescent nanothermometers for intracellular thermal sensing. *Nanomedicine* **2014**, *9* (7), 1047-62.
12. Benayas, A.; del Rosal, B.; Pérez-Delgado, A.; Santacruz-Gómez, K.; Jaque, D.; Hirata, G. A.; Vetrone, F., Nd:YAG Near-Infrared Luminescent Nanothermometers. *Advanced Optical Materials* **2015**, *3* (5), 687-694.
13. Marciniak, L.; Prorok, K.; Frances-Soriano, L.; Perez-Prieto, J.; Bednarkiewicz, A., A broadening temperature sensitivity range with a core-shell YbEr@YbNd double ratiometric optical nanothermometer. *Nanoscale* **2016**, *8* (9), 5037-42.

14. Vetrone, F.; Naccache, R.; Zamarron, A.; Juarranz de la Fuente, A.; Sanz-Rodriguez, F.; Martinez Maestro, L.; Martin Rodriguez, E.; Jaque, D.; Garcia Sole, J.; Capobianco, J. A., Temperature sensing using fluorescent nanothermometers. *ACS nano* **2010**, *4* (6), 3254-8.
15. Ximendes, E. C.; Santos, W. Q.; Rocha, U.; Kagola, U. K.; Sanz-Rodriguez, F.; Fernandez, N.; Gouveia-Neto Ada, S.; Bravo, D.; Domingo, A. M.; Del Rosal, B.; Brites, C. D.; Carlos, L. D.; Jaque, D.; Jacinto, C., Unveiling in Vivo Subcutaneous Thermal Dynamics by Infrared Luminescent Nanothermometers. *Nano letters* **2016**, *16* (3), 1695-703.
16. del Rosal, B.; Ximendes, E.; Rocha, U.; Jaque, D., In Vivo Luminescence Nanothermometry: from Materials to Applications. *Advanced Optical Materials* **2016**, n/a-n/a.
17. Kilbane, J. D.; Chan, E. M.; Monachon, C.; Borys, N. J.; Levy, E. S.; Pickel, A. D.; Urban, J. J.; Schuck, P. J.; Dames, C., Far-field optical nanothermometry using individual sub-50 nm upconverting nanoparticles. *Nanoscale* **2016**, *8* (22), 11611-11616.
18. Savchuk, O. A.; Carvajal, J. J.; Cascales, C.; Massons, J.; Aguilo, M.; Diaz, F., Thermochromic upconversion nanoparticles for visual temperature sensors with high thermal, spatial and temporal resolution. *Journal of Materials Chemistry C* **2016**, *4* (27), 6602-6613.
19. Zhou, S.; Jiang, G.; Li, X.; Jiang, S.; Wei, X.; Chen, Y.; Yin, M.; Duan, C., Strategy for thermometry via Tm(3)(+)-doped NaYF(4) core-shell nanoparticles. *Optics letters* **2014**, *39* (23), 6687-90.
20. Smith, A. M.; Mancini, M. C.; Nie, S., Bioimaging: second window for in vivo imaging. *Nature nanotechnology* **2009**, *4* (11), 710-1.
21. Weissleder, R., A clearer vision for in vivo imaging. *Nature biotechnology* **2001**, *19* (4), 316-7.
22. Balabhadra, S.; Debasu, M. L.; Brites, C. D. S.; Nunes, L. A. O.; Malta, O. L.; Rocha, J.; Bettinelli, M.; Carlos, L. D., Boosting the sensitivity of Nd³⁺-based luminescent nanothermometers. *Nanoscale* **2015**, *7* (41), 17261-17267.
23. Cheng, L.; Wang, C.; Liu, Z., Upconversion nanoparticles and their composite nanostructures for biomedical imaging and cancer therapy. *Nanoscale* **2013**, *5* (1), 23-37.
24. Huang, S.; Gu, L.; Miao, C.; Lou, Z.; Zhu, N.; Yuan, H.; Shan, A., Near-infrared photocatalyst of Er³⁺/Yb³⁺ codoped (CaF₂@TiO₂) nanoparticles with active-core/active-shell structure. *Journal of Materials Chemistry A* **2013**, *1* (27), 7874.
25. Pedroni, M.; Piccinelli, F.; Passuello, T.; Giarola, M.; Mariotto, G.; Polizzi, S.; Bettinelli, M.; Speghini, A., Lanthanide doped upconverting colloidal CaF₂ nanoparticles prepared by a single-step hydrothermal method: toward efficient materials with near infrared-to-near infrared upconversion emission. *Nanoscale* **2011**, *3* (4), 1456-60.
26. Pedroni, M.; Piccinelli, F.; Passuello, T.; Polizzi, S.; Ueda, J.; Haro-Gonzalez, P.; Maestro, L. M.; Jaque, D.; Garcia-Sole, J.; Bettinelli, M.; Speghini, A., Water (H₂O and D₂O) Dispersible NIR-to-NIR Upconverting Yb³⁺/Tm³⁺ Doped MF₂ (M = Ca, Sr) Colloids: Influence of the Host Crystal. *Crystal Growth & Design* **2013**, *13* (11), 4906-4913.
27. Cantarelli, I. X.; Pedroni, M.; Piccinelli, F.; Marzola, P.; Boschi, F.; Conti, G.; Sbarbati, A.; Bernardi, P.; Mosconi, E.; Perbellini, L.; Marongiu, L.; Donini, M.; Dusi, S.; Sorace, L.; Innocenti, C.; Fantechi, E.; Sangregorio, C.; Speghini, A., Multifunctional nanoprobos based on upconverting lanthanide doped CaF₂:

- towards biocompatible materials for biomedical imaging. *Biomaterials Science* **2014**, 2 (9), 1158.
28. Portioli, C.; Pedroni, M.; Benati, D.; Donini, M.; Bonafede, R.; Mariotti, R.; Perbellini, L.; Cerpelloni, M.; Dusi, S.; Speghini, A.; Bentivoglio, M., Citrate-stabilized lanthanide-doped nanoparticles: brain penetration and interaction with immune cells and neurons. *Nanomedicine* **2016**, 11 (23), 3039-3051.
 29. Ravangave, L. S., Effect of doping concentration of Eu³⁺ ion on CaF₂ nanoparticles. *Digest Journal of Nanomaterials and Biostructures* **2010**, 5 (3), 575-578.
 30. Wang, F.; Han, Y.; Lim, C. S.; Lu, Y.; Wang, J.; Xu, J.; Chen, H.; Zhang, C.; Hong, M.; Liu, X., Simultaneous phase and size control of upconversion nanocrystals through lanthanide doping. *Nature* **2010**, 463 (7284), 1061-1065.
 31. Mondini, S.; Ferretti, A. M.; Puglisi, A.; Ponti, A., Pebbles and PebbleJuggler: software for accurate, unbiased, and fast measurement and analysis of nanoparticle morphology from transmission electron microscopy (TEM) micrographs. *Nanoscale* **2012**, 4 (17), 5356-72.
 32. Gerward, L.; Olsen, J. S.; Steenstrup, S.; Malinowski, M.; Åsbrink, S.; Waskowska, A., X-ray diffraction investigations of CaF₂ at high pressure. *Journal of Applied Crystallography* **1992**, 25 (5), 578-581.
 33. Shannon, R. D.; Prewitt, C. T., Revised values of effective ionic radii. *Acta Cryst. B* **1970**, 26 (7), 1046-1048.
 34. Ma, F. K.; Zhang, Q.; Jiang, D. P.; Su, L. B.; Shao, Y. J.; Wang, J. Y.; Tang, F.; Xu, J.; Solarz, P.; Ryba-Romanowski, W.; Lisiecki, R.; Macalik, B., Spectroscopic, dielectric properties and local structure observation by EXAFS for Nd,Y:CaF₂ crystal. *Laser Physics* **2014**, 24 (10), 105703.
 35. Hraiech, S.; Jouini, A.; Jin Kim, K.; Guyot, Y.; Yoshikawa, A.; Boulon, G., Role of monovalent alkali ions in the Yb³⁺ centers of CaF₂ laser crystals. *Radiation Measurements* **2010**, 45 (3-6), 323-327.
 36. Leśniak, K., Crystal fields and local lattice distortions in some tetragonal symmetry centers in fluorite crystals doped with trivalent rare-earth ions. *The Journal of Chemical Physics* **1991**, 94 (5), 3919-3927.
 37. Petit, V.; Camy, P.; Doualan, J. L.; Portier, X.; Moncorgé, R., Spectroscopy of Yb³⁺:CaF₂: From isolated centers to clusters. *Physical Review B* **2008**, 78 (8).
 38. Wells, J.-P. R.; Reeves, R. J., Polarized laser selective excitation and Zeeman infrared absorption of $\{C\}_{4v}$ and $\{C\}_{3v}$ symmetry centers in $\{\mathrm{Eu}\}^{3+}$ -doped $\{\mathrm{CaF}\}_2$, $\{\mathrm{SrF}\}_2$, and $\{\mathrm{BaF}\}_2$ crystals. *Physical Review B* **2001**, 64 (3), 035102.
 39. Rocha, U.; Jacinto, C.; Silva, W. F.; Guedes, I.; Benayas, A.; Maestro, L. M.; Elias, M. A.; Bovero, E.; van Veggel, F. C. J. M.; Sole, J. A. G.; Jaque, D., Subtissue Thermal Sensing Based on Neodymium-Doped LaF₃ Nanoparticles. *ACS nano* **2013**, 7 (2), 1188-1199.
 40. Ceron, E. N.; Ortgies, D. H.; del Rosal, B.; Ren, F.; Benayas, A.; Vetrone, F.; Ma, D.; Sanz-Rodriguez, F.; Sole, J. G.; Jaque, D.; Rodriguez, E. M., Hybrid Nanostructures for High-Sensitivity Luminescence Nanothermometry in the Second Biological Window. *Advanced materials* **2015**, 27 (32), 4781-4787.
 41. Wade, S. A.; Collins, S. F.; Baxter, G. W., Fluorescence intensity ratio technique for optical fiber point temperature sensing. *J Appl Phys* **2003**, 94 (8), 4743-4756.
 42. Kolesnikov, I. E.; Golyeva, E. V.; Kurochkin, M. A.; Lähderanta, E.; Mikhailov, M. D., Nd³⁺-doped YVO₄ nanoparticles for luminescence nanothermometry in the first

- and second biological windows. *Sensors and Actuators B: Chemical* **2016**, 235, 287-293.
43. Wang, Z. P.; Ananias, D.; Carne-Sanchez, A.; Brites, C. D. S.; Imaz, I.; Maspoch, D.; Rocha, J.; Carlos, L. D., Lanthanide-Organic Framework Nanothermometers Prepared by Spray-Drying. *Advanced Functional Materials* **2015**, 25 (19), 2824-2830.
 44. Yarmolenko, P. S.; Moon, E. J.; Landon, C.; Manzoor, A.; Hochman, D. W.; Viglianti, B. L.; Dewhirst, M. W., Thresholds for thermal damage to normal tissues: An update. *International Journal of Hyperthermia* **2011**, 27 (4), 320-343.

Chapter 3

Core@Multishell Architectures for Multicolor Upconversion and Near-Infrared Nanothermometry

3.1 Introduction

Luminescent nanoprobes in the optical range (ultraviolet, visible and near-infrared (NIR) regions) are gaining much importance in biomedicine, in particular as materials for diagnostics and optical *in-vitro* and *in-vivo* imaging¹⁻³. Much effort has been devoted in the last years to engineer various functional nanomaterials, showing different features, and to integrate them in a unique nanostructure with improved multimodal capabilities^{4,5}. Lanthanide (Ln) doped upconverting nanoparticles (UCNPs) are excellent materials for optical nanoprobes⁶. Moreover, Ln-doped nanoparticles (NPs) have been recently investigated especially for *in-vivo* optical imaging, due to their emissions in the so-called biological optical transparency windows⁷. In fact, the NIR optical radiation penetrates deeper into the biological tissues, as it is less absorbed and also less scattered with respect to the visible light by the biological tissue constituents⁸⁻¹⁰. Many Ln-doped UCNPs can harvest light at a wavelength of 980 nm by means of the Yb³⁺ ion acting as the sensitizer¹¹. Exciting at this wavelength to generate emission, could be feasible for *in-vitro* diagnostics but much less for *in-vivo* applications, where due to significant absorption of water at 980 nm undesirable local heating can occur. To overcome this drawback, the Nd³⁺ ion has been investigated recently, as possible sensitizer for *in-vivo* imaging. Nd³⁺ activated NPs can convert NIR excitation light around 800 nm in the first biological optical transparency window (I-BW, 750-950 nm optical range) to visible light (upconversion; UC) as well as to Stokes NIR emission in the second biological optical transparency window (II-BW, 1000-1400 nm optical range)¹²⁻¹³. Most importantly, water absorption of 800 nm radiation is low, in turn the optical heating is greatly minimized¹⁴.

Possible strategies to enhance the luminescence properties of Ln-doped NPs involve the design of core@shell (C@S) architectures for nanostructured systems¹⁵⁻¹⁷. The enhancement effect is achieved by reducing surface based non-radiative processes, such as multiphonon relaxation, due to the interaction of the solvent molecules (water, in the case of nanomedical applications) with the superficial Ln ions. The C@S structure also allows for the promotion and/or reduction of specific energy transfer (ET) processes among Ln ions by choosing a proper shell composition¹⁸⁻¹⁹. Thus, appropriate design of C@S NPs permits to obtain desired luminescence features, that can be useful to trigger other systems for photodynamic therapy²⁰.

In modern medicine, real-time temperature sensing is of paramount importance, as a diagnostic tool for diseases that induce local temperature enhancements in the biological tissues, or for temperature monitoring during photothermal tumor treatment, to prevent excessive heating and therefore healthy tissue damage. Subsequently, a de-

sirable feature for multifunctional luminescent nanoprobe is the capability of measuring the temperature by monitoring optical spectral changes²¹⁻²². These systems can play an important role in nanomedicine²³⁻²⁵, since their nanosized nature permits to evaluate the local temperature with a high spatial resolution, within a single cell or even at a subcellular level²⁶⁻²⁷. Ln-based nanostructured materials are particularly adept as thermal probes, due to the unique arrangement of their energy levels resulting in multiple temperature sensitive luminescence bands²⁸. Many luminescent nanothermometers (NTHs) are based on ratiometric temperature sensing, which involves taking the ratio between the integrated signals of two well-defined emission bands²⁹⁻³¹. For good thermal sensitivity, this ratio should vary as much as possible with changes in temperature. Importantly, the ratiometric procedure avoids the calibration of the optical thermometer as in the case of changes of single band emission, since this is strongly dependent on the local probe concentration³². The majority of Ln-based NTHs have exploited their visible emissions for temperature sensing, mainly upon excitation in the NIR region at 980 nm³³⁻³⁵. Recently some interesting studies have appeared describing the utility of the Nd³⁺ ion, as dopant in some fluoride hosts³⁶⁻³⁹, not only for radiation harvesting but also for luminescence nanothermometry. In particular, Nd³⁺ doped LaF₃^{8,40-41} and NaYF₄⁴² NPs have been investigated as NIR temperature sensors, using 800 nm as the excitation wavelength, in the I-BW. Moreover, thanks to the notable absorption of the Nd³⁺ ions around 800 nm, it is also possible to exploit Nd³⁺ doped nanomaterials not only as optical thermometers but also to produce heat with high spatial resolution, as nanoheaters⁴¹.

While most studies have focused on NaYF₄, NaGdF₄ or LaF₃ hosts, alkaline-earth based fluorides (such as CaF₂ and SrF₂) have recently demonstrated to be very versatile and efficient hosts for Ln doping⁴³⁻⁴⁴. In particular, SrF₂ based NPs, that have low phonon energies, show strong UC properties and temperature sensitive emissions in the UV, visible, and NIR regions, as well as strong luminescence in the NIR for bioimaging⁴⁵⁻⁴⁹. These fluoride hosts are also easily prepared with facile and “green chemistry”, environmental friendly methods, using water as a solvent and low temperatures (< 200 °C) conditions.

The aim of the present investigation was to develop new multifunctional core@multishell Ln-doped SrF₂ NPs, properly designed as visible-NIR optical probes and NTHs. By choosing the Nd³⁺, Yb³⁺, Er³⁺ and Tm³⁺ as dopant ions, the present multishell nanoparticles (MNPs) were rationally designed to harvest 800 nm and also 980 nm radiation, subsequently emit visible UC and NIR (in the II-BW) light, that can be exploited for all-optical nanothermometry in both spectral regions.

3.2 Experimental Section

Preparation and MNPs architectures

MNPs were synthesized in four subsequent hydrothermal reaction steps^{45, 50}. At each synthetic step, solid strontium and Ln chlorides in the desired stoichiometric ratio were dissolved in 20 mL of deionized water (final metal concentration 0.2 M) adding potassium citrate as the capping agent (1 M, final concentration). The solution was stirred until all the reagents dissolved and an aqueous solution of NH₄F was added in order to have a F:(Ln³⁺+Sr²⁺) ratio of 2.5. All the reagents (99.9% purity) were purchased from Sigma-Aldrich, and were used without further purification. The resulting solution was sealed in a steel autoclave and heated at 190 °C for 3 h.⁴⁷ The NPs were then precipitated with acetone or ethanol and collected by centrifugation. The resulting

gel could be stored under acetone without any degradation and the NPs form transparent colloidal suspensions when dissolved in water. For the shell synthesis, the previously synthesized core (or core@shell) NPs were added to the reagents solution, as seeds to start the growth of the shell and the synthesis is performed as previously described. The dopant concentration and the architectures of the MNPs are described as follows, taking into account that the Ln percentages are referred to the total metal content in the corresponding core or shell layer:

- **MNPs1:**
 $\text{SrF}_2:\text{Yb}(22\%),\text{Tm}(0.2\%)\text{@Y}(22\%)\text{@Yb}(19\%),\text{Er}(2\%),\text{Nd}(1\%)\text{@Nd}(22\%)$.
- **MNPs2:**
 $\text{SrF}_2:\text{Yb}(22\%),\text{Er}(2\%)\text{@Y}(22\%)\text{@Yb}(19\%),\text{Tm}(0.2\%),\text{Nd}(1%)\text{@Nd}(22\%)$.
- **MNPs3:**
 $\text{SrF}_2:\text{Yb}(22\%),\text{Tm}(0.2\%)\text{@Y}(22\%)\text{@Yb}(19\%),\text{Nd}(1%)\text{@Nd}(22\%)$.

The architecture of the MNPs are schematically shown in figure 3.1.

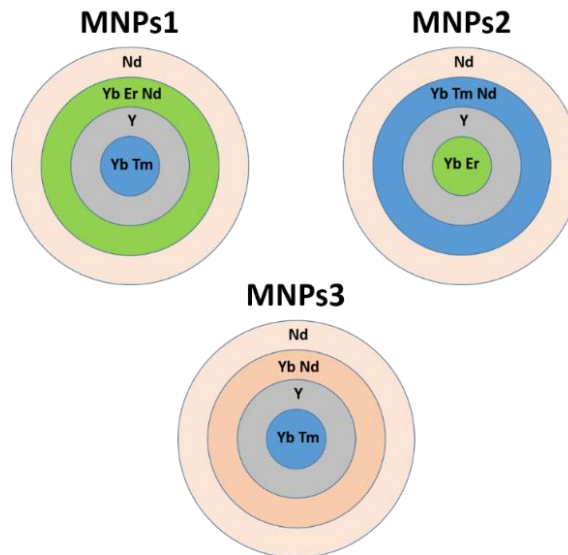


Figure 3.1 Schematic representations of the MNPs.

Note that MNPs1 and MNPs2 were designed with the same architecture and dopants but the Tm^{3+} and Er^{3+} ions are in the core and 2nd shell respectively for the MNPs1 while they are inverted for the MNPs2 (see figure 3.1). To investigate the influence of Er^{3+} and Tm^{3+} ions on the NIR emissions of Nd^{3+} and Yb^{3+} ions in the different MNPs, a reference system was designed (MNPs3) whose structure was similar to that of MNPs1 but with no Er^{3+} ions in the 2nd shell. It is worth noting that in all cases the percentages of the dopant ions were kept identical for corresponding core and shells. Furthermore, the 1st shell is doped only with the spectroscopically silent Y^{3+} ions, in order to minimize ET processes among Ln ions in the core and the 2nd shell. The 3rd shell contains only Nd^{3+} ions in elevated concentration (22%) for efficient harvest of radiation at 800 nm. The core@multi-shell structure has been inspired by Lai et al. work⁵¹.

Structural Analysis

X-ray powder diffraction (XRPD) patterns were measured using a Thermo ARL X'TRA powder diffractometer, equipped with a Cu anode X-ray source. The cell parameter for cubic structures was determined from the XRPD reflections. The crystallite size for the core and core@multishell structures were also estimated from the XRPD reflections using the Debye-Scherrer formula.

Morphology

Transmission Electron Microscopy (TEM) images were obtained with a CM200 LaB₆ Philips microscope operating at 200 kV. A few drops of NP dispersions were deposited on a copper grid and dried in air. Pebbles software was used to analyze the NP size distribution.⁵²

DLS analysis

Dynamic Light Scattering (DLS) measurements were carried out using a Malvern Zetasizer Nano ZS90, operating with a He-Ne laser at 633 nm. The samples were prepared in water colloidal dispersions with a 10 mg/mL concentration, using plastic disposable cuvettes. Malvern Zetasizer Software was used to obtain the hydrodynamic radius of the MNPs.

Luminescence spectroscopy and thermometric measurements

MNPs emission was measured using an Avaspec-ULS2048L spectrometer (Avantes) for the visible spectral range and with a Shamrock 500i monochromator (Andor) equipped with an iDus InGaAs 1.7 NIR detector (Andor).

For thermometry measurements, 980 nm and 806 nm continuous wave (cw) fiber-coupled laser diodes (Thorlabs) were used as the excitation sources. Their laser power densities were 240 W/cm² or 31 W/cm² for 980 or 800 nm excitation wavelength, respectively. A temperature control stage (Quantum Northwest qpod2e) was used. All the spectroscopic measurements were performed on water colloidal dispersion of MNPs (1 %wt).

3.3 Results and Discussion

Structural and Morphological Analysis

XRPD measurements were carried out on the MNPs after each reaction step, in order to check the growth of the core and each subsequent shell (shown respectively, in figures 3.2 and 3.3).

All the NPs presented a cubic single phase (space group n. 225, $Fm\bar{3}m$), with a cell parameter of 5.74 ± 0.01 Å. It can be noted that the reflections become sharper after addition of each shell suggesting a linear increase of the crystallite size with the increasing number of shells. TEM images of MNPs1 and MNPs2 after each synthesis step are shown in figure 3.4, together with the statistical size distribution calculations. The average size of the MNPs increased after each synthesis step, confirming the growth of multiple shells. The overall growth between the MNPs1 and MNPs2 was similar, as the mean size of the core of MNPs1 was 8.4 nm and of MNPs2 was 7.9 nm, while the average size of the complete structures was 24.1 and 26.3 nm for MNPs1 and MNPs2, respectively. The standard deviation of each size distribution was determined to be always <20% of the mean value, indicating small size dispersion (see figure 3.4). DLS measurements, shown in figure 3.5, additionally confirmed the multishell architecture of the MNPs, as an increase of the MNPs hydrodynamic size was observed after each synthesis step.

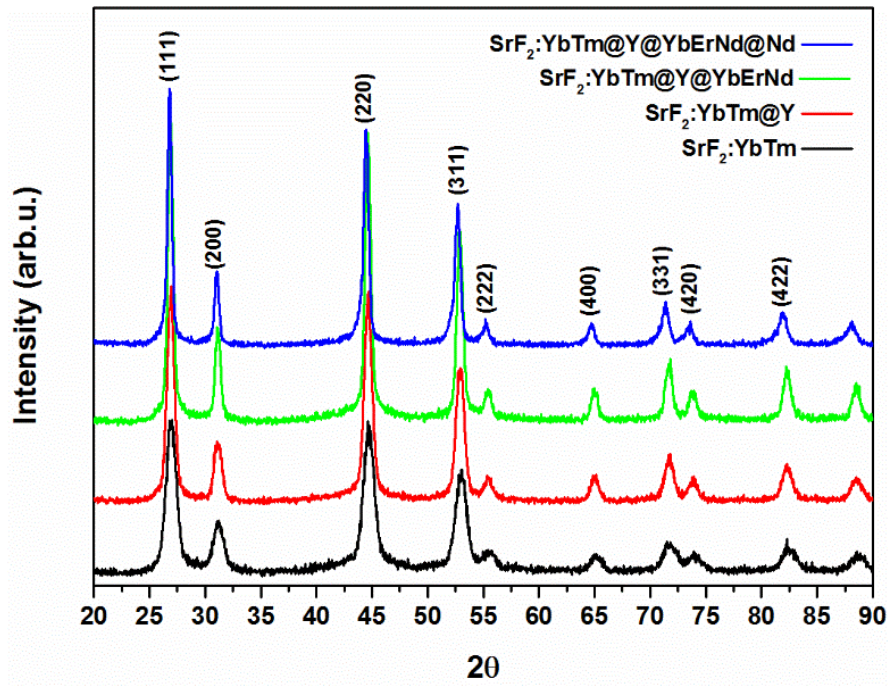


Figure 3.2 XRPD patterns for MNPs1 after each shell growth step.

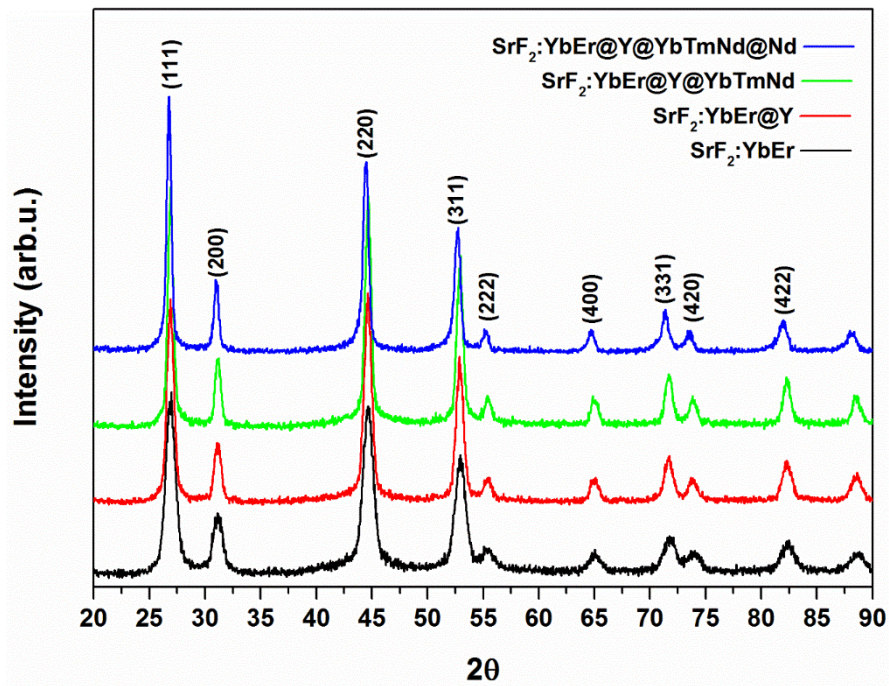


Figure 3.3 XRPD patterns for the MNPs2 after each shell growth step.

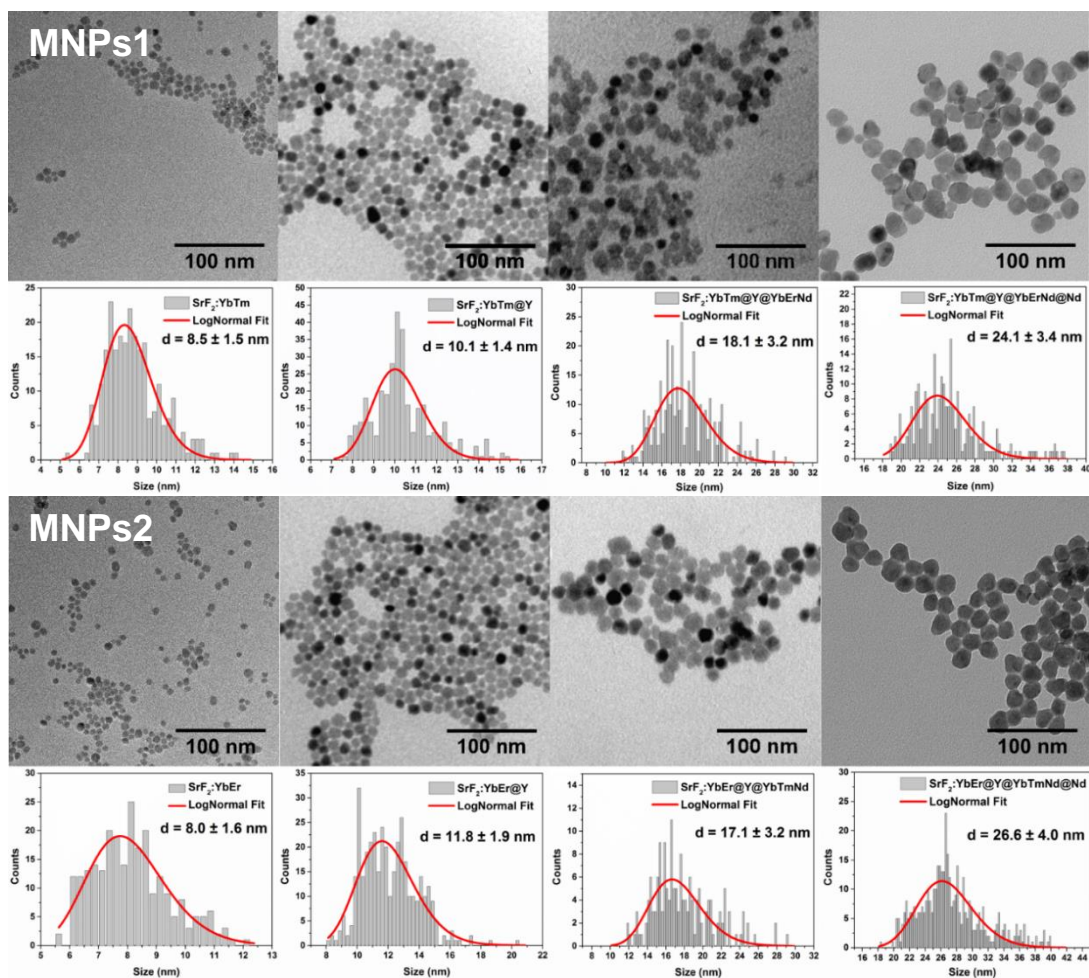


Figure 3.4 TEM images of the MNPs1 and MNPs2 after each reaction step and respective size distribution analysis, from the core (on the left) to the complete core@multishell MNPs (on the right).

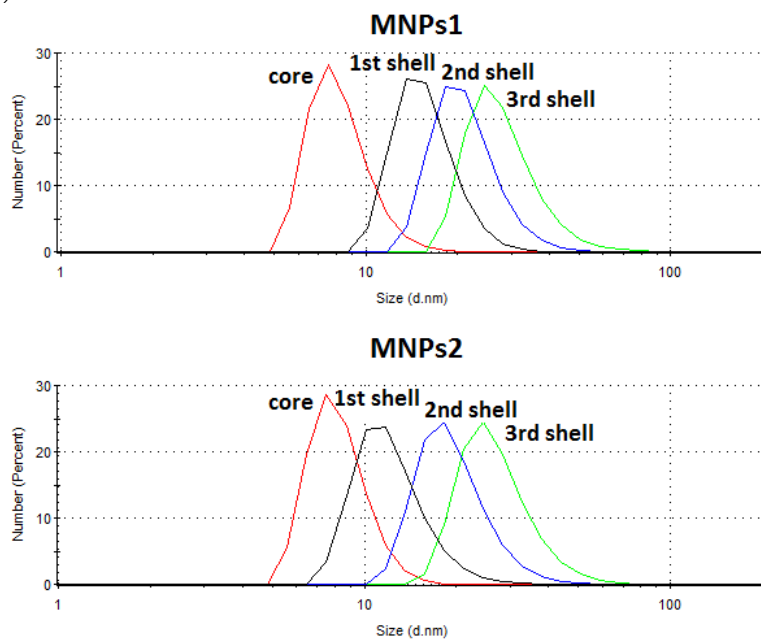


Figure 3.5 Hydrodynamic size measured by DLS technique for MNPs1 and MNPs2.

The summary of the sizes obtained from TEM, XRD and DLS studies for each synthesis step of MNPs1 and MNPs2 are shown in table 3.1. MNPs3 is not shown, but it presents the same structural and morphological features of MNPs1 and MNPs2.

Table 3.1 MNPs1 and MNPs2 size (in nm) at each synthesis step obtained from TEM, XRD and DLS data.

MNPs1	core	c@s	c@s@s	c@s@s@s
TEM	8.5 ± 1.5	10.1 ± 1.4	18.1 ± 3.2	24.1 ± 3.4
XRD	7.2 ± 0.2	10.0 ± 0.2	13.7 ± 0.3	16.4 ± 0.6
DLS	7.6 ± 2.0	15.1 ± 4.0	24.0 ± 3.9	28.4 ± 8.1
MNPs2	core	c@s	c@s@s	c@s@s@s
TEM	8.0 ± 1.6	11.8 ± 1.9	17.1 ± 3.2	26.6 ± 4.0
XRD	7.5 ± 0.2	10.6 ± 0.3	13.3 ± 0.4	15.5 ± 0.8
DLS	8.7 ± 2.0	17.3 ± 3.6	22.1 ± 3.2	27.2 ± 8.0

Spectroscopic Investigations

Upconversion emission upon 980 nm excitation. The UC spectra for water colloidal MNPs1 and MNPs2 dispersions (1 %wt) upon 980 nm laser excitations are shown in figure 3.6. The spectra present different features for the two kinds of MNPs. In particular, MNPs1 (with Tm³⁺ ions in the core) show strong Tm³⁺ emissions in the visible and NIR ranges,⁵³⁻⁵⁴ with negligible Er³⁺ emission at 550 nm. On the other hand, MNPs2 (with Er³⁺ in the core) present mainly Er³⁺ specific emissions⁵⁵⁻⁵⁶, with some Tm³⁺ UC bands in the UV (350-375 nm), blue (450-500 nm) and NIR (750-800 nm) regions^{48, 57}. This behavior could be explained by the fact that Tm³⁺ and Yb³⁺ ions are buried in the core of MNPs1, while the Er³⁺ ions are in the 2nd shell, together with the Yb³⁺ and Nd³⁺. Therefore, the extremely weak Er³⁺ luminescence could be attributed to an efficient Er³⁺ → Nd³⁺ ET, additionally boosted by the high concentration of Nd³⁺ ions present in the 3rd shell. Similarly, the main UC emission for MNPs2 derives from the Er³⁺ ions, located in the core, and are efficiently separated from the Nd³⁺ containing 2nd and 3rd shells by the 1st shell. In both MNPs1 and MNPs2, it is therefore reasonable that, due to close proximity of Er³⁺ or Tm³⁺ ions to Nd³⁺ ones, Er³⁺ → Nd³⁺ or Tm³⁺ → Nd³⁺ ET processes lead to UC quenching.⁵⁸⁻⁶⁰

The suggested mechanisms for the Nd³⁺ related UC emission quenching for the two MNPs are shown in figures 3.7 and 3.8. Since the Er³⁺ UC for MNPs1 is almost completely quenched (figure 3.6a) while the Tm³⁺ one for MNPs2 is still observable (figure 3.6b), the Er³⁺ → Nd³⁺ ET process is presumably more efficient than the Tm³⁺ → Nd³⁺ one. One possible explanation for this behavior involves the difference in the Ln ions concentration between Er³⁺ in the 2nd shell of MNPs1 (2.0 %) and Tm³⁺ ions in the 2nd shell of MNPs2 (0.2 %).

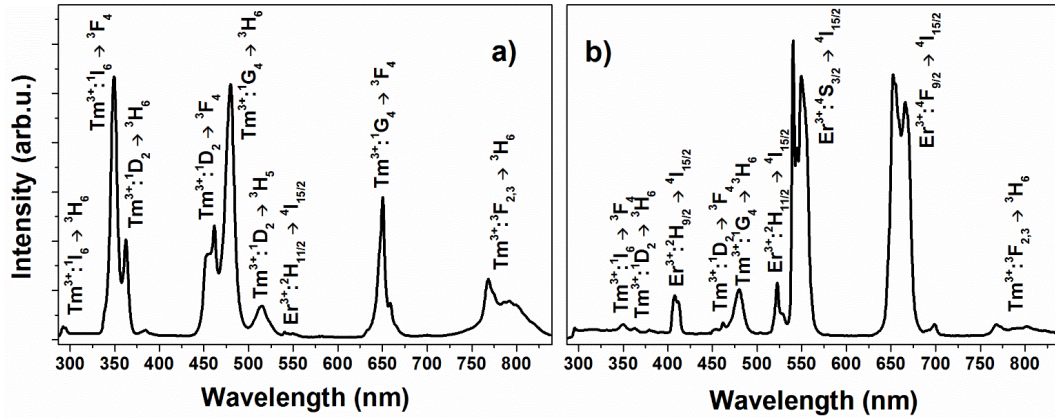


Figure 3.6 Upconversion spectra of MNPs1 (a) and MNPs2 (b) upon 980 nm excitation.

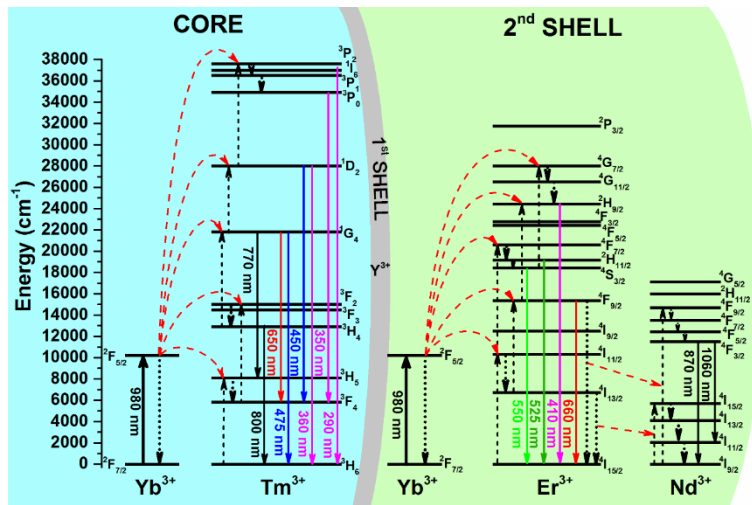


Figure 3.7 ETU mechanisms for MNPs1 upon 980 nm excitation. Black, ascending solid arrows represent 980 nm laser excitation. Dotted descending black arrows represent non-radiative de-excitation. Descending solid arrows represent the emissions. Ascending dashed arrows represents energy absorptions. Red dashed arrows represent Energy Transfers processes.

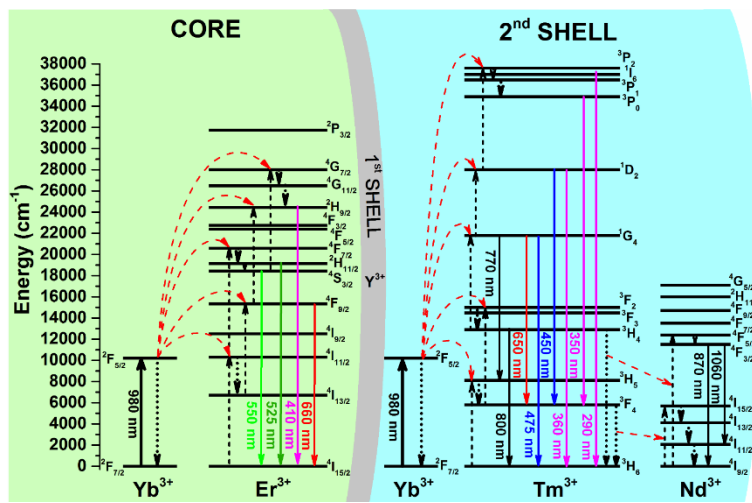
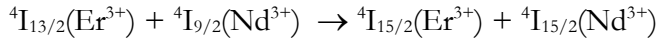
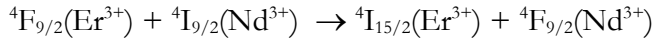


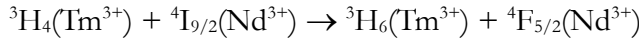
Figure 3.8 ETU mechanisms for MNPs2 upon 980 nm excitation. Black, ascending solid arrows represent 980 nm laser excitation. Dotted descending black arrows represent non-radiative de-excitation. Descending solid arrows represent the emissions. Ascending dashed arrows represents energy absorptions. Red dashed arrows represent Energy Transfers processes.

diative de-excitation. Descending solid arrows represent the emissions. Ascending dashed arrows represents energy absorptions. Red dashed arrows represent Energy Transfers processes.

In fact, for the present Ln concentrations, there is a lower average donor-acceptor distance between the Er^{3+} and Nd^{3+} ions in the MNPs1 than for the distance among Tm^{3+} and Nd^{3+} ones in MNPs2, therefore promoting the $\text{Er}^{3+} \rightarrow \text{Nd}^{3+}$ ET than the $\text{Tm}^{3+} \rightarrow \text{Nd}^{3+}$ one. On the other hand, a better overlap among the energy levels of the donor and the acceptor ions could also facilitate the ET process. For MNPs1, at least two possible $\text{Er}^{3+} \rightarrow \text{Nd}^{3+}$ ET processes (figure 3.7) can occur, as suggested by some groups⁶¹⁻⁶³



Therefore, this leads to significant depopulation of the ${}^4\text{F}_{9/2}$ and ${}^4\text{I}_{13/2}$ energy levels of Er^{3+} and subsequent UC emission intensity decrease.⁶⁴ In the case of MNPs2, one main $\text{Tm}^{3+} \rightarrow \text{Nd}^{3+}$ ET process is considered to be active (figure 3.8):



as described by Peng et al.⁶⁵, da Silva et al.⁶⁶ and Chung et al.⁶⁷

Most importantly, these results clearly demonstrate that the 1st shell (doped with Y^{3+}) screens efficiently the dopants in the core of MNPs from the possible ET processes with the Ln ions in the 2nd and 3rd shells. In turn, this spatial segregation of distinct functional layers within the MNPs allows for the controlled differentiation of the excitation and emission mechanisms taking place in the core and in the two outer shells.

Upconversion emission upon 806 nm excitation. When excited at the 806 nm wavelength (figure 3.9), the spectra of MNPs1 and MNPs2 strongly differ in the relative intensities between Tm^{3+} and Er^{3+} ion emissions with respect to previous observation upon 980 nm excitation. Moreover, the overall UC emission for the MNPs2 is around one order of magnitude greater than for the MNPs1.

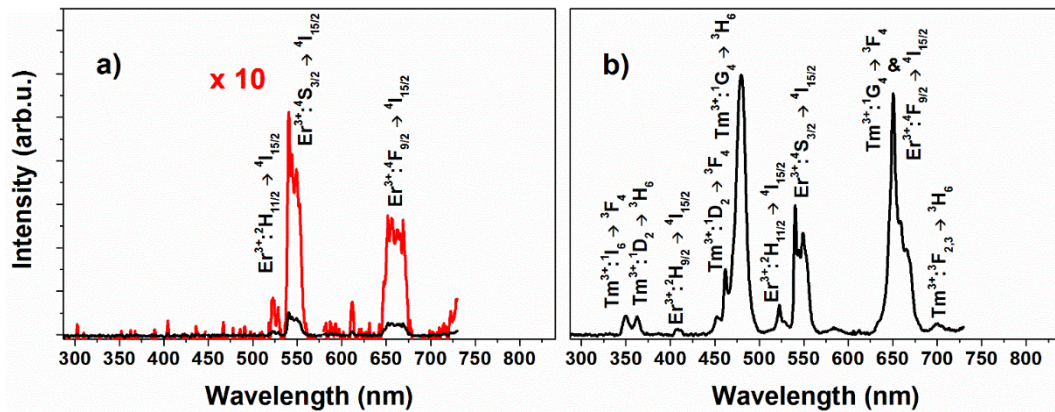


Figure 3.9 Upconversion spectra of MNPs1 (a) and MNPs2 (b) upon 806 nm excitation. UC emission spectrum of MNPs1 is additionally shown as multiplied by a factor of 10.

In the case of MNPs1, at the excitation laser power around 31 W/cm^2 , Tm^{3+} emission is not observed, but only weak Er^{3+} ions UC signal (figure 3.9a). Differently, at exactly the same experimental conditions and NPs concentration, both Tm^{3+} and Er^{3+} emissions are clearly observable in the case of MNPs2 (figure 3.9b).

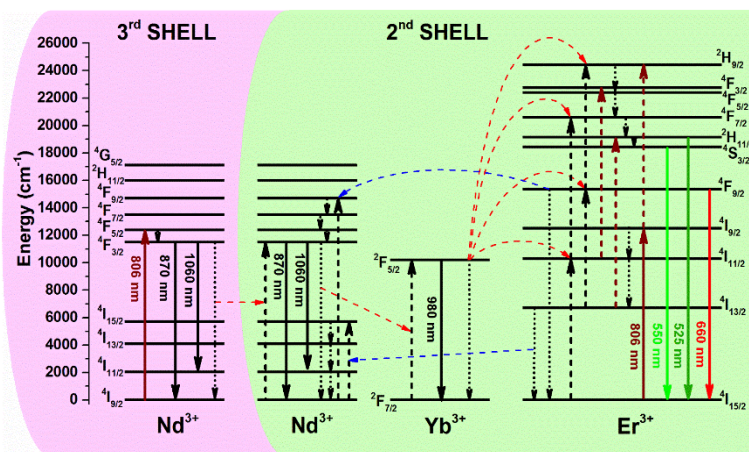


Figure 3.10 Energy transfer and UC mechanisms in MNPs1 upon 806 nm excitation. Brown, ascending solid arrows represent laser excitation. Dotted descending black arrows represent non-radiative de-excitation. Descending solid arrows represent emission. Ascending dashed arrows represent energy absorption (ascending brown dashed arrows represent ESA of 806 nm radiation). Red dashed arrows represent ET. Blue dashed arrows represent $\text{Er}^{3+} \rightarrow \text{Nd}^{3+}$ ET.

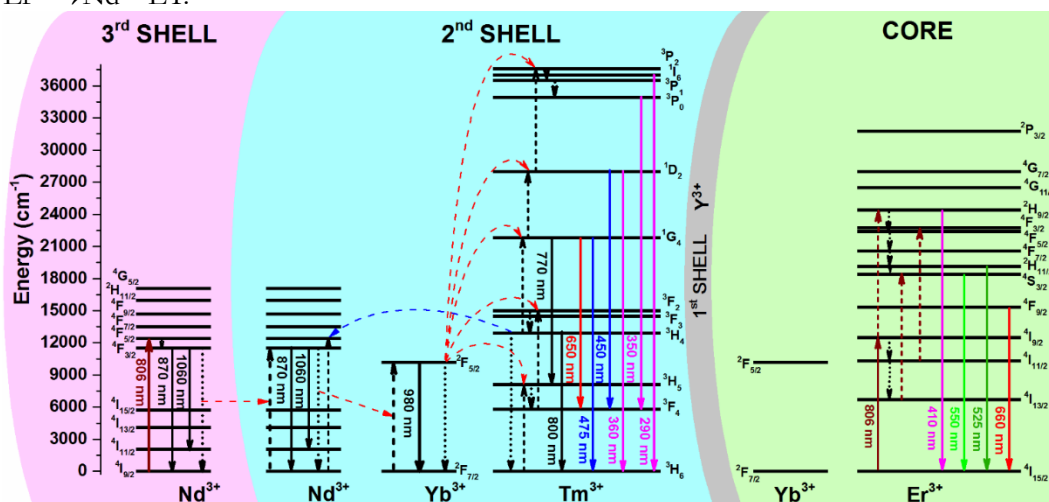
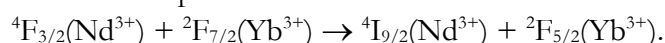


Figure 3.11 Energy transfer and UC mechanisms in MNPs2 upon 806 nm excitation. Brown, ascending solid arrows represent laser excitation. Dotted descending black arrows represent non-radiative de-excitation. Descending solid arrows represent emission. Ascending dashed arrows represent energy absorption (ascending brown dashed arrows represent ESA of 806 nm radiation). Red dashed arrows represent ET. Blue dashed arrows represent $\text{Tm}^{3+} \rightarrow \text{Nd}^{3+}$ ET.

The UC excitation and emission mechanisms for MNPs1 and MNPs2 are proposed in figures 3.10 and 3.11, respectively. In figure 3.10, only UC mechanisms for the outer shells of MNPs1 are shown, since Tm^{3+} ions in the core cannot be directly excited by 806 nm radiation, as evidenced by the lack of Tm^{3+} UC emission (figure 3.9a). Upon 806 nm excitation, the Yb^{3+} ions in the 2nd shell can be excited through an efficient $\text{Nd}^{3+} \rightarrow \text{Yb}^{3+}$ ET process⁶⁸:



This ET process is clearly demonstrated by the strong Yb^{3+} emission around 980 nm, observed in the Stokes spectra for the MNPs (see in the **NIR Stokes Emission** section). Due to the presence of the optically inert 1st shell between the core and the 2nd shell, excited Yb^{3+} ions cannot transfer their energy to the Tm^{3+} ions located in the

core. Nonetheless, after sensitization of the Yb^{3+} ion by Nd^{3+} , an energy transfer UC (ETU) mechanism between Yb^{3+} and Er^{3+} can take place generating Er^{3+} emission in the visible range. A second possible mechanism for populating higher energy levels of the Er^{3+} and therefore generating UC is by ground state absorption (GSA) followed by excited state absorption (ESA) of 806 nm excitation.⁶⁹ The very low emission intensity of Er^{3+} can be accounted for by an efficient $\text{Er}^{3+} \rightarrow \text{Nd}^{3+}$ ET (see figure 3.10) that depopulates the higher Er^{3+} energy levels.

Moreover, a direct $\text{Nd}^{3+} \rightarrow \text{Er}^{3+}$ ET is not very efficient, considering the very low Er^{3+} emission shown in figure 3.9a. The ET and UC mechanisms for MNPs2 upon 806 nm excitation are shown in figure 3.11. Unlike for MNPs1, UC emissions from both Tm^{3+} and Er^{3+} ions are observed, as shown in figure 3.9b. This behavior can be explained considering that the Er^{3+} ions in the core of the MNPs2 can be directly excited with 806 nm radiation and that $\text{Er}^{3+} \rightarrow \text{Yb}^{3+}$ ET is negligible. Two different processes take place simultaneously in MNPs2, the first involving the two external shells (2nd and 3rd shells) and the second involving only the core. In the two external shells GSA of the 806 nm radiation by Nd^{3+} ions is active, followed by the $\text{Nd}^{3+} \rightarrow \text{Yb}^{3+}$ ET and then an ETU mechanism from Yb^{3+} to Tm^{3+} populates the Tm^{3+} excited states and generate the Tm^{3+} emission⁷⁰. Simultaneously, a $\text{Tm}^{3+} \rightarrow \text{Nd}^{3+}$ ET pathway can be active, similar to the one found for the Er^{3+} ions in MNPs1^{65-66, 71}. The Tm^{3+} emission observed for the MNPs2 could be in principle also due to a direct $\text{Nd}^{3+} \rightarrow \text{Tm}^{3+}$ ET, without the assistance of the Yb^{3+} ions. On the other hand, Chung et al. found that the $\text{Nd}^{3+} \rightarrow \text{Tm}^{3+}$ ET process for a co-doped glass material is around two order of magnitude slower than the opposite $\text{Tm}^{3+} \rightarrow \text{Nd}^{3+}$ ET⁷¹. Therefore, it is reasonable that the population of the Tm^{3+} excited levels is mainly due to ETU mechanisms from Yb^{3+} to Tm^{3+} ions. One possible explanation of the stronger Tm^{3+} emission intensity can be figured out by considering the lower Tm^{3+} concentration (0.2 %) in the 2nd shell of MNPs2 with respect to the Er^{3+} concentration (2 %) in the 2nd shell of MNPs1, or by a better overlap among the energy levels of the donor and the acceptor ions, as previously mentioned. Since ET is a concentration dependent process, the efficiency of the $\text{Tm}^{3+} \rightarrow \text{Nd}^{3+}$ ET process could be lower than the $\text{Er}^{3+} \rightarrow \text{Nd}^{3+}$ one. UC emission bands for Er^{3+} ions are still observed in MNPs2 (figure 3.9b), since the Er^{3+} ions in the core are excited through GSA and ESA upon 806 nm laser irradiation while the presence of the optically inert 1st shell prevents the $\text{Er}^{3+} \rightarrow \text{Nd}^{3+}$ ET.

From the analysis of the UC emission of the MNPs upon 980 and 806 nm excitation, it is clear that it is possible to generate different UC emission from the same MNPs by simply changing the excitation wavelength. This behavior is particularly marked for MNPs2, for which up to more than 90% of the total emission upon 980 nm excitation stems from the Er^{3+} ion. On the other hand, the behavior for MNPs1 upon 980 nm excitation is quite peculiar, because almost 95 % of the visible UC, is due to Tm^{3+} ions, while the Er^{3+} emission is almost completely quenched by the above-mentioned $\text{Er}^{3+} \rightarrow \text{Nd}^{3+}$ ET process.

NIR Stokes emission. The Nd^{3+} ions in the MNPs act as radiation harvesters, while the Yb^{3+} ions do not absorb at a wavelength of 806 nm. In order to increase the radiation harvesting, the Nd^{3+} concentration in the 3rd shell was kept to 22% with respect to the total metal ion content. However, Nd^{3+} ions in the outer shell act as antennas for 806 nm radiation, that can be transferred through ET migration to the Nd^{3+}

ions in the next shell. If the nanoparticle design was including a 22% Nd^{3+} ion concentration in the second shell instead, Nd^{3+} would totally quench the Er^{3+} and Tm^{3+} emission, eliminating the option of having visible emissions, and would even quench the NIR emissions from Nd^{3+} ions themselves through non-radiative de-excitation processes⁷². To overcome this fact, a small amount of Nd^{3+} ions (1% concentration, see figure 3.1) is present in the 2nd shell, guaranteeing efficient NIR Nd^{3+} emission. On the other hand, at the MNPs concentrations used in this study, no temperature variations for the water dispersions (ca. 1 % wt) were observed upon cw 806 nm laser excitation for the experimental time needed to acquire the spectrum. The emission spectra at 20°C for the three MNPs upon 806 nm excitation are shown in figure 3.12. As the investigation was focused on Nd^{3+} and Yb^{3+} NIR emission in the presence of Er^{3+} or Tm^{3+} ions as co-dopants in the 2nd shell of the MNPs, as a reference system, MNPs3 (see figure 3.1) was doped solely with Yb^{3+} and Nd^{3+} ions in the 2nd shell. NIR emission spectra, clearly indicate that the presence of Er^{3+} or Tm^{3+} ions in the 2nd shells of the MNPs significantly affects the relative emissions of Nd^{3+} and Yb^{3+} ions. In particular, the $\text{Yb}^{3+}/\text{Nd}^{3+}$ intensity ratio decreases on passing from MNPs3 to MNPs2 and to MNPs1. This behavior could be explained by the $\text{Yb}^{3+} \rightarrow \text{Tm}^{3+}$ and $\text{Yb}^{3+} \rightarrow \text{Er}^{3+}$ ET processes for MNPs2 and MNPs1, respectively (figures 3.10 and 3.11). In the case of the reference MNPs3 only the $\text{Nd}^{3+} \rightarrow \text{Yb}^{3+}$ ET process is present.

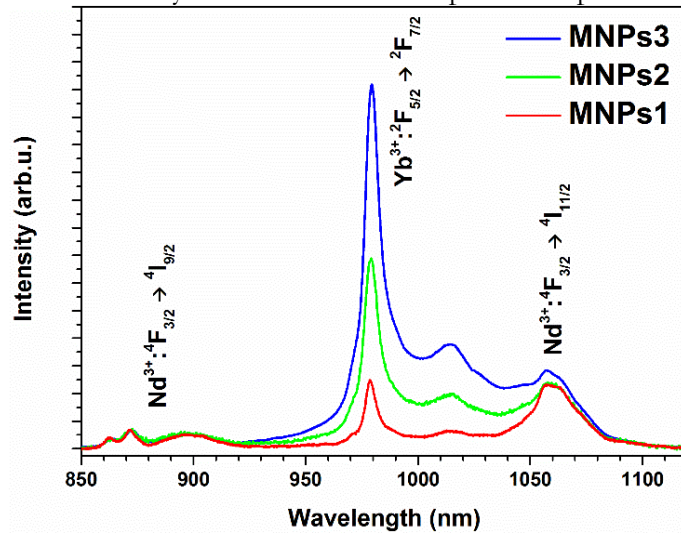


Figure 3.12 NIR emission of the three MNPs ($\lambda_{\text{exc}}=806$). The spectra are normalized to the Nd^{3+} 870 nm emission.

The difference in the $\text{Yb}^{3+}/\text{Nd}^{3+}$ emission intensity ratio between MNPs1 and MNPs2 could be accounted for the different concentrations of Er^{3+} and Tm^{3+} ions, in the respective structures (see Figure 1), as $\text{Yb}^{3+} \rightarrow \text{Er}^{3+}$ or $\text{Yb}^{3+} \rightarrow \text{Tm}^{3+}$ ET processes are present.

In order to shed light on this behavior, *ad-hoc* C@S NPs were synthesized, with the following composition:

- $\text{SrF}_2:\text{Yb}(22\%),\text{Er}(x\%),\text{Nd}(2\%)@\text{Nd}(22\%)$ (C@S_Er)
- $\text{SrF}_2:\text{Yb}(22\%),\text{Tm}(x\%),\text{Nd}(2\%)@\text{Nd}(22\%)$ (C@S_Tm)

with $x=0.2, 0.5, 1$ or 2% . For these NPs, the concentrations of Yb^{3+} and Nd^{3+} ions are the same as those in the 2nd and 3rd shells of MNPs1 and MNPs2, respectively. It should be noted that the Yb^{3+} and Er^{3+} or Tm^{3+} ions are distributed in a sphere in the C@S structure rather than in a shell for the MNPs. Nonetheless, since the concentration of the lanthanide ions are the same, we are confident that the donor (Yb^{3+}) and acceptor (Er^{3+} or Tm^{3+}) average distance would be also the same and therefore an investigation on the C@S NPs would be significant for understanding the ET dynamics in the MNPs. These C@S NPs were prepared with the same hydrothermal technique as the MNPs. Detailed TEM analysis for these C@S NPs confirm the shell growth (see figure 3.13).

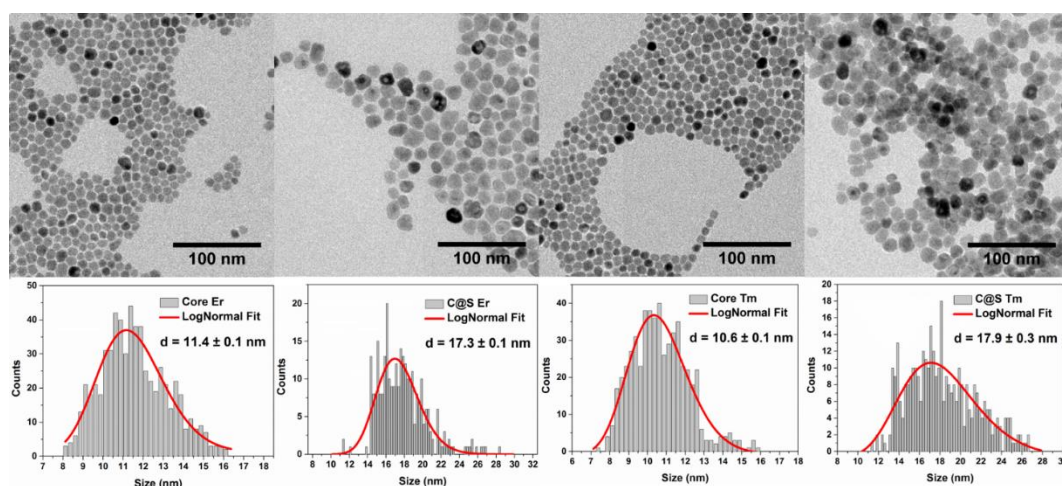


Figure 3.13 TEM for core@shell NPs.

NIR emission spectra for water colloidal dispersions (1 %wt) of the several C@S NPs were measured with a spectrofluorometer with a Xenon lamp 573 nm radiation and will be shown in figure 3.15. As a representative example, the absorption spectrum for the C@S:Tm(0.2%) in the visible and NIR range was measured at room temperature and it is shown in figure 3.14. In this spectrum, typical absorption bands of both Nd^{3+} and Yb^{3+} ions can be observed, while the Tm^{3+} absorption are not observable due to the small concentration of the Tm^{3+} ions (0.2%) with respect to the Nd^{3+} or Yb^{3+} ions one. A strong absorption band is clearly present around 800 nm, due to the $^4\text{I}_{9/2} \rightarrow ^4\text{F}_{5/2}$ for Nd^{3+} ions transition. Moreover, as shown by the absorption spectrum, light radiation at 573 nm is strongly absorbed by the Nd^{3+} ions, inducing population of the $^4\text{G}_{5/2}$ and $^2\text{G}_{7/2}$ excited energy levels (see also figure 3.10). It is worth remarking that Er^{3+} or Tm^{3+} ions are not directly excited by the 573 nm radiation as they do not absorb at this radiation wavelength ⁷³.

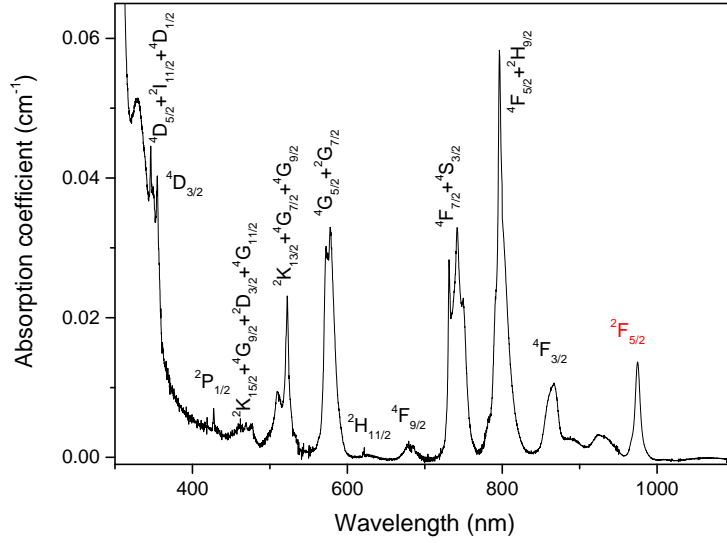


Figure 3.14 Absorption spectrum for a water colloidal dispersion of the SrF₂:Yb,Tm(0.2%),Nd@Nd core@shell NPs. Transitions starting from the ⁴I_{9/2} ground state of Nd³⁺ ions are indicated in black, while transitions starting from the ²F_{7/2} ground state of Yb³⁺ ions are indicated in red. The room temperature absorption spectrum has been measured with a Cary 5000 spectrophotometer.

Then, after rapid non-radiative relaxations to the low energy lying levels, the Nd³⁺ ions decay to the ⁴F_{3/2} level from which the abovementioned Nd³⁺→Yb³⁺ and Yb³⁺→Er³⁺ or Yb³⁺→Tm³⁺ ET processes (see figures 3.10 and 3.11) take place. From the NIR emission spectra of the C@S NPs, shown in figure 3.15, it can be noted that the Yb³⁺ emission around 980 nm decreases monotonically with respect to the Nd³⁺ one around 1060 nm as the concentration of the Er³⁺ or Tm³⁺ increases. This behavior strongly suggests that the Yb³⁺→Er³⁺ and Yb³⁺→Tm³⁺ ET processes become more and more efficient as the Er³⁺ or Tm³⁺ concentrations increase. This behavior can be clearly observed by evaluating the Fluorescence Intensity Ratio between the Yb³⁺ and Nd³⁺ integrated emissions, FIR(Yb,Nd), defined as

$$FIR(Yb, Nd) = \frac{A_{980}(Yb^{3+})}{A_{1060}(Nd^{3+})} \quad (3.1)$$

where A denotes the integrated areas, highlighted with green regions in figure 3.15.

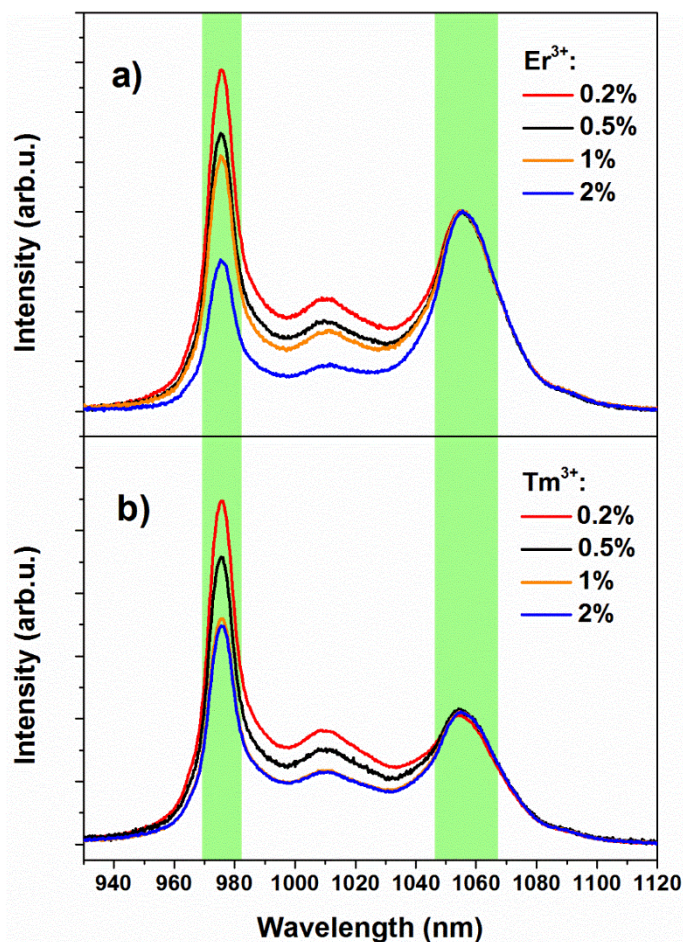


Figure 3.15 NIR emission spectra for a) SrF₂:Yb,Er,Nd@Nd core@shell NPs with different Er³⁺ concentrations and b) SrF₂:Yb,Tm,Nd@Nd NPs with different Tm³⁺ concentrations.

The integrated areas were chosen in order to have a significant integration range around the main peaks at 980 and 1060 nm, for Yb³⁺ and Nd³⁺ respectively, while minimizing overlap between bands for different transitions. In figure 3.16 the FIR(Yb,Nd) for the C@S NPs are shown, from which a clear decrease of the FIR(Yb,Nd) on increasing the Er³⁺ or Tm³⁺ concentration is observed. Moreover, the FIR(Yb,Nd) values for the case of C@S_Er NPs are lower than for the C@S_Tm NPs for every Ln ion concentration, suggesting that the ET process is more efficient for the Er³⁺ doped C@S_Er NPs. This behavior can be probably ascribed to the resonant nature of the Yb³⁺→Er³⁺ ET process⁷⁴ that could be more efficient than the non-resonant Yb³⁺→Tm³⁺ energy ET transfer (see figures 3.10 and 3.11).

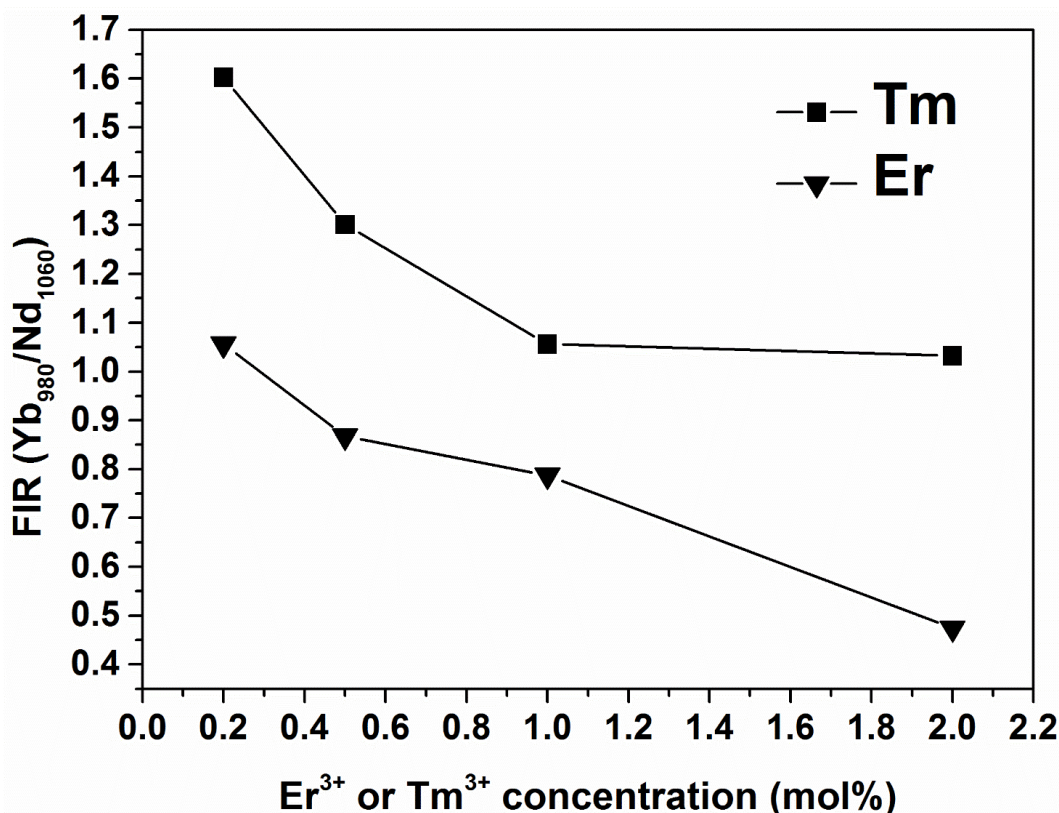


Figure 3.16 Fluorescence Intensity Ratio FIR(Yb,Nd) between the Yb³⁺ integrated emission and the Nd³⁺ one. The integration area is indicated in figure 3.15 (green area) for SrF₂:Yb,Tm,Nd@Nd nanoparticles (squares) and SrF₂:Yb,Er,Nd@Nd nanoparticles (triangles). The lines are guides for the eyes.

NIR Thermometry

The capabilities of the present MNPs as luminescent NTHs in the II-BW have been investigated by analyzing the variation of the NIR emission spectra in the physiological temperature range. The Stokes emission in the NIR range, upon 806 nm excitation, of the MNPs has been measured as a function of temperature in the 20°-60°C range, in figure 3.17 the emission spectra at 20°C and 60°C are shown. The spectra clearly show that the Yb³⁺/Nd³⁺ emission intensity ratio significantly decreases by increasing the temperature. The FIR(Yb,Nd) defined as above, has been evaluated, by integrating the emission signal over a suitable integration range around the Yb³⁺ (around 980 nm) and Nd³⁺ (around 1060 nm) peak emissions. The abovementioned bands for the two Ln ions were chosen because of their higher emission intensities with respect to the Nd³⁺ one at 870 nm and the Yb³⁺ one at 1015 nm (see figure 3.17).

In figure 3.18a the variation of the FIR(Yb,Nd) for the MNPs as a function of the temperature is shown, in all cases, FIR values decrease following a linear behavior. The dependence of the FIR(Yb,Nd) on the temperature has been found to follow different behaviors for different compounds, as for LiLa_{0.9-x}Nd_{0.1}Yb_xP₄O₁₂ NPs in the 300-400 K temperature range the FIR(Yb,Nd) is increasing on increasing the temperature⁷⁵.

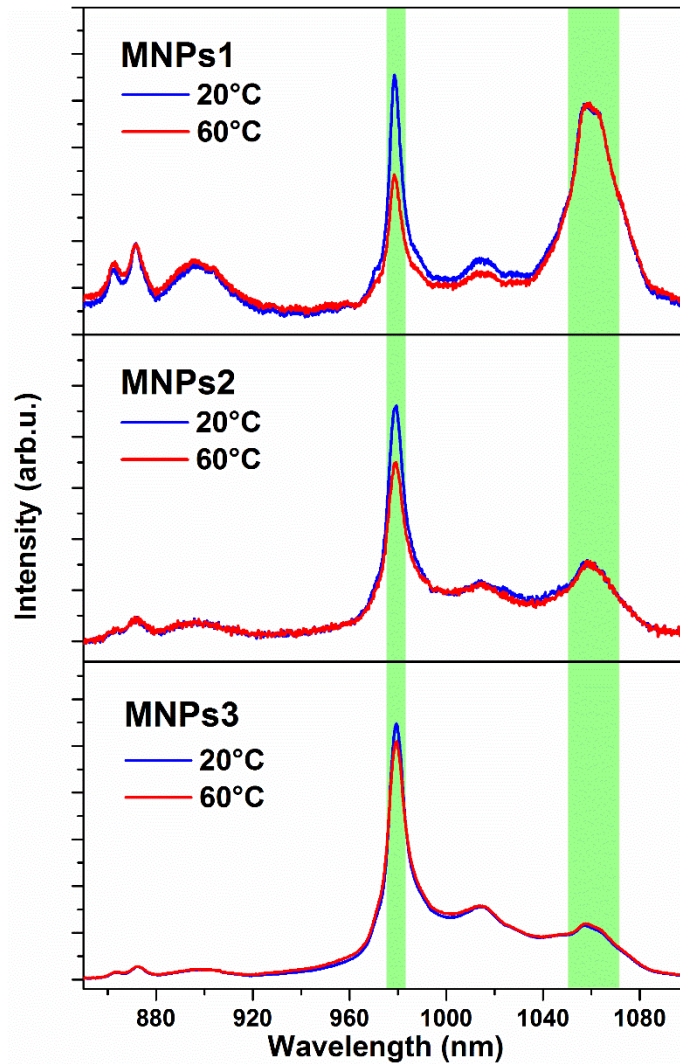


Figure 3.17 NIR emission spectra ($\lambda_{\text{exc}} = 806 \text{ nm}$) for the MNPs at different temperatures. The spectra are normalized to the Nd^{3+} emission.

On the other hand, the behavior for the present MNPS is similar to that found by Ximendes et al. for $\text{Nd}^{3+}, \text{Yb}^{3+}$ doped LaF_3 nanoparticles⁷². Since a non-resonant ET between Nd^{3+} and Yb^{3+} ions is present (see figures 3.10 and 3.11), a phonon assisted mechanism has to be active, described by the Miyakawa–Dexter (MD) model.⁷⁶ Importantly, besides the direct $\text{Nd}^{3+} \rightarrow \text{Yb}^{3+}$ ET, also the back ET $\text{Nd}^{3+} \leftarrow \text{Yb}^{3+}$ can occur⁷⁷⁻⁷⁸. Therefore, the negative or positive slope for the FIR(Yb, Nd) vs temperature depends by a subtle balance between these two processes. This behavior is therefore clearly dependent on the local environment around the Nd^{3+} and Yb^{3+} ions in the particular host where they are accommodated that strongly influence the Stark energy levels for the Ln ions. Since in our case we observe a negative slope for the FIR vs temperature for all the MNPS (see figure 3.18a) a $\text{Nd}^{3+} \leftarrow \text{Yb}^{3+}$ back transfer is most probably the dominant mechanism producing the Yb^{3+} emission decrease with respect to the Nd^{3+} emission. In order to clarify this point, an absorption spectrum in the NIR region for the MNPs was measured and it is shown in figure 3.19 overlapped with the emission spectrum obtained by excitation at 806 nm. It can be clearly observed that

the bands at 980 nm, that are the most prominent feature for the two spectra, are perfectly overlapped, indicating that this band derives from a transition involving the Yb^{3+} ion ground state.

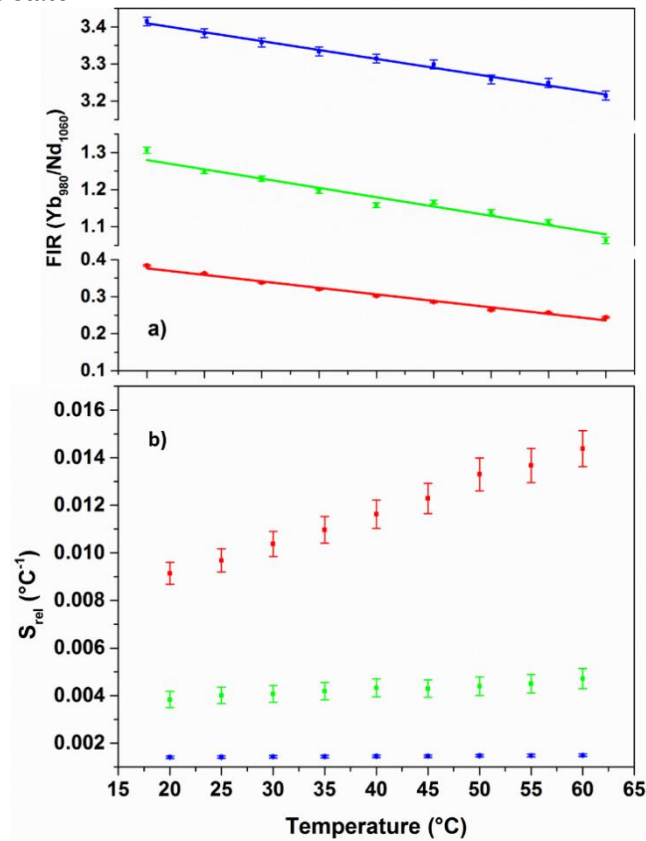


Figure 3.18 FIR(Yb,Nd) (a) and relative sensitivity S_{rel} (b) for MNPs1 (red), MNPs2 (green) and MNPs3 (blue). Error bars on S_{rel} are evaluated considering an error propagation procedure from the uncertainties of the FIR(Yb,Nd) values.

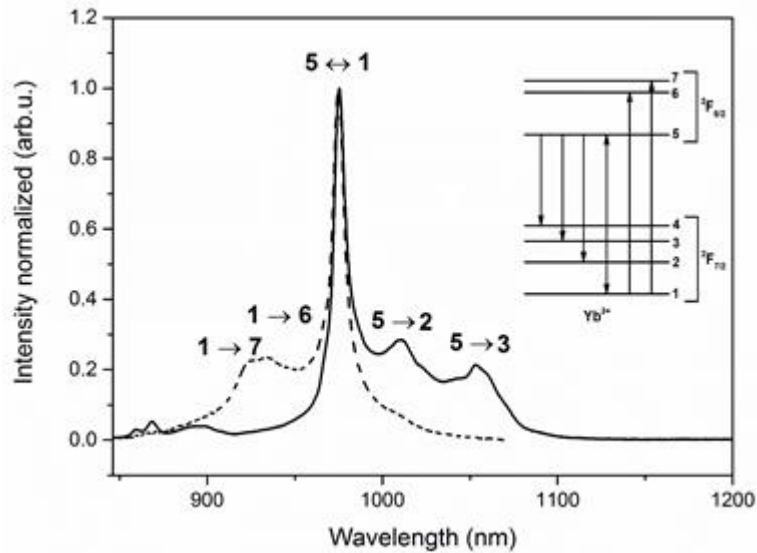


Figure 3.19 MNP3 NIR absorption (dashed line) and emission (solid line) upon 806 nm excitation.

Due to the Kramers degeneracy, three and four Stark energy states are expected for the $^2F_{5/2}$ and $^2F_{7/2}$ excited and ground levels of the Yb^{3+} ion, respectively. Falin et al.,

from an optical spectroscopy investigation on Yb³⁺ doped SrF₂ samples, found that the absorption or the emission band at 980 nm is due to a transition between the lowest Stark states of both the ²F_{5/2} and ²F_{7/2} levels⁷⁹. This transition is shown in the inset of figure 3.19 with an energy level scheme for the Yb³⁺ ions, following Falin et al. Then, following the Nd³⁺→Yb³⁺ ET process, a thermalization of the three Stark levels of the ²F_{5/2} of the Yb³⁺ ions takes place. On increasing the temperature, it is conceivable that the population of the lowest Stark state of the Yb³⁺ ²F_{5/2} level decreases, while the two higher Stark states are more and more populated. Therefore, it is reasonable that the emission at 980 nm, starting from the lowest Stark state of the Yb³⁺ ²F_{5/2} level, weakens on increasing the temperature, in perfect agreement with what observed in our investigation. The decrease of the FIR(Yb,Nd) vs temperature can be therefore explained by the decrease of the population of the lowest Stark state of the Yb³⁺ ²F_{5/2} level. It is to be remarked that the behaviors vs temperature of the FIR(Yb,Nd) for the MNPs, although monotonically decreasing, are different, as shown in figures 3.17 and 3.18a, due to the Yb³⁺→Er³⁺ or Yb³⁺→Tm³⁺ ET processes for MNPs1 and MNPs2, respectively.

The absolute thermal sensitivity S can be defined as⁸⁰⁻⁸¹

$$S = \left| \frac{\partial \text{FIR}(\text{Yb}, \text{Nd})}{\partial T} \right| \quad (3.2)$$

where T represents the temperature. Therefore, the absolute thermal sensitivity values (denoted as S) are considered constants in the temperature range from 20 to 60 °C and they are evaluated as the slopes of the linear regression fits for the FIR(Yb,Nd) vs T , shown in figure 18a. The MNPs3 and MNPS2 show very similar values of absolute sensitivities, $(4.8 \pm 0.2) \cdot 10^{-3} \text{ } ^\circ\text{C}^{-1}$ and $(5.0 \pm 0.4) \cdot 10^{-3} \text{ } ^\circ\text{C}^{-1}$, respectively, while MNPs1 have an absolute thermal sensitivity of $(3.5 \pm 0.2) \cdot 10^{-3} \text{ } ^\circ\text{C}^{-1}$.

Nonetheless, in order to compare the thermometric performances of the present MNPs with those reported in the literature, the relative thermal sensitivities, S_{rel} , were calculated:

$$S_{rel} = \frac{S}{\text{FIR}(\text{Yb}, \text{Nd})} \quad (3.3)$$

where S is the absolute sensitivity, and they are shown in figure 3.18b. The relative sensitivity is in fact the commonly accepted parameter for direct comparison of various nanothermometers, in particular with different Ln ion doping^{80, 82}. The relative thermal sensitivities in the considered temperature range were estimated to be around $4 \cdot 10^{-3} \text{ } ^\circ\text{C}^{-1}$ and $1.5 \cdot 10^{-3} \text{ } ^\circ\text{C}^{-1}$ for MNPs2 and MNPs3, respectively, with slight temperature dependent variation. While, for MNPs1 the S_{rel} value significantly increased on increasing the temperature, from $(9.1 \pm 0.5) \cdot 10^{-3} \text{ } ^\circ\text{C}^{-1}$ at 20 °C to $(14.4 \pm 0.8) \cdot 10^{-3} \text{ } ^\circ\text{C}^{-1}$ at 60 °C. Therefore, it can be assumed, that the presence of Er³⁺ in the 2nd shell strongly improves the thermal sensitivity based on FIR(Yb,Nd). It could be emphasized that the efficient Yb³⁺→Er³⁺ ET is beneficial for the thermometric properties, lowering the FIR(Yb,Nd) with respect to the case in which only Yb³⁺ and Nd³⁺ are doped in the 2nd shell.

Moreover, the significant difference between the room temperature FIR(Yb,Nd) of MNPs1 with respect to MNPs2 is most probably due to the higher Er³⁺ concentration in the 2nd shell of MNPs1 with respect to that of Tm³⁺ in the 2nd shell of MNPs2, as described above, although a better level overlap among the donor and acceptor energy

levels could also contribute to this behavior. A comparison between the MNPs thermometric performances and the most recent Nd^{3+} or $\text{Nd}^{3+}/\text{Yb}^{3+}$ based NTHs investigated in literature is reported in Table 3.2. We have to remark that while the relative sensitivities of MNPs3 and MNPS2 are similar to those reported in the literature, the S_{rel} for MNPs1 are the highest reported for NIR-to-NIR NTHs operating in the II-BW in water dispersions based on a single host (SrF_2 in this study), although multishell structured. Higher thermal sensitivity has been determined in hybrid poly(lactic-co-glycolic) acid (PLGA) nanostructures, constitutes by $\text{NaGdF}_4:\text{Nd}^{3+}$ NPs and $\text{PbS}/\text{CdS}/\text{ZnS}$ quantum dots that have been encapsulated in PLGA, with a S_{rel} of $2.5 \cdot 10^{-2} \text{ }^\circ\text{C}^{-1}$ ⁸¹. Nonetheless, the present multishell nanoparticles are much smaller (around 25 nm) than the abovementioned PLGA nanostructures (around 150 nm) and therefore they could be more useful in application where size is an issue, such as in the biomedical field.

Table 3.2 Comparison between different Nd^{3+} or $\text{Nd}^{3+}/\text{Yb}^{3+}$ based nanothermometers

Material	Sample form	λ_{exc} (nm)	λ_{em} (nm)	Temperature range ($^\circ\text{C}$)	$S_{rel}(\cdot 10^{-2} \text{ }^\circ\text{C}^{-1})^a$	Temperature of S_{MAX} ($^\circ\text{C}$)	Reference
MNPs1 $\text{SrF}_2:\text{Yb},\text{Tm}@Y@Yb,\text{Er},\text{Nd}@Nd$	Water dispersion	806	980, 1060	20 \rightarrow 60	1.49 ± 0.08	60	This work
$\text{Gd}_2\text{O}_3:\text{Nd}$	Powder sample	580	825, 890	15 \rightarrow 50	1.75 ± 0.04	15	[83]
YAG:Nd	Water dispersion	808	940	10 \rightarrow 70	0.15	N/A	[84]
$\text{LiLaPO}_4:\text{Nd},\text{Yb}$	Powder sample	808	870, 980, 1050	-180 \rightarrow 390	0.3	30	[75]
$\text{NaYF}_4:\text{Yb},\text{Er}@Yb,\text{Nd}$	Powder sample	808	980, 1050	-70 \rightarrow 180	2.1	100	[85]
$\text{LaF}_3:\text{Nd},\text{Yb}$	Water dispersion	808	1000, 1060, 1350	15 \rightarrow 50	0.75	15	[72]
$\text{LiLaP}_4\text{O}_{12}:\text{Cr},\text{Nd}$	Powder sample	665	830, 1050	-160 \rightarrow 200	4.89 ^b	50	[86]

^a highest value of the relative thermal sensitivity reported in the references.

^b this value is the maximum reported for the physiological temperature range (20 $^\circ\text{C}$ \rightarrow 60 $^\circ\text{C}$).

One of the most relevant parameter describing the thermometric performance is the temperature uncertainty ΔT , which defines the achievable precision of the temperature evaluation in the local environment in which the thermometer is working. This important parameter is defined as³¹:

$$\Delta T = \frac{\Delta \text{FIR}}{\text{FIR} \cdot S_{rel}} \quad (3.4)$$

where $\Delta \text{FIR}/\text{FIR}$ is the relative uncertainty of the thermometric parameter (in our case, $\text{FIR}(\text{Yb},\text{Nd})$). It is important to remark that $\Delta \text{FIR}/\text{FIR}$ depends on the measurement setup and in particular on the signal to noise ratio of the measured signal. Taking

into account the FIR(Yb,Nd) values and their corresponding errors, the ΔT values have been evaluated and are shown in figure 3.20.

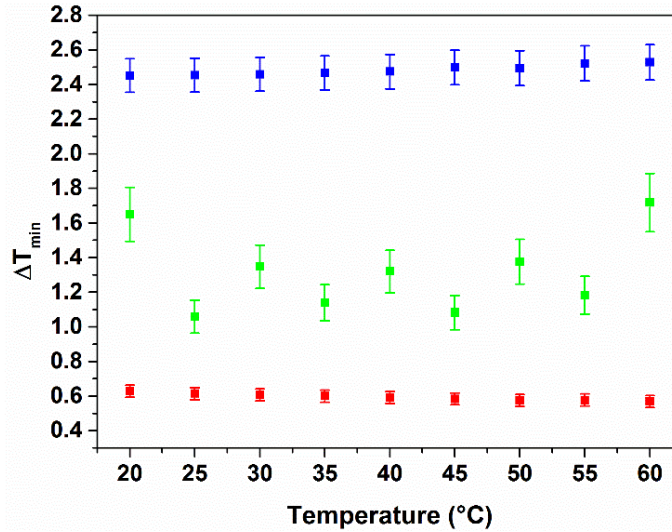


Figure 3.20 Minimum temperature variation measurable with MNPs1 (red), MNPs2 (green) and MNPs3.

The ΔT values are 0.5-0.6 °C for MNPs1, 1.0-1.6 °C for MNPs2 and 2.4-2.5 °C for MNPs3. Therefore, MNPs1 confirms to possess the best thermometric performances among the MNPs shown in this investigation. The minimum measurable ΔT can be further improved by modifying the MNPs to increasing their S_{rel} , as well as by refining the spectral acquisitions in order to increase the signal to noise ratio, hence decreasing the relative uncertainty of the FIR values.

3.4 Conclusion

In summary, we prepared Ln-doped core@multishell nanostructured systems (MNPs) based on the SrF₂ host. From a careful structural and morphological analysis, the confirm of their multi shell structure has been achieved. The nanosystems can be easily and efficiently dispersed in water as well as in physiological solutions, assuring their possible use in biomedicine. From a detailed spectroscopic investigation, we demonstrated that the MNPs are multifunctional tools for possible use as diagnostic tools in bioimaging in the visible range and NIR in the II-BW, with the possibility of double excitation in the I-BW at 980 and 800 nm within the same MNPs. The possibility of a multicolor UC emission was clearly demonstrated and the possible UC mechanisms were investigated. Through a proper structure architecture, it was possible to tune the emission properties by properly doping with the Ln ions (such as Er³⁺ or Tm³⁺) in the proper core or shell layer. NIR spectroscopy of the MNPs exhibits a strong emission from Yb³⁺ and Nd³⁺ ions in the II-BW upon excitation at 806 nm. Moreover, the Yb³⁺/Nd³⁺ emission ratio appears to be strongly influenced by the presence of a third dopant ion in the shell layer. A thermometric investigation confirmed that the MNPs under investigation are also efficient NIR nanothermometers based on Yb³⁺ and Nd³⁺ emissions. MNPs1 showed the best performance thanks to Er³⁺ co-

doping together with Yb^{3+} and Nd^{3+} in the 2nd shell layer, providing a high FIR percentage variation around 40%, while MNPs2 and MNPs3 show relative thermal sensitivities in line with the values reported in the literature for the majority of NIR-to-NIR optical NTHs. In particular, MNPs1 show a very high thermal relative sensitivity in the 20-60 °C temperature range, from $(0.9 \pm 0.08) \cdot 10^{-2} \text{ } ^\circ\text{C}^{-1}$ to $(1.49 \pm 0.08) \cdot 10^{-2} \text{ } ^\circ\text{C}^{-1}$, strongly indicating their suitability as NTHs in nanomedicine. Underlining that the thermometry features for the MNPs were carried out in water colloidal dispersion, to the best of our knowledge their relative sensitivity values are the highest reported for water dispersible NIR-to-NIR NTHS working in the II-BW highest reported for NIR-to-NIR NTHs based on a single nanoparticle. MNPs1 presents also the minimum measurable temperature variation ΔT , also for its high S_{rel} value.

REFERENCES

1. Jaque, D.; Richard, C.; Viana, B.; Soga, K.; Liu, X.; García Solé, J., Inorganic nanoparticles for optical bioimaging. *Advances in Optics and Photonics* **2016**, *8* (1), 1.
2. Ranjan, S.; Jayakumar, M. K. G.; Zhang, Y., Luminescent lanthanide nanomaterials: an emerging tool for theranostic applications. *Nanomedicine-Uk* **2015**, *10* (9), 1477-1491.
3. Naczynski, D. J.; Tan, M. C.; Riman, R. E.; Moghe, P. V., Rare Earth Nanoprobes for Functional Biomolecular Imaging and Theranostics. *Journal of Materials Chemistry B* **2014**.
4. Ortgies, D. H.; de la Cueva, L.; Del Rosal, B.; Sanz-Rodriguez, F.; Fernandez, N.; Iglesias-de la Cruz, M. C.; Salas, G.; Cabrera, D.; Teran, F. J.; Jaque, D.; Martin Rodriguez, E., In Vivo Deep Tissue Fluorescence and Magnetic Imaging Employing Hybrid Nanostructures. *ACS Appl Mater Interfaces* **2016**.
5. Prodi, L.; Rampazzo, E.; Rastrelli, F.; Speghini, A.; Zaccheroni, N., Imaging agents based on lanthanide doped nanoparticles. *Chem Soc Rev* **2015**, *44* (14), 4922-52.
6. Bettinelli, M.; Carlos, L.; Liu, X., Lanthanide-doped upconversion nanoparticles. *Physics Today* **2015**, *68* (9), 38-44.
7. Gu, Z. J.; Yan, L.; Tian, G.; Li, S. J.; Chai, Z. F.; Zhao, Y. L., Recent Advances in Design and Fabrication of Upconversion Nanoparticles and Their Safe Theranostic Applications. *Adv Mater* **2013**, *25* (28), 3758-3779.
8. Rocha, U.; Kumar, K. U.; Jacinto, C.; Villa, I.; Sanz-Rodriguez, F.; de la Cruz, M. D. I.; Juarranz, A.; Carrasco, E.; van Veggel, F. C. J. M.; Bovero, E.; Sole, J. G.; Jaque, D., Neodymium-Doped LaF₃ Nanoparticles for Fluorescence Bioimaging in the Second Biological Window. *Small* **2014**, *10* (6), 1141-1154.
9. Vijayaraghavan, P.; Liu, C. H.; Vankayala, R.; Chiang, C. S.; Hwang, K. C., Designing multi-branched gold nanoechinus for NIR light activated dual modal photodynamic and photothermal therapy in the second biological window. *Advanced materials* **2014**, *26* (39), 6689-95.
10. Maestro, L. M.; Ramirez-Hernandez, J. E.; Bogdan, N.; Capobianco, J. A.; Vetrone, F.; Sole, J. G.; Jaque, D., Deep tissue bio-imaging using two-photon excited CdTe fluorescent quantum dots working within the biological window. *Nanoscale* **2012**, *4* (1), 298-302.
11. Park, Y. I.; Lee, K. T.; Suh, Y. D.; Hyeon, T., Upconverting nanoparticles: a versatile platform for wide-field two-photon microscopy and multi-modal in vivo imaging. *Chemical Society Reviews* **2014**.
12. Chen, D. Q.; Yu, Y. L.; Huang, F.; Lin, H.; Huang, P.; Yang, A. P.; Wang, Z. X.; Wang, Y. S., Lanthanide dopant-induced formation of uniform sub-10 nm active-core/active-shell nanocrystals with near-infrared to near-infrared dual-modal luminescence. *J Mater Chem* **2012**, *22* (6), 2632-2640.
13. Xie, X.; Gao, N.; Deng, R.; Sun, Q.; Xu, Q.-H.; Liu, X., Mechanistic Investigation of Photon Upconversion in Nd³⁺-Sensitized Core-Shell Nanoparticles. *Journal of the American Chemical Society* **2013**, 130819131610004.
14. Smith, A. M.; Mancini, M. C.; Nie, S. M., BIOIMAGING Second window for in vivo imaging. *Nat Nanotechnol* **2009**, *4* (11), 710-711.
15. Shen, J.; Chen, G. Y.; Ohulchanskyy, T. Y.; Kesseli, S. J.; Buchholz, S.; Li, Z. P.; Prasad, P. N.; Han, G., Tunable Near Infrared to Ultraviolet Upconversion Luminescence Enhancement in (alpha-NaYF₄:Yb,Tm)/CaF₂ Core/Shell Nanoparticles for In situ Real-time Recorded Biocompatible Photoactivation. *Small* **2013**, *9* (19), 3213-3217.
16. Hao, S. W.; Yang, L. M.; Qiu, H. L.; Fan, R. W.; Yang, C. H.; Chen, G. Y., Heterogeneous core/shell fluoride nanocrystals with enhanced upconversion photoluminescence for in vivo bioimaging. *Nanoscale* **2015**, *7* (24), 10775-10780.

17. Huang, X., Giant enhancement of upconversion emission in (NaYF₄:Nd³⁺/Yb³⁺/Ho³⁺)/(NaYF₄:Nd³⁺/Yb³⁺) core/shell nanoparticles excited at 808 nm. *Opt Lett* **2015**, *40* (15), 3599-602.
18. Chen, G.; Ågren, H.; Ohulchanskyy, T. Y.; Prasad, P. N., Light upconverting core-shell nanostructures: nanophotonic control for emerging applications. *Chemical Society Reviews* **2014**.
19. Chen, G.; Damasco, J.; Qiu, H.; Shao, W.; Ohulchanskyy, T. Y.; Valiev, R. R.; Wu, X.; Han, G.; Wang, Y.; Yang, C.; Ågren, H.; Prasad, P. N., Energy-Cascaded Upconversion in an Organic Dye-Sensitized Core/Shell Fluoride Nanocrystal. *Nano Lett* **2015**, *15* (11), 7400-7.
20. Li, Y.; Tang, J.; Pan, D. X.; Sun, L. D.; Chen, C.; Liu, Y.; Wang, Y. F.; Shi, S.; Yan, C. H., A Versatile Imaging and Therapeutic Platform Based on Dual-Band Luminescent Lanthanide Nanoparticles toward Tumor Metastasis Inhibition. *ACS Nano* **2016**, *10* (2), 2766-73.
21. Vetrone, F.; Naccache, R.; Zamarron, A.; de la Fuente, A. J.; Sanz-Rodriguez, F.; Maestro, L. M.; Rodriguez, E. M.; Jaque, D.; Sole, J. G.; Capobianco, J. A., Temperature Sensing Using Fluorescent Nanothermometers. *ACS Nano* **2010**, *4* (6), 3254-3258.
22. Jaque, D.; Vetrone, F., Luminescence nanothermometry. *Nanoscale* **2012**, *4* (15), 4301-26.
23. Jaque, D.; del Rosal, B.; Rodriguez, E. M.; Maestro, L. M.; Haro-Gonzalez, P.; Sole, J. G., Fluorescent nanothermometers for intracellular thermal sensing. *Nanomedicine-Uk* **2014**, *9* (7), 1047-1062.
24. Zhegalova, N. G.; Dergunov, S. A.; Wang, S. T.; Pinkhassik, E.; Berezin, M. Y., Design of Fluorescent Nanocapsules as Ratiometric Nanothermometers. *Chem-Eur J* **2014**, *20* (33), 10292-10297.
25. Zhou, D.; Lin, M.; Liu, X.; Li, J.; Chen, Z. L.; Yao, D.; Sun, H. Z.; Zhang, H.; Yang, B., Conducting the Temperature-Dependent Conformational Change of Macrocyclic Compounds to the Lattice Dilation of Quantum Dots for Achieving an Ultrasensitive Nanothermometer. *ACS Nano* **2013**, *7* (3), 2273-2283.
26. Maestro, L. M.; Jacinto, C.; Silva, U. R.; Vetrone, F.; Capobianco, J. A.; Jaque, D.; Sole, J. G., CdTe Quantum Dots as Nanothermometers: Towards Highly Sensitive Thermal Imaging. *Small* **2011**, *7* (13), 1774-1778.
27. Zhou, H.; Sharma, M.; Berezin, O.; Zuckerman, D.; Berezin, M. Y., Nanothermometry: From Microscopy to Thermal Treatments. *Chemphyschem* **2015**.
28. Cadiou, A.; Brites, C. D. S.; Costa, P.; Ferreira, R. A. S.; Rocha, J.; Carlos, L. D., Ratiometric Nanothermometer Based on an Emissive Ln(3+)-Organic Framework. *ACS Nano* **2013**, *7* (8), 7213-7218.
29. Brites, C. D. S.; Lima, P. P.; Silva, N. J. O.; Millán, A.; Amaral, V. S.; Palacio, F.; Carlos, L. s. D., Ratiometric highly sensitive luminescent nanothermometers working in the room temperature range. Applications to heat propagation in nanofluids. *Nanoscale* **2013**, *5* (16), 7572-7580.
30. Ananias, D.; Paz, F. A. A.; Yufit, D. S.; Carlos, L. D.; Rocha, J., Photoluminescent Thermometer Based on a Phase-Transition Lanthanide Silicate with Unusual Structural Disorder. *Journal of the American Chemical Society* **2015**, 150219143728004-8.
31. Wang, Z. P.; Ananias, D.; Carne-Sanchez, A.; Brites, C. D. S.; Imaz, I.; Maspocho, D.; Rocha, J.; Carlos, L. D., Lanthanide-Organic Framework Nanothermometers Prepared by Spray-Drying. *Adv Funct Mater* **2015**, *25* (19), 2824-2830.
32. Brites, C. D. S.; Lima, P. P.; Silva, N. J. O.; Millan, A.; Amaral, V. S.; Palacio, F.; Carlos, L. D., Ratiometric highly sensitive luminescent nanothermometers working in the room temperature range. Applications to heat propagation in nanofluids. *Nanoscale* **2013**, *5* (16), 7572-7580.
33. Jaque, D.; Vetrone, F., Luminescence nanothermometry. *Nanoscale* **2012**, *4* (15), 4301.

34. Wang, X. F.; Zheng, J.; Xuan, Y.; Yan, X. H., Optical temperature sensing of NaYbF₄:Tm³⁺@SiO₂ core-shell micro-particles induced by infrared excitation. *Opt Express* **2013**, *21* (18), 21596-21606.
35. Brites, C. D. S.; Lima, P. P.; Silva, N. J. O.; Millán, A.; Amaral, V. S.; Palacio, F.; Carlos, L. s. D., Thermometry at the nanoscale. *Nanoscale* **2012**, *4* (16), 4799-4829.
36. Ximendes, E. C.; Rocha, U.; Jacinto, C.; Kumar, K. U.; Bravo, D.; Lopez, F. J.; Martin Rodriguez, E.; Garcia-Sole, J.; Jaque, D., Self-monitored photothermal nanoparticles based on core-shell engineering. *Nanoscale* **2016**, *8* (5), 3057-66.
37. Ximendes, E. C.; Santos, W. Q.; Rocha, U.; Kagola, U. K.; Sanz-Rodriguez, F.; Fernandez, N.; Gouveia-Neto, A. D.; Bravo, D.; Domingo, A. M.; del Rosal, B.; Brites, C. D. S.; Carlos, L. D.; Jaque, D.; Jacinto, C., Unveiling in Vivo Subcutaneous Thermal Dynamics by Infrared Luminescent Nanothermometers. *Nano Letters* **2016**, *16* (3), 1695-1703.
38. Zheng, S. H.; Chen, W. B.; Tan, D. Z.; Zhou, J. J.; Guo, Q. B.; Jiang, W.; Xu, C.; Liu, X. F.; Qiu, J. R., Lanthanide-doped NaGdF₄ core-shell nanoparticles for non-contact self-referencing temperature sensors. *Nanoscale* **2014**, *6* (11), 5675-5679.
39. Wawrzynczyk, D.; Bednarkiewicz, A.; Nyk, M.; Streck, W.; Samoc, M., Neodymium(III) doped fluoride nanoparticles as non-contact optical temperature sensors. *Nanoscale* **2012**, *4* (22), 6959-6961.
40. Rocha, U.; Jacinto, C.; Silva, W. F.; Guedes, I.; Benayas, A.; Maestro, L. M.; Elias, M. A.; Bovero, E.; van Veggel, F. C. J. M.; Sole, J. A. G.; Jaque, D., Subtissue Thermal Sensing Based on Neodymium-Doped LaF₃ Nanoparticles. *Acs Nano* **2013**, *7* (2), 1188-1199.
41. Rocha, U.; Upendra Kumar, K.; Jacinto, C.; Ramiro, J.; Caamaño, A. J.; García Sole, J.; Jaque, D., Nd³⁺ doped LaF₃ nanoparticles as self-monitored photo-thermal agents. *Applied Physics Letters* **2014**, *104* (5), 053703.
42. Chen, Y. Y.; Liu, B.; Deng, X. R.; Huang, S. S.; Hou, Z. Y.; Li, C. X.; Lin, J., Multifunctional Nd³⁺-sensitized upconversion nanomaterials for synchronous tumor diagnosis and treatment. *Nanoscale* **2015**, *7* (18), 8574-8583.
43. Sarkar, S.; Chatti, M.; Adusumalli, V. N.; Mahalingam, V., Highly Selective and Sensitive Detection of Cu²⁺ Ions Using Ce(III)/Tb(III)-Doped SrF₂ Nanocrystals as Fluorescent Probe. *ACS Appl Mater Interfaces* **2015**, *7* (46), 25702-8.
44. Wang, G.; Peng, Q.; Li, Y., Upconversion luminescence of monodisperse CaF₂:Yb³⁺/Er³⁺ nanocrystals. *Journal of the American Chemical Society* **2009**, *131* (40), 14200-14201.
45. Li, A. H.; Lu, M.; Yang, J.; Chen, L.; Cui, X.; Sun, Z., Upconversion-luminescent/magnetic dual-functional sub-20 nm core-shell SrF₂:Yb,Tm@CaF₂:Gd heteronanoparticles. *Dalton Trans* **2016**, *45* (13), 5800-7.
46. Du, Y. P.; Sun, X.; Zhang, Y. W.; Yan, Z. G.; Sun, L. D.; Yan, C. H., Uniform Alkaline Earth Fluoride Nanocrystals with Diverse Shapes Grown from Thermolysis of Metal Trifluoroacetates in Hot Surfactant Solutions. *Cryst Growth Des* **2009**, *9* (4), 2013-2019.
47. Pedroni, M.; Piccinelli, F.; Passuello, T.; Polizzi, S.; Ueda, J.; Haro-Gonzalez, P.; Maestro, L. M.; Jaque, D.; Garcia-Sole, J.; Bettinelli, M.; Speghini, A., Water (H₂O and D₂O) Dispersible NIR-to-NIR Upconverting Yb³⁺/Tm³⁺ Doped MF₂ (M = Ca, Sr) Colloids: Influence of the Host Crystal. *Cryst Growth Des* **2013**, *13* (11), 4906-4913.
48. Quintanilla, M.; Cantarelli, I. X.; Pedroni, M.; Speghini, A.; Vetrone, F., Intense ultraviolet upconversion in water dispersible SrF₂:Tm³⁺,Yb³⁺-nanoparticles: the effect of the environment on light emissions. *J. Mater. Chem. C* **2015**, *3* (13), 3108-3113.
49. Villa, I.; Vedda, A.; Cantarelli, I. X.; Pedroni, M.; Piccinelli, F.; Bettinelli, M.; Speghini, A.; Quintanilla, M.; Vetrone, F.; Rocha, U.; Jacinto, C.; Carrasco, E.; Rodríguez, F. S.; Juarranz, Á.; del Rosal, B.; Ortgies, D. H.; Gonzalez, P. H.; Solé, J. G.; García, D. J., 1.3 μm emitting SrF₂:Nd³⁺ nanoparticles for high contrast in vivo imaging in the second biological window. *Nano Research* **2014**, *8* (2), 649-665.

50. Zanzoni, S.; Pedroni, M.; D'Onofrio, M.; Speghini, A.; Assfalg, M., Paramagnetic Nanoparticles Leave Their Mark on Nuclear Spins of Transiently Adsorbed Proteins. *Journal of the American Chemical Society* **2016**, *138* (1), 72-75.
51. Lai, J.; Zhang, Y.; Pasquale, N.; Lee, K. B., An upconversion nanoparticle with orthogonal emissions using dual NIR excitations for controlled two-way photoswitching. *Angewandte Chemie* **2014**, *53* (52), 14419-23.
52. Mondini, S.; Ferretti, A. M.; Puglisi, A.; Ponti, A., Pebbles and PebbleJuggler: software for accurate, unbiased, and fast measurement and analysis of nanoparticle morphology from transmission electron microscopy (TEM) micrographs. *Nanoscale* **2012**, *4* (17), 5356-72.
53. Dong, N. N.; Pedroni, M.; Piccinelli, F.; Conti, G.; Sbarbati, A.; Ramirez-Hernandez, J. E.; Maestro, L. M.; Iglesias-de la Cruz, M. C.; Sanz-Rodriguez, F.; Juarranz, A.; Chen, F.; Vetrone, F.; Capobianco, J. A.; Sole, J. G.; Bettinelli, M.; Jaque, D.; Speghini, A., NIR-to-NIR two-photon excited CaF₂:Tm³⁺, Yb³⁺ nanoparticles: multifunctional nanoprobe for highly penetrating fluorescence bio-imaging. *ACS nano* **2011**, *5* (11), 8665-71.
54. Quintanilla, M.; Nunez, N. O.; Cantelar, E.; Ocana, M.; Cusso, F., Tuning from blue to magenta the up-converted emissions of YF₃:Tm³⁺/Yb³⁺ nanocrystals. *Nanoscale* **2011**, *3* (3), 1046-52.
55. Zheng, K.; Wang, L.; Zhang, D.; Zhao, D.; Qin, W., Power switched multiphoton upconversion emissions of Er³⁺ in Yb³⁺/Er³⁺ codoped beta-NaYF₄ microcrystals induced by 980 nm excitation. *Optics express* **2010**, *18* (3), 2934-9.
56. Sun, J.; Xian, J.; Zhang, X.; Du, H., Hydrothermal synthesis of SrF₂:Yb³⁺/Er³⁺ micro-/nanocrystals with multiform morphologies and upconversion properties. *Journal of Rare Earths* **2011**, *29* (1), 32-38.
57. Jalani, G.; Naccache, R.; Rosenzweig, D. H.; Haglund, L.; Vetrone, F.; Cerruti, M., Photocleavable Hydrogel-Coated Upconverting Nanoparticles: A Multifunctional Theranostic Platform for NIR Imaging and On-Demand Macromolecular Delivery. *Journal of the American Chemical Society* **2016**, *138* (3), 1078-83.
58. Zhong, Y.; Tian, G.; Gu, Z.; Yang, Y.; Gu, L.; Zhao, Y.; Ma, Y.; Yao, J., Elimination of photon quenching by a transition layer to fabricate a quenching-shield sandwich structure for 800 nm excited upconversion luminescence of Nd³⁺-sensitized nanoparticles. *Advanced materials* **2014**, *26* (18), 2831-7.
59. Wang, F.; Han, Y.; Lim, C. S.; Lu, Y.; Wang, J.; Xu, J.; Chen, H.; Zhang, C.; Hong, M.; Liu, X., Simultaneous phase and size control of upconversion nanocrystals through lanthanide doping. *Nature* **2010**, *463* (7284), 1061-5.
60. Jagosich, F. H.; Gomes, L.; Tarelho, L. V. G.; Courrol, L. C.; Ranieri, I. M., Deactivation effects of the lowest excited states of Er³⁺ and Ho³⁺ introduced by Nd³⁺ ions in LiYF₄ crystals. *J Appl Phys* **2002**, *91* (2), 624-632.
61. Tian, L.; Xu, Z.; Zhao, S.; Cui, Y.; Liang, Z.; Zhang, J.; Xu, X., The Upconversion Luminescence of Er³⁺/Yb³⁺/Nd³⁺ Triply-Doped β-NaYF₄ Nanocrystals under 808-nm Excitation. *Materials* **2014**, *7* (11), 7289-7303.
62. Huang, F.; Zhang, Y.; Hu, L.; Chen, D., Judd–Ofelt analysis and energy transfer processes of Er³⁺ and Nd³⁺ doped fluoroaluminate glasses with low phosphate content. *Optical Materials* **2014**, *38*, 167-173.
63. Shen, X.; Nie, Q.; Xu, T.; Dai, S.; Wang, X., Investigation on energy transfer from Er³⁺ to Nd³⁺ in tellurite glass. *Journal of Rare Earths* **2008**, *26* (6), 899-903.
64. Zheng, Y.; Chen, B.; Zhong, H.; Sun, J.; Cheng, L.; Li, X.; Zhang, J.; Tian, Y.; Lu, W.; Wan, J.; Yu, T.; Huang, L.; Yu, H.; Lin, H., Optical Transition, Excitation State Absorption, and Energy Transfer Study of Er³⁺, Nd³⁺ Single-Doped, and Er³⁺/Nd³⁺ Codoped Tellurite Glasses for Mid-Infrared Laser Applications. *Journal of the American Ceramic Society* **2011**, *94* (6), 1766-1772.

65. Peng, S.; Zhou, Y.; Yang, F.; Wu, L.; Qi, Y.; Wang, B., Improved thermal stability and intense blue upconversion in Yb³⁺/Nd³⁺/Tm³⁺ tri-doped tellurite glasses. *Materials Letters* **2015**, *138*, 132-134.
66. Gouveia-Neto, A. d. S.; Vermelho, M. V. D.; Jacinto, C., Vis–NIR luminescence emission via energy-transfer in Tm³⁺/Er³⁺ and Tm³⁺/Nd³⁺ codoped glass under 1.319 μm excitation. *Journal of Luminescence* **2016**, *172*, 275-278.
67. Chung, W. J. H., J., Energy Transfer Process for the Blue Up-Conversion in Calcium Aluminate Glasses Doped with Tm³⁺ and Nd³⁺. *J. Am. Ceram. Soc.* **2001**, *84*, 348-352.
68. Shang, Y.; Hao, S.; Liu, J.; Tan, M.; Wang, N.; Yang, C.; Chen, G., Synthesis of Upconversion β-NaYF₄:Nd³⁺/Yb³⁺/Er³⁺ Particles with Enhanced Luminescent Intensity through Control of Morphology and Phase. *Nanomaterials* **2015**, *5* (1), 218-232.
69. Capobianco, J. A.; Vetrone, F.; D'Alesio, T.; Tessari, G.; Speghini, A.; Bettinelli, M., Optical spectroscopy of nanocrystalline cubic Y₂O₃:Er³⁺ obtained by combustion synthesis. *Physical Chemistry Chemical Physics* **2000**, *2* (14), 3203-3207.
70. Mahalingam, V.; Vetrone, F.; Naccache, R.; Speghini, A.; Capobianco, J. A., Colloidal Tm³⁺/Yb³⁺-Doped LiYF₄ Nanocrystals: Multiple Luminescence Spanning the UV to NIR Regions via Low-Energy Excitation. *Adv Mater* **2009**, *21* (40), 4025--.
71. Chung, W. J.; Heo, J., Energy Transfer Process for the Blue Up-Conversion in Calcium Aluminate Glasses Doped with Tm³⁺ and Nd³⁺. *Journal of the American Ceramic Society* **2004**, *84* (2), 348-52.
72. Ximendes, E. C.; Rocha, U.; Kumar, K. U.; Jacinto, C.; Jaque, D., LaF₃ core/shell nanoparticles for subcutaneous heating and thermal sensing in the second biological-window. *Applied Physics Letters* **2016**, *108* (25), 253103.
73. Carnall, W. T., Electronic Energy Levels in the Trivalent Lanthanide Aquo Ions. I. Pr³⁺, Nd³⁺, Pm³⁺, Sm³⁺, Dy³⁺, Ho³⁺, Er³⁺, and Tm³⁺. *The Journal of Chemical Physics* **1968**, *49* (10), 4424.
74. Renero-Lecuna, C.; Martín-Rodríguez, R.; Valiente, R.; González, J.; Rodríguez, F.; Krämer, K. W.; Güdel, H. U., Origin of the High Upconversion Green Luminescence Efficiency in β-NaYF₄: 2% Er³⁺, 20% Yb³⁺. *Chemistry of Materials* **2011**, *23* (15), 3442-3448.
75. Marciniak, L.; Bednarkiewicz, A.; Stefanski, M.; Tomala, R.; Hreniak, D.; Strek, W., Near infrared absorbing near infrared emitting highly-sensitive luminescent nanothermometer based on Nd³⁺ to Yb³⁺ energy transfer. *Phys Chem Chem Phys* **2015**, *17* (37), 24315-21.
76. Miyakawa, T.; Dexter, D. L., Phonon Sidebands, Multiphonon Relaxation of Excited States, and Phonon-Assisted Energy Transfer between Ions in Solids. *Physical Review B* **1970**, *1* (7), 2961-2969.
77. Jaque, D.; Ramirez, M.; Bausá, L.; Solé, J.; Cavalli, E.; Speghini, A.; Bettinelli, M., Nd³⁺→Yb³⁺ energy transfer in the YAl₃(BO₃)₄ nonlinear laser crystal. *Physical review. B, Condensed matter* **2003**, *68* (3), 035118.
78. Caldino, U.; Jaque, D.; Martín Rodríguez, E.; Ramírez, M.; Garcia Sole, J.; Speghini, A.; Bettinelli, M., Nd³⁺→Yb³⁺ resonant energy transfer in the ferroelectric Sr_{0.6}Ba_{0.4}Nb₂O₆ laser crystal. *Physical Review B* **2008**, *77* (7), 075121.
79. Falin, M.; Gerasimov, K.; Latypov, V.; Leushin, A.; Bill, H.; Lovy, D., EPR and optical spectroscopy of Yb³⁺ ions in CaF₂ and SrF₂. In *Journal of Luminescence*, **2003**; Vol. 102, pp 239-242.
80. Carrasco, E.; del Rosal, B.; Sanz-Rodríguez, F.; de la Fuente, Á. J.; Gonzalez, P. H.; Rocha, U.; Kumar, K. U.; Jacinto, C.; Solé, J. G.; Jaque, D., Intratumoral Thermal Reading During Photo-Thermal Therapy by Multifunctional Fluorescent Nanoparticles. *Advanced Functional Materials* **2015**, *25* (4), 615-626.
81. Ceron, E. N.; Ortgies, D. H.; del Rosal, B.; Ren, F.; Benayas, A.; Vetrone, F.; Ma, D.; Sanz-Rodríguez, F.; Sole, J. G.; Jaque, D.; Rodriguez, E. M., Hybrid Nanostructures

- for High-Sensitivity Luminescence Nanothermometry in the Second Biological Window. *Adv Mater* **2015**, *27* (32), 4781-4787.
82. Balabhadra, S.; Debasu, M. L.; Brites, C. D.; Nunes, L. A.; Malta, O. L.; Rocha, J.; Bettinelli, M.; Carlos, L. D., Boosting the sensitivity of Nd³⁺-based luminescent nanothermometers. *Nanoscale* **2015**, *7* (41), 17261-7.
 83. Balabhadra, S.; Debasu, M. L.; Brites, C. D.; Nunes, L. A.; Malta, O. L.; Rocha, J.; Bettinelli, M.; Carlos, L. D., Boosting the sensitivity of Nd³⁺-based luminescent nanothermometers. *Nanoscale* **2015**.
 84. Benayas, A.; del Rosal, B.; Pérez-Delgado, A.; Santacruz-Gómez, K.; Jaque, D.; Hirata, G. A.; Vetrone, F., Nd:YAG Near-Infrared Luminescent Nanothermometers. *Advanced Optical Materials* **2015**, *3* (5), 687-694.
 85. Marciniak, L.; Prorok, K.; Frances-Soriano, L.; Perez-Prieto, J.; Bednarkiewicz, A., A broadening temperature sensitivity range with a core-shell YbEr@YbNd double ratiometric optical nanothermometer. *Nanoscale* **2016**, *8* (9), 5037-42.
 86. Marciniak, L.; Bednarkiewicz, A.; Kowalska, D.; Streck, W., A new generation of highly sensitive luminescent thermometers operating in the optical window of biological tissues. *J. Mater. Chem. C* **2016**, *4* (24), 5559-5563.

Conclusion

CaF₂ and SrF₂ proved to be good host for lanthanide ions, showing interesting luminescent properties and a good versatility for architecting structures with different functionalities.

In Chapter 1 an analysis of the site symmetry for lanthanide ions in CaF₂ and SrF₂ NPs was carried out, using Eu³⁺ ions as symmetry probe. Thanks to Eu³⁺ ions properties it was possible to identify a site with D₂ symmetry, previously unknown in CaF₂ and SrF₂. We show that Na⁺ ions can substitute Ca²⁺ ions more efficiently than K⁺ ions, helping the formation of symmetric sites for lanthanide ions. Furthermore, the extremely long luminescence decay time shown by Eu³⁺ ions in CaF₂ NPs co-doped with Na⁺ ions could be used for Fluorescence Lifetime Imaging Microscopy.

In Chapter 2 we showed that CaF₂ NPs doped with Nd³⁺ ions can be used as luminescent nanothermometers in the first and second biological windows. Nd³⁺ luminescence can be excited at 800 nm, a wavelength that possesses a high penetration in the biological tissues (around 2 cm) since it lies in the middle of the first biological window where the biological tissues present a minimum of the absorption. Furthermore, the low absorption can reduce the tissue damage due to irradiation. The nanothermometry measurements were carried out by exciting Nd³⁺ luminescence at 573 nm. The nanothermometric properties were evaluated taking into account the two Nd³⁺ emissions at 867 nm and 1058 nm, respectively in the first and second biological transparency windows. The Nd³⁺ doped CaF₂ NPs show interesting nanothermometric properties, presenting a sensitivity that is coherent with the sensitivities obtained for other Nd³⁺-based nanothermometers, with a minimum measurable temperature variation useful for temperature monitoring during a photothermal therapy.

In Chapter 3 we showed the design and synthesis of core@multishell NPs, with the aim of producing a multimodal tool for optical imaging in the VIS and NIR range and for nanothermometry. The NPs structure was designed to obtain different upconversion emission upon different excitation wavelengths (by harvesting 800 nm with Nd³⁺ ions or 980 nm with Yb³⁺ ions). We showed that by inverting the doping ions of the core and the second shell the upconversion properties can be inverted, and that Er³⁺ and Tm³⁺ emission can be quenched by the presence of Nd³⁺ as co-doping ion. The NPs showed an intense NIR luminescence when excited at 800 nm, due to Nd³⁺ ions emission around 870 nm and 1060 nm and to Yb³⁺ ions emission at 980 nm. While in Chapter 2 we showed nanothermometry based only on Nd³⁺ NIR luminescence, in Chapter 3 we used a different strategy, by exerting Yb³⁺ emission at 980 nm and Nd³⁺ emission at 1060 nm. The resulting luminescent nanothermometers presented high relative sensitivity values. By comparing the thermometric properties of the three different NPs we were able to prove that the thermometric performance of the nanothermometers can be improved by choosing the doping ions that co-dope the second shell with Nd³⁺ and Yb³⁺. In particular we showed that the NPs with only Yb³⁺ and Nd³⁺ co-doping the second shell present a relative sensitivity similar to already reported thermal sensitivities. When Tm³⁺ ions are added to the second shell the relative sensitivity of the nanothermometer increases and if Er³⁺ ions are used as third dopant, the

relative sensitivity is higher than for the other NPs, higher than most NIR nanothermometers ever reported. Future measurements will be carried out to try to use the NPs for self-monitored photothermal therapy (thanks to the high Nd^{3+} content of the external shell). Since the thermometric performance of the Yb^{3+} - Nd^{3+} based nanothermometer strongly changes by changing the dopant ions in the second shell further investigation will be carried out varying the dopant ions and their relative amounts to improve the sensitivity of the nanothermometer.

APPENDIX A

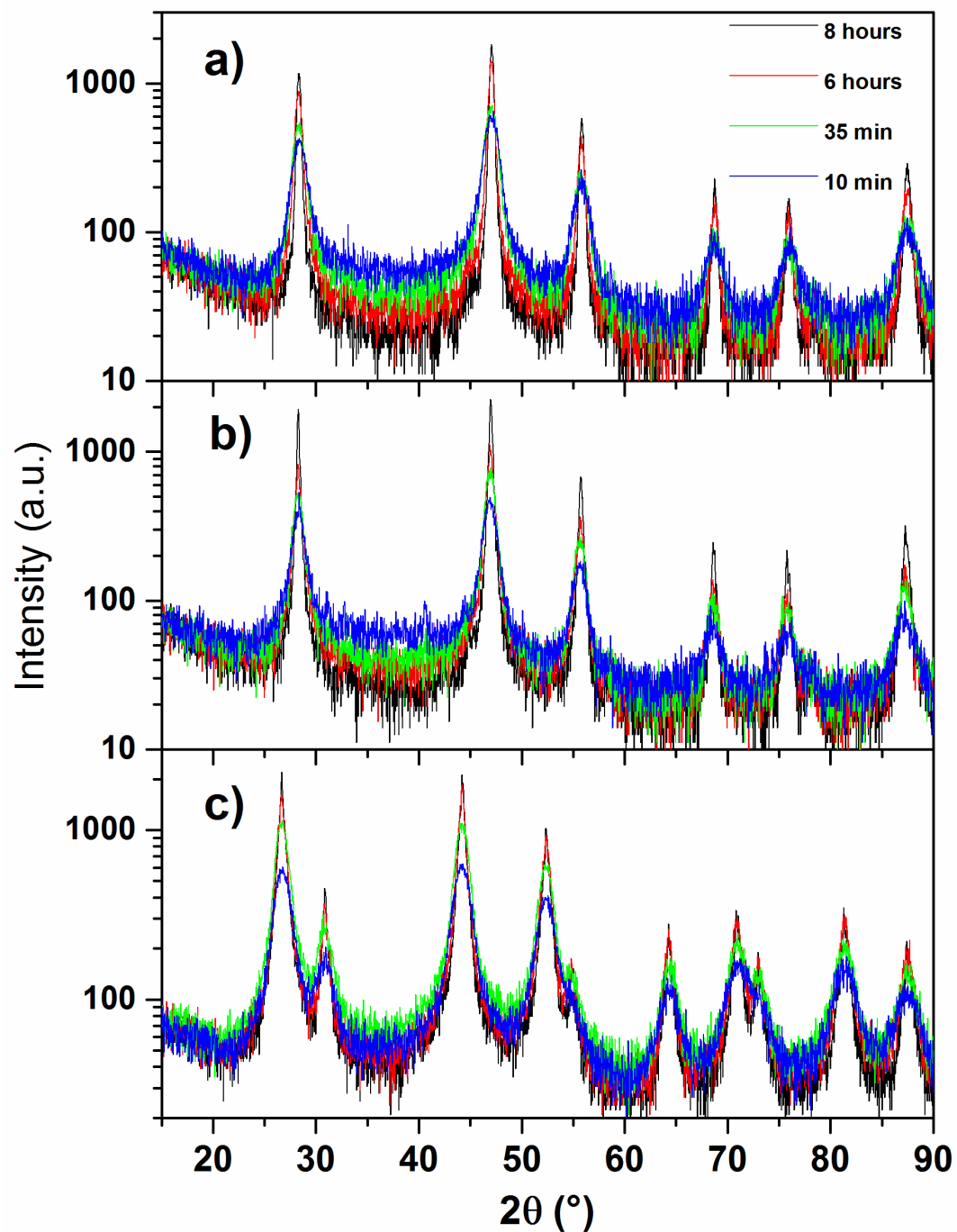


Figure A1. XRD patterns for the samples synthesized at different reaction times. In a) the CN samples, in b) the CK samples, in c) the SN samples.

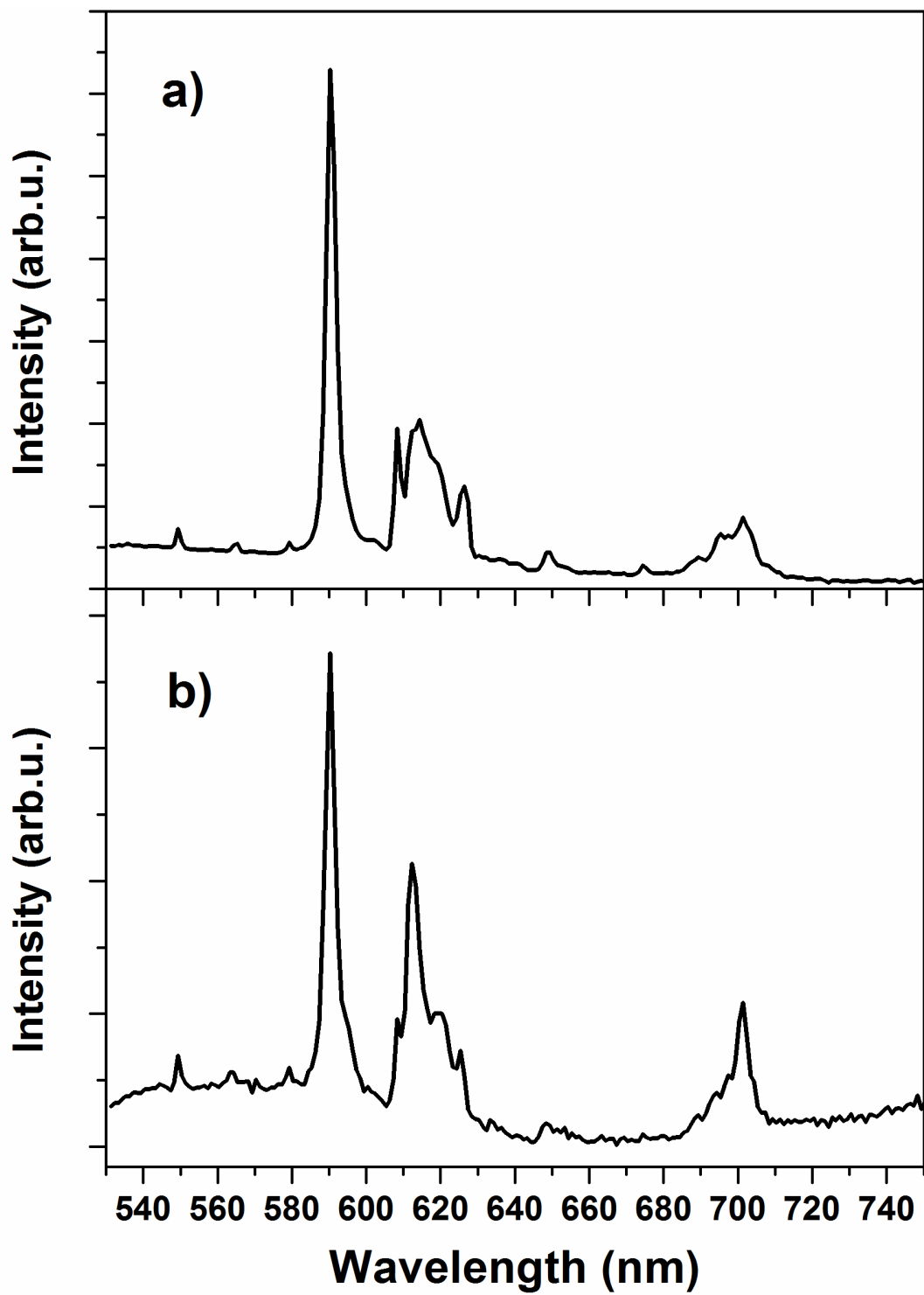


Figure A2. CN10 (a) and SN10 (b) emission under 465 nm excitation.

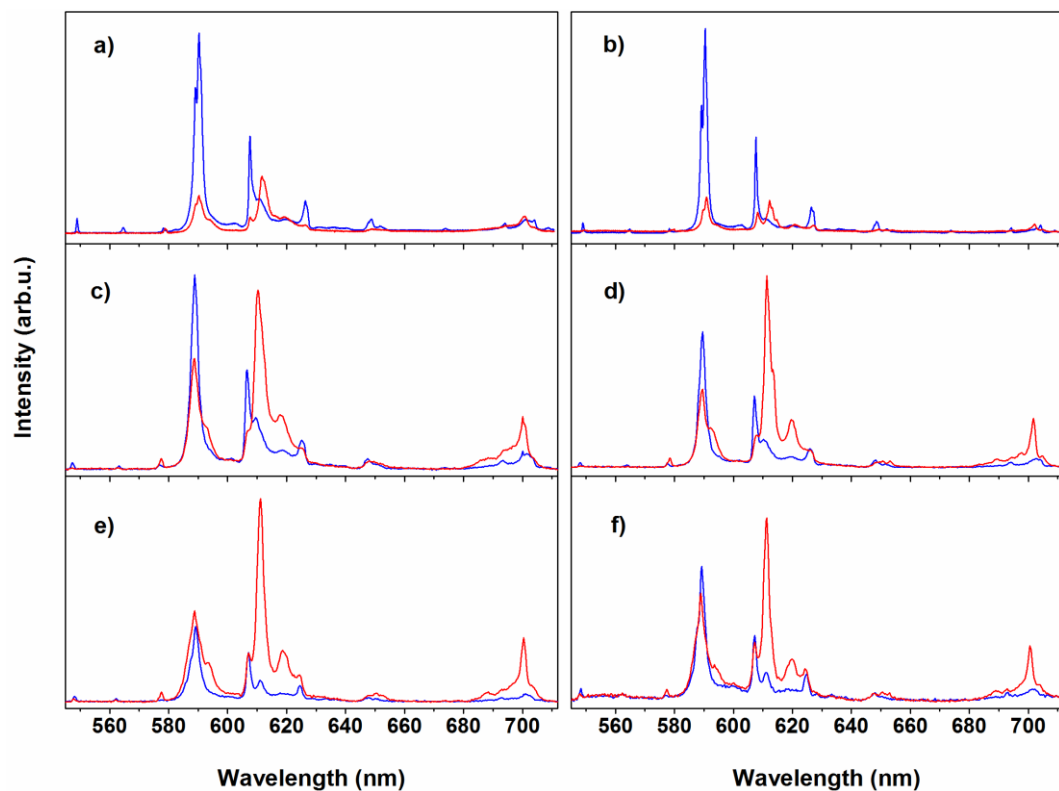


Figure A3. Site selection spectroscopy for CN35 (a), CN360 (b), CK35 (c), CK360 (d), SN35 (e), SN360 (f) nanoparticles. Site 1 is the blue line, site 2 is the red line.

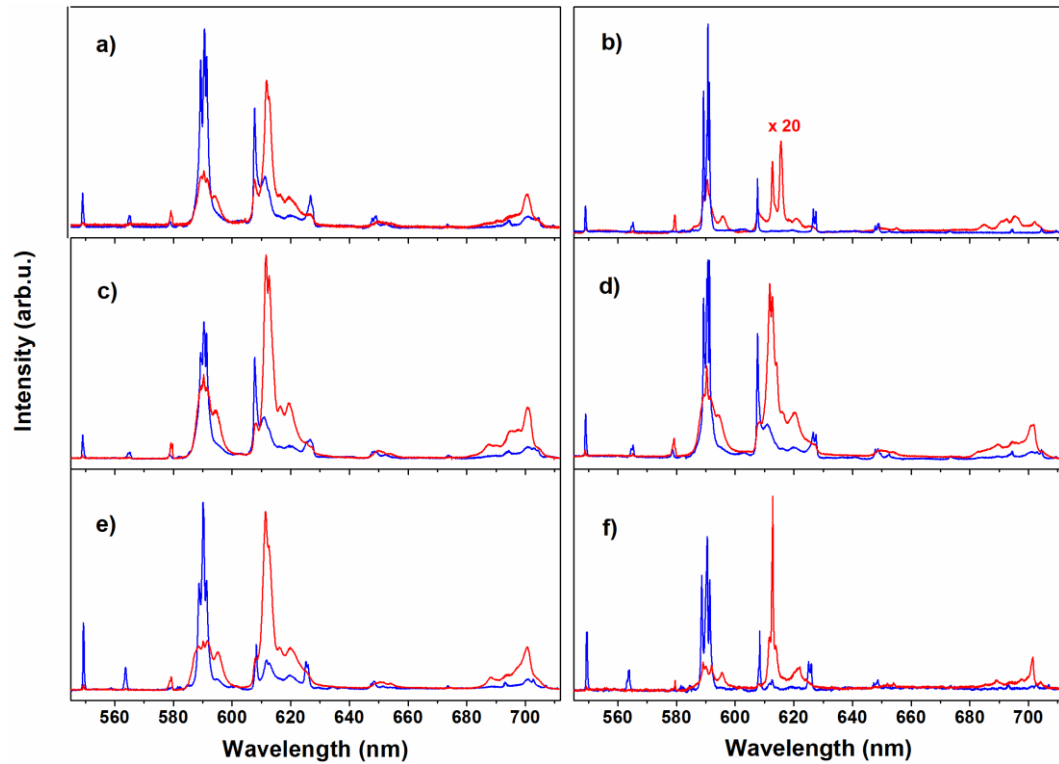


Figure A4. Site selection spectroscopy at 77 K for CN10 (a), CN480 (b), CK10 (c), CK480 (d), SN10 (e), SN480 (f) nanoparticles. Site 1 is the blue line, site 2 is the red line.